공학박사학위논문

형태학적 제어를 통한 진동 입자 군집의 가변적 거동

Reconfigurable behaviors of vibrated particle collectives through morphological control

2023 년 8 월

서울대학교 대학원

기계공학부

손 경 민

형태학적 제어를 통한 진동 입자 군집의 가변적 거동

Reconfigurable behaviors of vibrated particle collectives through morphological control

지도교수 김 호 영

이 논문을 공학박사 학위논문으로 제출함

2023 년 4 월

서울대학교 대학원

기계공학부

손 경 민

손경민의 공학박사 학위논문을 인준함

2023 년 6 월

위 원 장 : 김 도 년 (인)

부위원장 : 김 호 영 (인)

위 원 : 신 용 대 (인)

위 원 : 김 아 영 (인)

위 원 : 이 정 수 (인)

위 원 : 정 소 현 (인)

Abstract

Reconfigurable behaviors of vibrated particle collectives
through morphological control

Kyungmin Son
Department of Mechanical Engineering
The Graduate School
Seoul National University

Due to the demand for robotic machines capable of performing multiple functions in various environments while using limited resources, there is a growing interest in novel mechanical systems with high adaptability, and functionality. In addition, the potential use of small-scale reconfigurable systems in various fields increases the need for scalable, material-independent design strategies. Inspired by collectives in nature that alter their morphology to accomplish diverse tasks, many researcher have developed unconventional, programmable systems employing particle or robot swarms. In this work, motivated by recently developed artificial cluster systems, we explore the dynamics of vibrated particles and collective structures composed of them. Without elaborate external control, we try to regulate the behaviors and functions of collective structures by modulating the direct or indirect mechanical interactions between their components through morphological control.

First, we explore the redistribution of solid-like granular media to construct collective systems that meet both the structural rigidity and flexibility required for achieving multi-functionality and high reliability. We introduce a system consisting of a limited quantity of self-propelled particles (SPPs) that are dispersed among densely packed particles subjected to vertical vibration within a two-dimensional circular confinement. We show that an SPP exhibits superdiffusion in a dense granular medium, where the diffusion exponent increases with polarity and aspect ratio. The SPPs form a cluster upon reaching the boundary, and the increased number of SPPs facilitates the transition from a moving to a static state. We also present a qualitative and quantitative analysis of particle behavior in the bulk and at the boundary. These results suggest a simple and effective method for controlling self-organization by adjusting the shape and number of components.

Second, based on the dynamics of SPPs in a dense environment, we create a particle structure composed of a mobile boundary containing densely packed particles with a few SPPs, as opposed to the previously proposed particle structures with a low number density. Densely packed systems exhibit structural robustness, rendering them advantageous for operation in high-stress environments. The manipulation of the shape and number of SPPs results in a wide range of structure behaviors including random, rotational, and directional motion. We show that the dynamic properties of these structures, such as the magnitudes of polarity and chirality, are also affected by the particle number density and the mechanical properties of the confining boundary. Our findings have the potential to facilitate substantial regulation of dense structure's behavior through small alteration of components.

Thirdly, away from the concept of confining particles, we demonstrate that a particle cluster can organize more adaptable and multifunctional structures that are capable of modifying their shape and motion in order to accomplish a variety of desired functions. We create an open chain structure made up of SPPs and connecting links, the design parameters of which allow us to control the relative motion of adjacent particles. The modification of flexible structures improves the chain's functionality, evidenced by its ability to perform a variety of tasks that may be nutually exclusive, such as passing or enclosing objects, transporting objects forward or backward, traversing or remaining obstacles, and penetrating or blocking narrow spaces. Through geometric analysis, we present the mechanisms of different chain behavior and the analytical predictions of their dynamic properties. Our method can be used to create robust and low-cost robotic machines capable of object transport, environmental monitoring, and traffic management.

The successful control of collective behavior in numerous ways demonstrates the reconfigurable and versatile nature of our scalable approach which simply regulates mechanical interactions between components through shape control. We believe that our study will aid in the development of reconfigurable soft robot systems with minimal ingredients at multiple scales.

Keywords: Active matter, Vibrated particles, Collective behavior, Reconfigurable functions, Morphological control
Student Number: 2018-31738

Contents

List of Figures

Chapter 1

Introduction

1.1 Overview

This thesis demonstrates reconfigurable and scale-free nature of novel collective systems using vibrated particles, and their potential for a range of behaviors and functions. We alter the geometry of a particle or link to modify the direct or indirect mechanical interactions between adjacent particles, which in turn controls the particle's motion and consequently the collective structure's behavior. We first discuss the research contexts and motivations in §1.2. In this section, we introduce several collectives in nature and briefly review particle and robotic swarms that have previously been developed to mimic the complex behavior and function of natural collectives. In chapter 2, we present a system in which a small number of self-propelled particles (SPPs) move inside a dense population of randomly vibrated particles within a circular confinement. We experimentally and analytically show that the direct mechanical interaction between particles in dense granular media cause the diffusion exponent of SPP to vary with polarity and shape. We then demonstrate that the number of SPPs determines whether the SPP cluster at the boundary is in a moving or static state. In chapter 3, based on the findings of chapter 2, we present rigid particle structures made up of densely packed particles and mobile boundaries. By adjusting the shape and number of SPPs, we demonstrate that the structure displays a variety of behaviors ranging from random, rotational, to directional motion. We show that the dynamic properties of the structures can also be modulated by the particle number density and the mechanical properties of the boundary. In chapter 4, we present nonloop chains composed of SPPs and links connecting two adjacent particles. We demonstrate that flexible structure and appropriate interparticle interactions mediated by the connecting links enables the chain to adapt to its environments by altering its shape and the orientation of each particle. We provide evidence for the chain's superior functionality by performing multiple tasks that may be opposed to each other by morphological control. Finally, in chapter 5, we summarize our research and suggest a few future research subjects.

1.2 Backgrounds and motivations

Multi-functionality has become increasingly sought after in recent years due to its potential to enhance tool efficiency and convenience, while simultaneously mitigating environmental pollution by minimizing energy and material usage. Robotic machines that perform multiple functions with minimal resources are particularly required in constrained conditions, such as resource scarcity or harsh, complex environments resulting from disasters. To achieve such functionality, it is necessary to develop soft robotic machines that can be freely reconfigured. Because shape often determines function, technologies that enable flexible reconfiguration of systems as well as high structural stability will revolutionize the current landscape of robotic machines. These include the development of high-degree-of-freedom mechanical systems with variable functionality, and the promotion of novel manufacturing methods.

Scalability is another important concern for the new mechanical system. The demand for the technologies that change form and function is not limited to macroscale systems, which include the conventional robotic

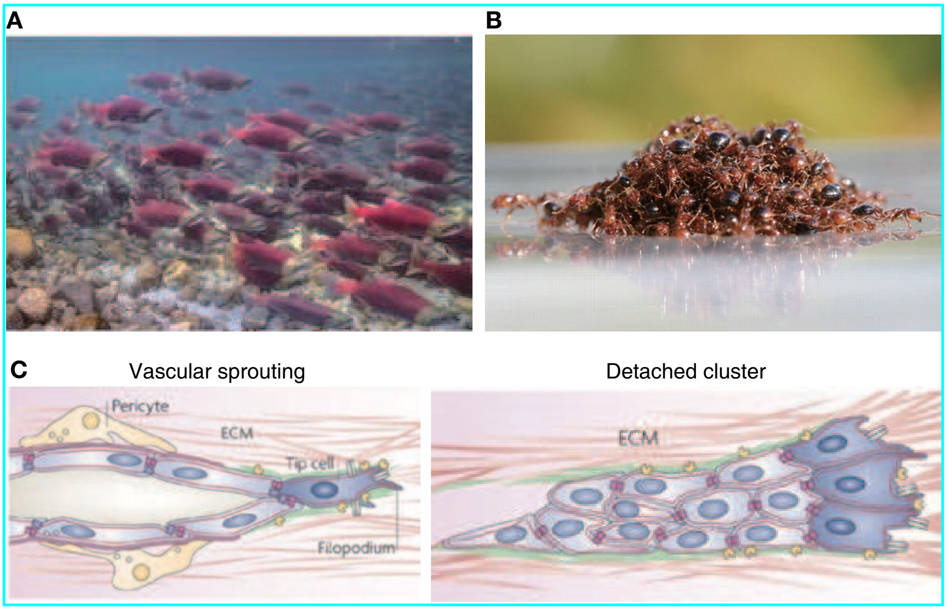

Figure 1.1: Various collective behaviors in nature. **A**, Salmon swim in schools. **B**, Fire ants form a raft, with a partly wet layer on the bottom and dry ants on top. **C**, Endothelial cells and cancer cells show vascular sprouting and collective invasion, respectively. **A**, **B**, and **C** are adapted from (Westley *et al.*, 2018), (Mlot *et al.*, 2011), and (Friedl & Gilmour, 2009), respectively.

machines used in many industries. The potential utilization of reconfigurable robotic machines at micro or submicron scales is anticipated in various fields such as healthcare (Nelson *et al.*, 2010), manufacturing (Zheng *et al.*, 2004), programmable matter (Goldstein *et al.*, 2005), and biochemical applications (Guix *et al.*, 2014). However, adopting electromechanical actuation components, which are typically utilized in conventional robotics, is difficult at small scales due to manufacturing constraints, the existence of stochastic forces, or the necessity for biocompatibility. Therefore, achieving scalability requires a material-agnostic design strategy.

To develop highly adaptable and functional systems that possess programmable, scale-free, and material-independent characteristics, there has been a recent surge in attention towards using clusters of small units as a viable method. Examples of clusters consisting of several individual units are observed in nature. Collectives in nature frequently use reconfiguration, which involves changing the morphology of the group to carry out complex tasks in diverse environments (McCann *et al.*, 2010; Rappel *et al.*, 1999; Vicsek & Zafeiris, 2012). For large scale organisms, vast fish schools, bird flocks, and ungulate herds with large numbers of individuals move in a highly coordinated manner to reduce flow resistance, avoid predators, or find food (Fig. 1.1A) (Westley *et al.*, 2018). The cooperative behavior is also observed in smaller scale, where fire ant shows remarkable behaviors including construction of chains, walls, and rafts made entirely of individual ants linked together to keep its colonies together under harsh circumstances (Fig. 1.1B) (Mlot *et al.*, 2011). Even microorganisms can adapt to changes in their environments and perform various tasks by reconfiguration (Fig. 1.1C) (Friedl & Gilmour, 2009). The versatility and resilience exhibited by collectives in nature across various scales serves as a source of motivation for engineers to implement complex behavior through particle or robot collectives that are robustly reconfigurable.

In the last decade, there has been a lot of research on using clusters of self-propelled units to mimic the complex behaviors and functions of natural collectives. Kilobots, which are fist-sized motors equipped with autonomous control logic and onboard memory, is an example of the macroscale robotic swarms (Fig. 1.2A) (Rubenstein *et al.*, 2014). The collectives are governed by an algorithm operating on each kilobot, thereby facilitating their self-organization into predetermined formations as a swarm (Divband Soorati *et al.*, 2019; Slavkov *et al.*, 2018). At the microscale, collectives in artificial systems interact via physical and chemical interactions to orchestrate global responses that surpass the capabilities of individual entities (Martínez-Pedrero *et al.*, 2021; Yigit *et al.*, 2019). Self-driven systems with active particles and externally driven systems with particles controlled by external stimuli are the primary routes for reconfiguration at this scale (Sitti, 2017). For example, collectives of microrobots propelled by external

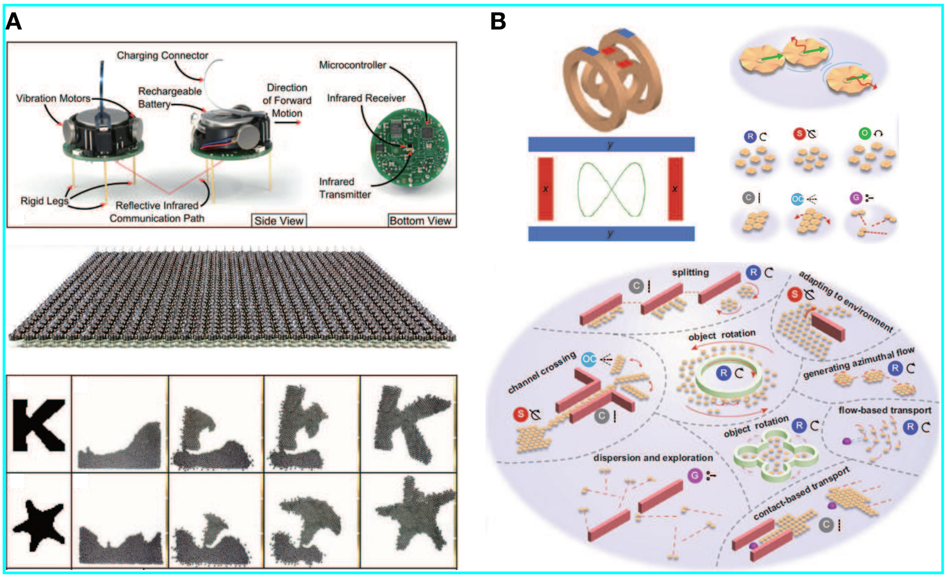

Figure 1.2: Different behaviors of collectives of artificial systems. **A**, Kilobot swarm robot can construct any shape with simple connections. **B**, Microrobot collectives driven by external magnetic fields performs various behaviors and functions. **A**, and **B** are adapted from (Rubenstein *et al.*, 2014) and (Gardi *et al.*, 2022), respectively.

magnetic fields can modify the way one or more particles in the system move (Wang *et al.*, 2017), resulting in a variety of behaviors (Fig. 1.2B) (Gardi *et al.*, 2022). Although these systems have been introduced as capable of performing complex functions, such systems are restricted to employing intelligent units with memory and the ability to interact with neighboring units (Li *et al.*, 2019), or to managing particle swarms through sophisticated external force field control (Xie *et al.*, 2019; Yan *et al.*, 2016). First, the knowledge and high-level functions would be challenging to embed in microparticles, which makes it difficult to apply behavioral mechanisms of Kilobots at multiple scales. In the case of externally driven systems, the particles are limited to stimulus-responsive materials (Vutukuri *et al.*, 2020), and can only be controlled in environments where external stimuli above a certain intensity can reach them. Therefore, we seek a method for

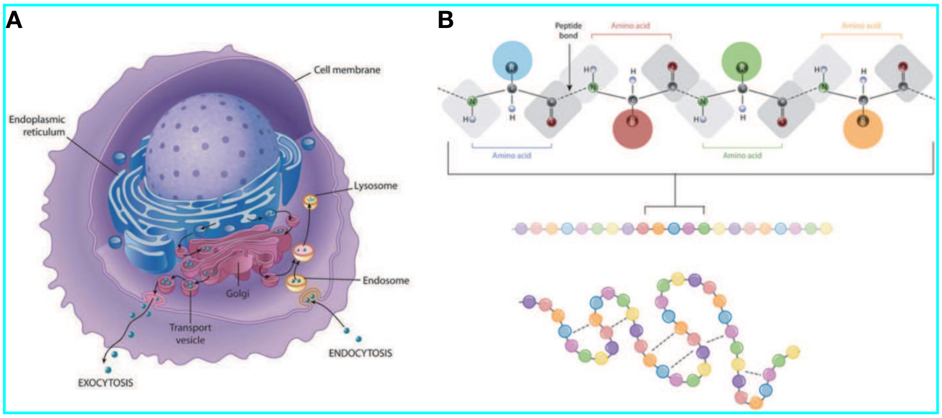

Figure 1.3: Structure of cells and proteins. **A**, Cells are made up of numerous organelles that are separated by flexible phospholipid membranes. **B**, Proteins are composed of amino acids connected by a series of peptide bonds. **A**, and **B** are adapted from (O'Connor & Adams, 2010).

creating self-driven systems with active but nonintelligent particles.

In situations where there are no binding forces between particles and no external stimuli to bring them together, each freely moving particle is susceptible to be dispersed by flow and disturbances. To prevent particles from scattering, we can either confine them within a boundary or connect them with links. Such constraints are easily found in biology. Cells are composed of many organelles surrounded by flexible phospholipid membranes, and biomolecules such as proteins are made up of chains of subunits (Fig. 1.3) (O'Connor & Adams, 2010). The composition of cell and vesicles, and the possibility of connecting colloidal particles using polymers (DeVries *et al.*, 2007) or DNA oligonucleotides (Nykypanchuk *et al.*, 2008; Zhang *et al.*, 2013) suggest that these approaches are applicable to a range of scales. Recent work has shown that simple active robots can be confined to flexible, mobile boundaries (Deblais *et al.*, 2018), or that active particles can be connected to form chains or loops (Spellings *et al.*, 2015) to perform multiple functions.

However, previous studies on these structures are still limited to certain conditions. Most of the enclosed particle ensembles are composed of low number density which allows particle to be skewed to one side or mechanically interact with neighboring particles (Boudet *et al.*, 2021; Savoie *et al.*, 2019). Although structures with high number density have high structural stability so that they can operate in high-stress environments without losing their shape and functions, they have so far only shown the potential for rotational motion (Liu *et al.*, 2020) because changing the position and orientation of the particles is difficult in a densely packed environment. In the case of chain structures, they show only limited dynamics, relying mostly on controlling the sequence of the two types of particles (Agrawal & Glotzer, 2020; Scholz *et al.*, 2021). How dense particle structure and particle chain structure can perform diverse behaviors and functions is not well understood.

In this thesis, we explore the possibility of implementing various behaviors and functions in (1) dense particle structures and (2) particle chain structures. To make self-driven systems with nonintelligent particles, we design and fabricate particles that propel themselves by vertical vibration. Each particle is restricted in its motion by the boundaries that confine it, or by the links that physically connect multiple particles. We first observe the dynamics of self-propelled particles (SPPs) which is surrounded by densely packed, randomly vibrated particles, and found that the motion of the SPPs in a dense environment depends on their translational and rotational properties, shape and number. The change of particle motion leads to diverse behaviors of dense particle structures, ranging from random, rotational to directional motion. We then demonstrate the high adaptability and functionality of particle chain structure, where SPPs are connected by links. Our strategy is morphological control (Agrawal & Glotzer, 2020), in which the chains behavior is controlled by the mechanical interactions between the particles. The highly flexible and symmetrical structure of our chains, along with the restricted motion of each particle, allows them to perform diverse tasks that would not be possible without intelligent particles and sophisticated external field control. The change of functions through adjustment of the dynamic properties, shape, and range of motion of the simple, active units makes these particle structures both reconfigurable and compatible with the scale-free physics. Our approach for achieving multiple functions with minimal information and resources will ultimately contribute to the development of intelligent artificial structures that can adapt to various environments, including the inside of living organisms, and to a sustainable society through material savings.

Chapter 2

Dynamics of polar particles in a vibrated dense granular system

Constructing a system that can self-organize into diverse functional structures presents an engineering challenge: structural rigidity is necessary for reliable performance of a function, while structural fluidity is required for switching between different functions. As a solution to this problem, we present a system in which a small number of self-propelled particles (SPPs) are interspersed with granular particles that are vibrated vertically in a two-dimensional circular confinement. Two key conclusions are drawn from our experiments. First, an SPP shows superdiffusion within a dense granular media, the diffusion exponent of which increases as the aspect ratio increases. Second, after the SPPs reach the boundary form a moving cluster, a transition from a moving state to a static state tends to occur as the number of SPPs increases. These findings indicate a straightforward and efficient way for manipulating self-organization by regulating the shape and amount of SPPs.

2.1 Introduction

Many natural systems exhibit the phenomena of self-organization, in which individual components interact locally to generate large-scale structures autonomously (Couzin & Krause, 2003; Sanchez *et al.*, 2012; Toner & Tu, 1995; Zhang *et al.*, 2010). Inspired by these systems, there has been a rise of interest in developing and building artificial systems made up of millimeter or larger scale components whose self-organization can be reprogrammed to accomplish a certain target structure (Brambilla *et al.*, 2013; Cademartiri & Bishop, 2015; Culha *et al.*, 2020; Wang *et al.*, 2017). However, these methods are based on components that have limited relationships with one another, and they value structural flexibility over structural stability to external pressures. As a result, reprogrammable self-organization still faces a basic problem: structural stability, which demands the system's solid-like rigidity, must be reconciled with structural fluidity so that the component units can redistribute themselves.

One promising way to address this problem is using vibrating particle systems. Granular particles densely packed within a confinement have a hard, solid-like structure as a result of jamming. However, if the particles are vibrated with sufficient force, the structure becomes liquidized, allowing particles to be redistributed. Specifically, anisotropic granular particles on a two-dimensional (2D) plate gain self-propulsion and tend to travel consistently in one direction indicated by the shape anisotropy. Such self-propelled 2D granular particles have been seen to display a variety of collective behaviors, including flocking (Deseigne *et al.*, 2010; Kumar *et al.*, 2014), clogging (Garcimartín *et al.*, 2015; Patterson *et al.*, 2017), crystallization (Briand *et al.*, 2018), and phase separation (Scholz *et al.*, 2018). In addition, it was discovered that the aspect ratio (AR) of the particle considerably modifies the collective phenomena, as ARs other than 1 result in local nematic alignment interactions via contact torques, which in turn result in propulsion direction alignment (Kudrolli *et al.*, 2008).

In this study, we aims to explore the redistribution of solid-like granular media in a state close to jamming through the utilization of a limited number of self-propelled particles (SPPs) possessing an elongated shape. To assess how effective manipulating the characteristics and quantity of SPPs is in the redistribution, we observe the dynamics of single or multiple SPPs placed among densely packed, randomly vibrated particles in a two-dimensional (2D) circular confinement space. Experimental results show that SPPs reach the boundary of the confinement via superdiffusion and form a moving or static cluster there. The superdiffusion reflects the quasi-long-range temporal correlations present in the axial motion. We find that the aspect ratio and polarity of the SPPs can significantly alter the cracking motion, which regulates their axial speed and travel trajectory in a dense environment. Our analysis elucidates the physical mechanisms underlying the ability of SPPs and particle clusters to penetrate and move through large numbers of nonpolar particles around them. This experiment is a simple yet effective approach for evaluating the potential of particle redistribution in artificial systems, revealing a unique strategy for regulating the collective motion of self-organized structures.

2.2 Experimental methods and materials

Each particle consists of two elliptical cylinders with a cap (5 mm high) and a body (6 mm high) joined on the same axis. For the circular particle, the diameters of the cap and body are 20 mm and 12 mm, respectively, and the cap and body of the elliptical particle have the same area as the corresponding parts of the circular particle. Eleven legs (8 mm long and 1 mm in diameter) are attached to the cap, which are inclined at equal angles, θ_{L}, of less than 10 degrees from the vertical direction. All particles are manufactured by stereolithography 3D printing using an acrylate-based transparent photopolymer. The accuracy of the 3D printer used in this work is around ±0.1 mm. To robustly track the position and orientation of some particles, we label their tops with one or two red squares. We then use the

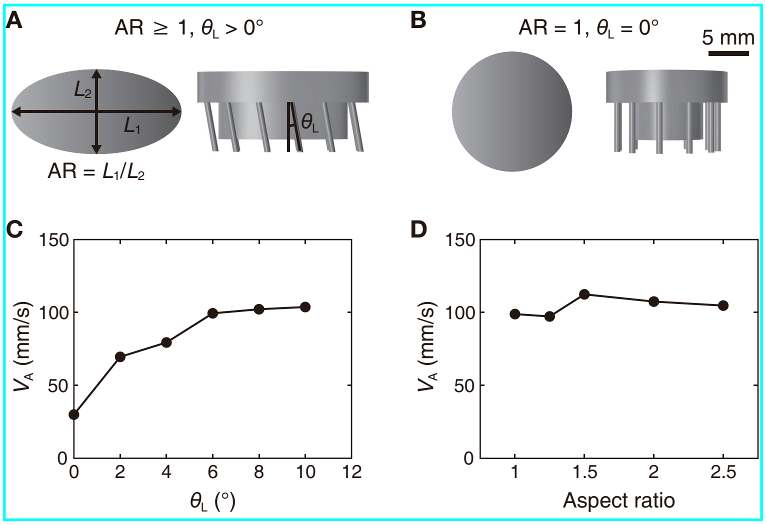

Figure 2.1: Design and speed of vibrated particles. **A**, The top and the side view of an elliptic polar particle. This particle becomes SPPs by vertical vibration. **B**, The top and the side view of a circular nonpolar particle. **C**, The time-averaged speed V_A as a function of leg tilt angle θ_L when AR $=$ 1. **D**, V_A as a function of AR when $\theta_L = 10^\circ$.

TrackMate plugin for ImageJ (Tinevez *et al.*, 2017) to track and analyze their trajectories.

The particles are excited by the vertical vibration of a circular acrylic baseplate (300 mm in diameter and 30 mm in height) attached to an electromagnetic shaker. The plate is maintained horizontal to within 10^{-3} degrees. The particle motion is constrained by an enclosing circular ring (diameter 300 mm). The shaker is linked to substantial concrete blocks to dampen vibrations. Experiments are conducted using vibrations with a frequency of $f = 80$ Hz and an amplitude of $A = 70$ μm, which ensures steady particle excitation. A fluctuating horizontal force is generated by the elastic deformation and restoring forces of the thin legs when they collide with the vertically vibrating plate, which propels the particle in the direction opposite of which its legs are tilted (Scholz *et al.*, 2016). Thus,

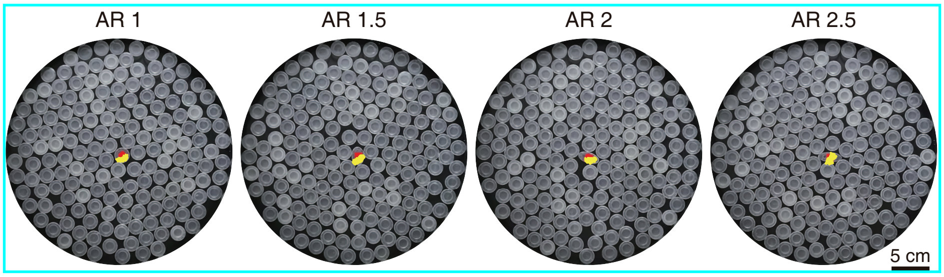

Figure 2.2: Trajectories of a single nonpolar particle initially placed at the center among a densely packed isotropic particles. The position of the particle is tracked for 3 minutes as the AR is adjusted.

polar particles with inclined legs (Fig. 2.1A) becomes SPPs that exhibit directional motion. Whereas, nonpolar particles with circular top and vertical legs (Fig. 2.1B) move randomly on the vibrating plate in an unbiased manner. The physical properties of the SPP can be controlled by changing the leg tilt angle θ_L and the AR of the top of the ellipse. In the absence of obstruction by other particles, the axial velocity of the SPP increases with θ_L but does not vary significantly with AR (Fig. 2.1C and 2.1D).

2.3 Single SPP in a bulk

We first observe how a single SPP moves among a large number of vibrating particles. To do this, we filled the circular arena with area fraction η of 75% with a single SPP and the rest with nonpolar particles. Considering that the maximum area fraction reaches around 81% when filling a circular confinement with circular particles (Graham *et al.*, 1998), the fraction of 75% represents a very dense system while still provides the possibility for particles to move and switch position. The high packing density is identified through the motion of the nonpolar particles constituting the granular medium. When the vibration is activated, an isotropic nonpolar particle initially placed in the center of the circular confinement barely moves from

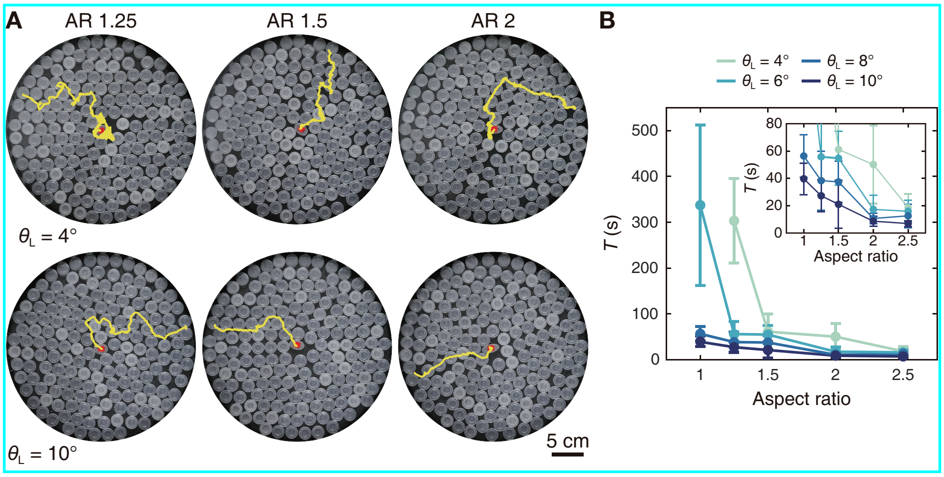

Figure 2.3: Motion of a single SPP initially positioned at the center of tightly packed nonpolar particles. **A**, The trajectories of a single polar particle with different leg tilt angle (θ_L) and the aspect ratio (AR). **B**, The time to reach the boundary T as AR and θ_L are altered. The error bars show standard deviation.

its initial position (Fig. 2.2). The virtual lack of diffusion shows that the isotropic particles are jammed, i.e., they scarcely swap places with one another. However, under the same conditions, the SPP exhibits stochastic motion among the isotropic particles, always reaching and remaining at the confinement's boundary the majority of the time (Fig. 2.3A). This indicates that the SPP which penetrates through the granular medium of isotropic particles disrupts the jammed state. The SPP's trajectories clearly show the importance of θ_L and AR: higher θ_L or AR produces straighter trajectories, whereas lower θ_L or AR produces more wavy trajectories.

Their quantitative impacts are more visible in the time T for the SPP to reach the boundary, which reduces quickly as the SPP's θ_L or AR increase (Fig. 2.3B). Besides, the time T is also highly dependent on the granular packing density, as easily expected. Fig. 2.4 shows a significant increase in T just by increasing the area fraction η by 75% to 3% points, and also

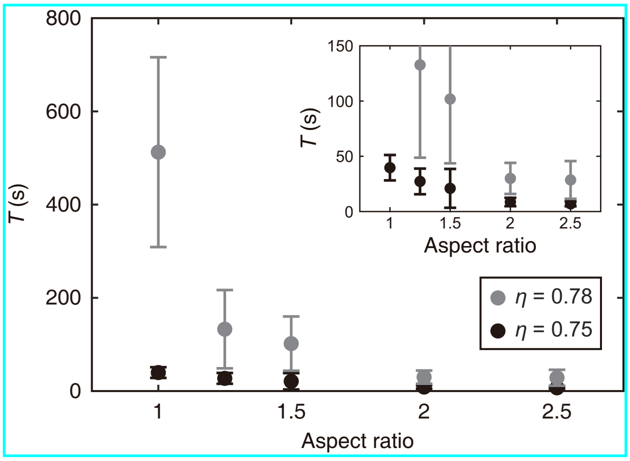

Figure 2.4: The time T it takes for particles with $\theta_{\mathrm{L}} = 10^{\circ}$ to reach the boundary under two area fractions η.

shows that T rapidly decreases with AR at both area fractions. These findings contradict what one might predict given the axial velocity of an isolated SPP, which increases by little more than 20% as θ_{L} is increased from 4° to 10° and minimally changes with the AR (Fig. 2.1C). In other words, when the granular media is jammed, the SPP's motion becomes significantly more sensitive to its controllable physical properties. Here, we note that the SPP with low θ_{L} can hardly move at high packing density (η = 0.78) even at high AR. Therefore, we proceed with future experiments by fixing η = 0.75 to clarify both the effects of θ_{L} and AR.

The time to reach the boundary is determined by the speed and distance the particle travels; the more complex the particle's path, the longer it takes to reach the boundary. The influence of AR and θ_{L} on travel distance S and time-averaged speed V_{A} demonstrates that θ_{L} has a relatively strong effect on particle mobility and that AR affects both the travel route and particle mobility (Fig. 2.5). Here, the path is strongly influenced by the rotational motion of the particle, which causes frequent changes in direction of motion and results in longer travel distance to the boundary. Increases in AR and θ_{L} reduce particle's rotational diffusion because vertical movement

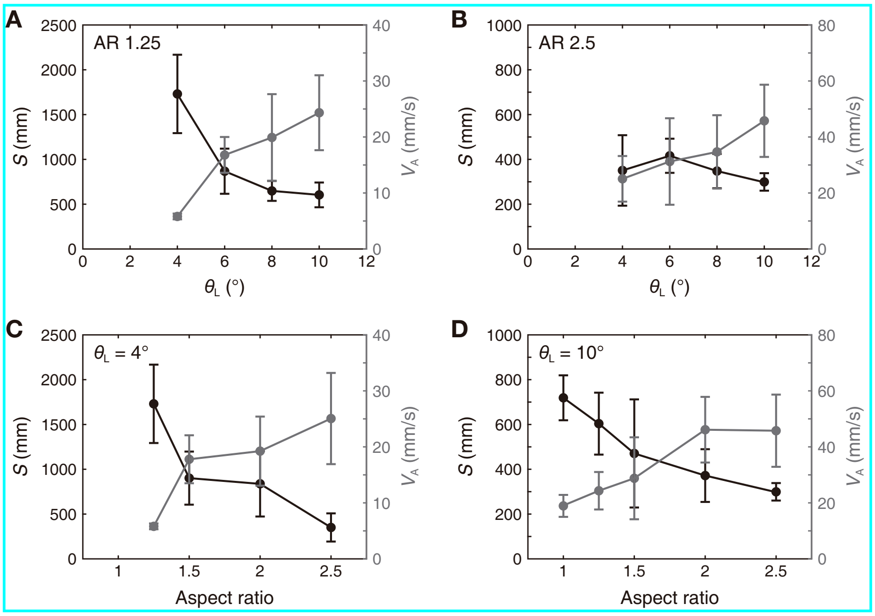

Figure 2.5: Traveled distance and the time-averaged speed of a single SPP from the center to the boundary. The time-averaged speed V_{A} for different θ_{L} at (**A**) low and (**B**) high AR, and for different AR at (**C**) low and (**D**) high θ_{L} are shown.

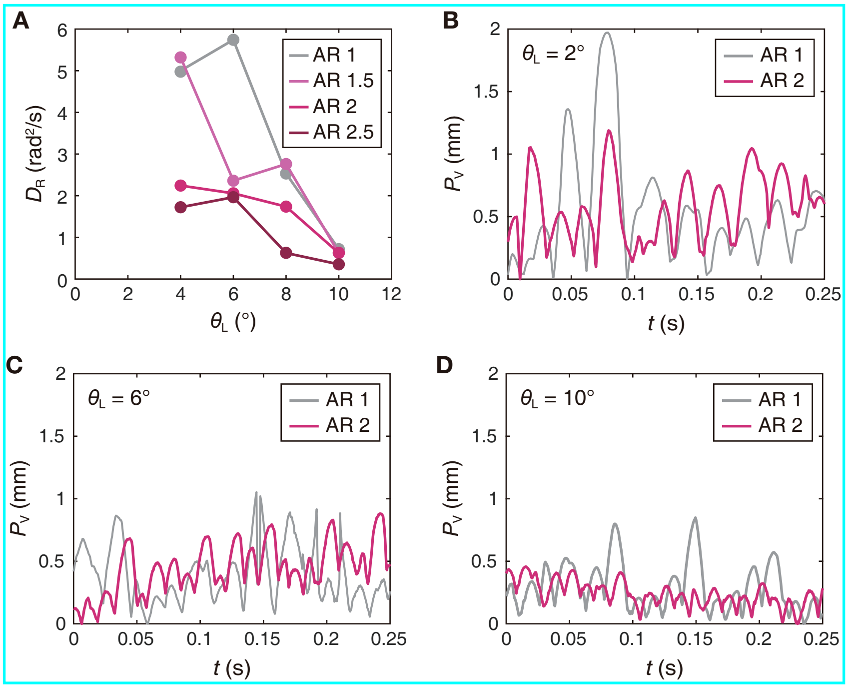

Figure 2.6: Rotational and vibrational properties of a single SPP. **A**, Rotational diffusion coefficient D_{R} tends to decrease with AR and θ_{L}. **B-D**, Change of the vertical position P_{V} of the SPP as the AR and θ_{L} are varied.

by vertical vibration becomes modest at high aspect ratio and leg tilt angle (Fig. 2.6). High AR particles, in particular, are substantially constrained in rotational motion by neighboring particles in a dense environment, which reduces the total travel distance.

To further characterize the dynamics of a single SPP in a dense environment, we measured the time-averaged mean square displacement (MSD), which is defined as

$$\langle \overline{\Delta \mathbf{r}(t)^2} \rangle \equiv \left\langle \frac{1}{T-t} \int_0^{T-t} dt' \left[\mathbf{r}(t+t') - \mathbf{r}(t') \right]^2 \right\rangle . \tag{2.1}$$

Here, $\mathbf{r}(t)$ denotes the location of the SPP at time $t \geq 0$, and $\langle \cdots \rangle$ represents the ensemble average over different samples. Except for SPPs with low θ_L and AR which show subdiffusive behavior (Fig. 2.7A), the SPPs exhibits superdiffusion $\langle \overline{\Delta \mathbf{r}(t)^2} \rangle \sim t^\gamma$ with $1 < \gamma < 2$ for a time interval up to the order of seconds (Fig. 2.7A and 2.7B), which eventually passes into the normal diffusion ($\gamma = 1$) as time goes on. The diffusion exponent γ increases with AR, which is consistent with the visual observation (Fig. 2.3A) that the SPPs with a larger AR tend to exhibit a straighter trajectory. Such superdiffusion indicates that the motion of SPP contains substantial long-range temporal correlations.

2.4 Analysis of cracking force

We see that the mobility in dense environments increases with AR, which means that sharper SPPs can crack the cage more easily. A step-by-step view of this cracking motion is shown in Fig. 2.8A, where we can see that the SPP marked in red finds and widens the gap between a pair of adjacent nonpolar particles highlighted by the yellow dashed line. To illustrate how an increase in AR enhances cracking motion, we calculated the cracking force P exerted by an SPP (with a self-propulsion force F) that widens the gap b between two isotropic particles in front of it. The forces acting on the two particles are shown in Fig. 2.8B, with the yellow

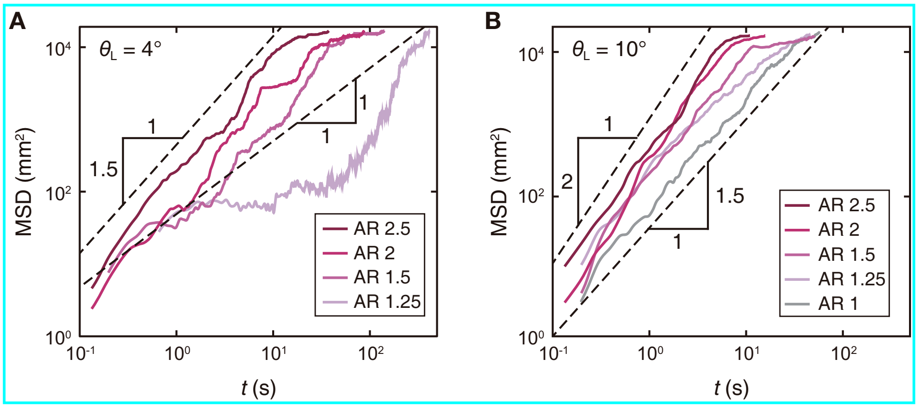

Figure 2.7: The time-averaged mean squared displacement (MSD) of the polar particle. **A**, MSD of a single SPP with $\theta_{\mathrm{L}} = 4^{\circ}$. **B**, MSD of a single SPP with $\theta_{\mathrm{L}} = 10^{\circ}$.

and blue borders indicating the particles marked with the same colors in Fig. 2.8A. For simplicity, we assumed that (1) the particles colored blue in Fig. 2.8A behave like a wall exerting normal and friction forces on the particles and (2) the system is in static mechanical equilibrium conditions.

Neglecting inertial effects establishes the following relationships for the forces and torque,

$$F_1 \cos\theta + \mu F_1 \sin\theta = F_2 + f_3 = \frac{F}{2}, \tag{2.2}$$

$$F_1 \sin\theta - \mu F_1 \cos\theta - \mu F_2 = P, \tag{2.3}$$

$$\mu F_1 + f_3 = \mu F_2, \tag{2.4}$$

where μ is friction coefficient between particles and θ is the angle between the x-axis and the line joining the center of the circle and the point of contact (X, Y). Using the three relationships, we can relate the cracking

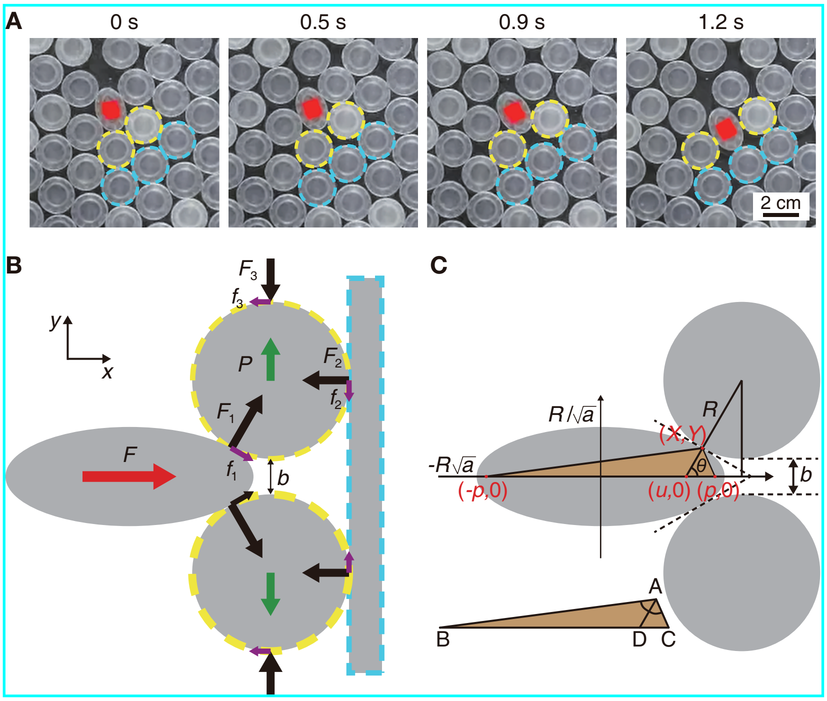

Figure 2.8: Analysis of the effect of aspect ratio on cracking ability. **A**, Images of a single SPP (marked in red) penetrating the gap between two nonpolar particles (yellow dotted circles) in front. **B**, Schematic of the forces applied by the SPP on the two nonpolar particles. **C**, Coordinate system corresponding to **B** for calculating the force P that widens the gap b. An elliptic SPP has an aspect ratio of a.

force P to F, θ, and μ by

$$P = \frac{F}{2}\left[\frac{\sin\theta - \mu\cos\theta - \mu^2/\left(\mu+1\right)}{\cos\theta + \mu\sin\theta} - \frac{\mu}{\mu+1}\right], \tag{2.5}$$

where $\sin\theta$ and $\cos\theta$ is $Y/\left[(X-u)^2+Y^2\right]$ and $(X-u)/\left[(X-u)^2+Y^2\right]$, respectively. The elliptic perimeter of the horizontal SPP centered at the origin is expressed by the following equation,

$$\frac{x^2}{a\,R^2} + \frac{a\,y^2}{R^2} = 1, \tag{2.6}$$

which includes the point of contact $(X,\,Y)$ as well. Meanwhile, considering a line through the center of the circle adjacent to the tangent point, let us denote the intersection between the line and the x-axis by $(u,\,0)$. A feature of an ellipse where the triangle in Fig. 2.8C satisfies $\overline{\mathrm{AB}} : \overline{\mathrm{AC}} = \overline{\mathrm{BD}} : \overline{\mathrm{DC}}$ implies

$$\frac{(X+p)^2+Y^2}{(X-p)^2+Y^2} = \frac{(p+u)^2}{(p-u)^2}\,. \tag{2.7}$$

The locations of two foci of the ellipse $(\pm p\ ,0)$ satisfy $p = R\sqrt{a-a^{-1}}$. Using this property, Eq. (2.6), and Eq. (2.7) along with the appropriate root of the quadratic equation, we can represent u through X by

$$u = X\left(1-\frac{1}{a^2}\right), \tag{2.8}$$

which allows us to express Y and u as functions of X. Now, we consider the gap between two circular particles, b. From the geometry of the ellipse, we can write $b = 2(Y + R\sin\theta - R)$, where Y can be expressed in terms of X by Eq. (2.6). We use Eq. (2.8) to eliminate θ, which gives

$$\sin\theta = \frac{\sqrt{R^2/a-(X/a)^2}}{\sqrt{X^2/a^4+R^2/a-(X/a)^2}}, \tag{2.9}$$

$$\cos\theta = \frac{X/a^2}{\sqrt{X^2/a^4+R^2/a-(X/a)^2}}\,. \tag{2.10}$$

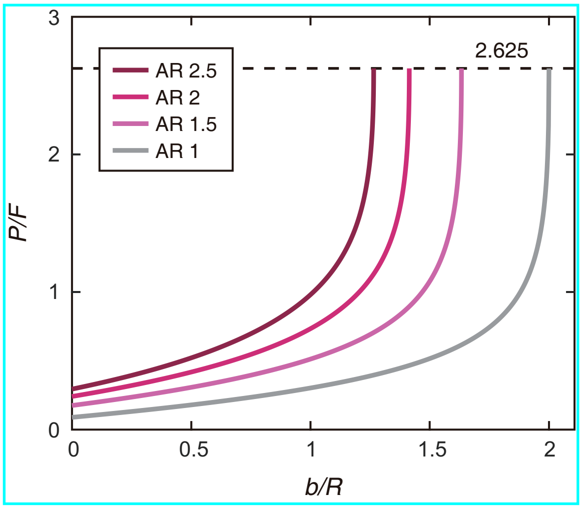

Figure 2.9: The relative magnitude of the cracking force P/F applied by a single SPP with different AR as the gap b is varied. Each curve ends when the gap reaches the thickness of the SPP with each AR.

Substituting Eqs. (2.9) and (2.10) into Eqs. (2.5) and b, we obtain the curves of P as a function of the AR and the gap b. The result using an experimentally measured interparticle friction coefficient $\mu = 0.18$ is shown in Fig. 2.9 where the cracking force increases monotonically with AR and b. The cracking force of the SPP with AR = 2.5 is approximately 3 times stronger than that of the circular SPP for $b/R < 1$, and it increases rapidly as b approaches the thickness of the SPP, eventually reaching about 2.6 times the propulsion force. The smaller P for narrower spacing reflects that cracking becomes more difficult in dense environments. These results confirm our observation that the shape of the SPP has a strong influence on its mobility through its cracking ability and rotational properties.

2.5 SPPs at circular boundary

Now we'll discuss how the SPP moves once it reaches the confinement boundary. If there is no SPP, a nonpolar particle remains at the boundary

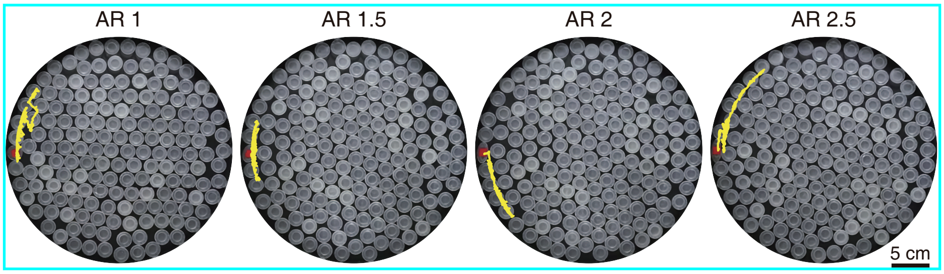

Figure 2.10: Trajectories of a single nonpolar particle initially placed at the boundary. The position of the particle is tracked for 3 minutes as the AR is adjusted.

and diffuses only along the boundary, as depicted in Fig. 2.10. This again verifies that the granular system meets the jamming condition, i.e., the relative locations of the particles do not change, despite the possibility of rotational diffusion in the entire cluster. In contrast, the SPP exhibits significantly faster motion through the granular media at the boundary (Fig. 2.11A). The SPP tends to linger near to the boundary, as expected for a particle whose direction of motion demonstrates a degree of persistence (Li & Tang, 2009). But the AR and θ_{L} determine how close the SPP keeps to the boundary. Because the self-propulsion force rises monotonically with θ_{L} below 10°, the SPP is likely to travel along the boundary more quickly as θ_{L} is increased. On the other hand, because the cracking ability and orientational persistence of the SPP both increase with the AR, the SPPs with a higher AR tend to remain closer to the boundary (Fig. 2.11A and 2.11B). However, we also notice that, once the SPP leaves the boundary, it wanders further into the confinement's center when the AR is higher (Fig. 2.11B), despite the fact that such instances are uncommon. This behavior is also a result of the greater breaking capability and orientational persistence of SPPs with a higher AR. When not leaving the boundary, the speed of the SPP moving along the boundary increases with AR and θ_{L} (Fig. 2.12).

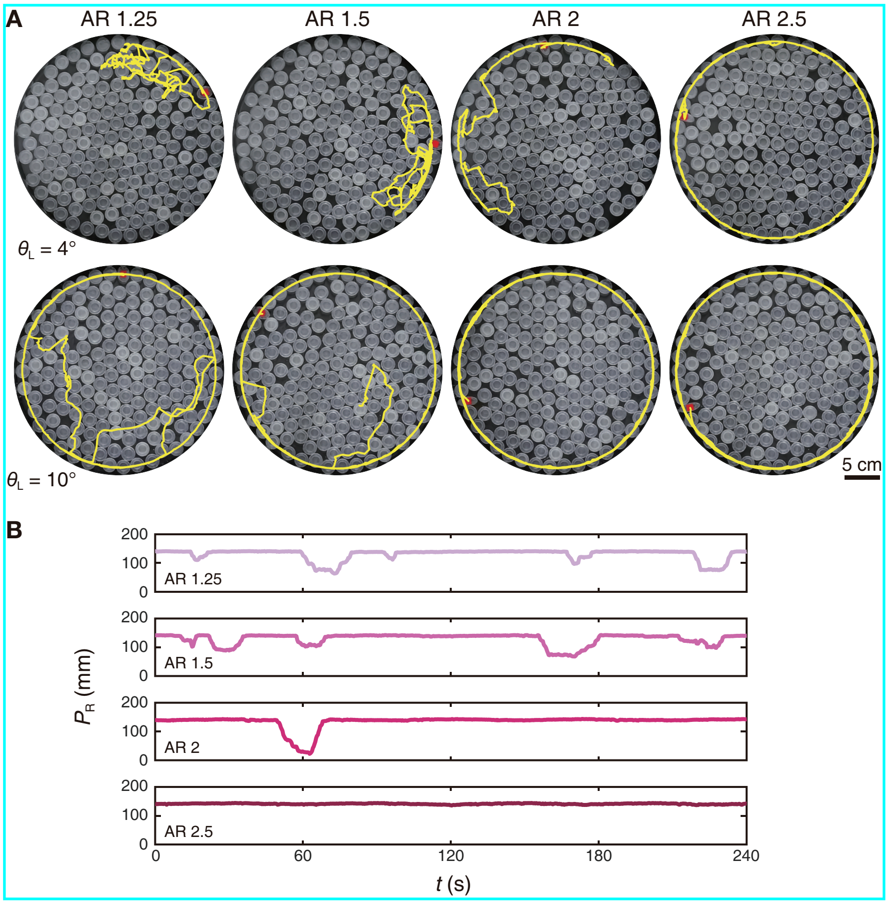

Figure 2.11: Motion of a single SPP after reaching the boundary. **A**, The trajectories of a single SPP with different AR and leg tilt angle θ_{L} for 3 minutes after reaching the boundary. **B**, The time evolution of the radial position P_{R} of the SPP with $\theta_{\mathrm{L}} = 10^{\circ}$.

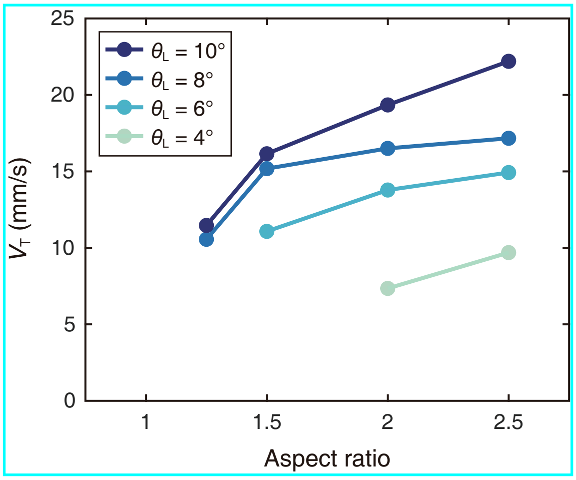

Figure 2.12: The averaged tangential velocity V_T of the SPP along the boundary. The velocity is calculated only for particles moving over 30 seconds without stopping or leaving the boundary.

We now consider the case where two SPPs are moving along the boundary. For this aim, we place two SPPs with AR $= 2.5$ and $\theta_L = 10^\circ$. When SPPs moving in opposite directions collide at the boundary, they may simply pass by (Fig. 2.13A) or one of them may leave the boundary and move to the bulk (Fig. 2.13A). The two processes are repeated until the SPPs are moving in the same direction along the boundary. If the two SPPs proceed in the same direction, they tend to remain near to each other and maintain their initial direction of movement after the collision (Fig. 2.13C). Only a cluster of SPPs traveling in the same direction can form a stable structure, which becomes the attractor of the SPPs' collective dynamics.

Based on the result of two SPPs, we investigate the collective behavior of numerous SPPs in a dense granular media confined by a circular boundary. We place several SPPs in the bulk of the previously described experimental system, with each SPP substituting a single isotropic particle so that the total number of particles and packing fraction remains at 170 and 75%, respectively, as in the single-SPP studies. As shown in Fig. 2.14A, when

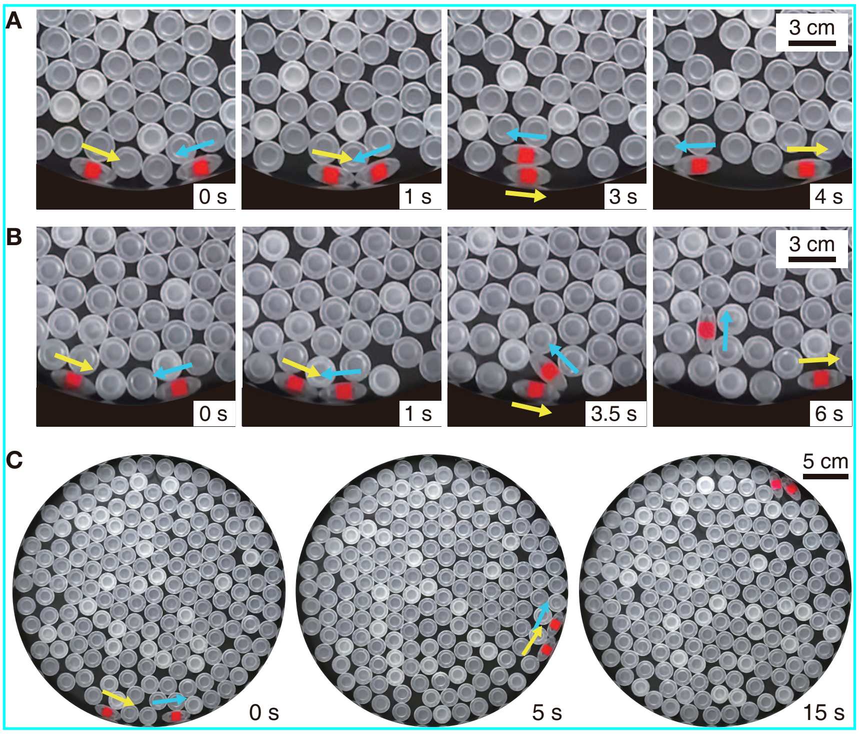

Figure 2.13: Motion of two SPPs after collision at the boundary. A pair of SPPs going in opposite directions may either (**A**) pass each other and move back along the boundary or (**B**) get dispersed with one particle moving into the bulk. **C**, Two SPPs travelling in the same direction tend to form a single cluster and move together.

the vibration is turned on, all SPPs travel from the bulk to the boundary (for $t < 40$ s). Then the SPPs collide with each other at the boundary and gradually merge into a single large cluster ($40 < t < 80$ s) and move together along the boundary ($t > 80$ s). The cluster in Fig. 2.14A gives us a clue to how a cluster of SPPs can persistently move in a single direction along the boundary. For $t > 80$ s, we observe that the SPPs constituting the cluster are asymmetrically inclined from the radial direction. For instance, the rearmost SPP, denoted by a yellow arrow, has a substantial tilt which indicates that the particle leans almost entirely against the confinement boundary. In contrast, the leading SPP leans against an nonpolar particle in front and tilts only slightly. The geometry implies that the rearmost SPP exerts a high forward force on the cluster, whereas the frontmost SPP exerts just a modest resistance to the cluster's motion. This force imbalance propels the cluster ahead, causing the nonpolar particle in front of the cluster to adhere more strongly to the leading SPP. Thus, despite the microscopic noise, the leading SPP maintains a restricted tilt, preserving the cluster's asymmetry. In short, a positive feedback exists between the structural asymmetry and the motility of the SPP cluster, allowing it to maintain a prolonged motion through spontaneous symmetry breacking. This state of motion is referred to as the moving phase.

However, the aforementioned mechanism fails to maintain the cluster's mobility when the number of SPPs, N, exceeds critical number. Fig. 2.14B illustrates the behavior of the SPP cluster where $N = 8$. For $0 < t < 3$ s, the cluster's motion is maintained by the aforementioned positive feedback mechanism. At approximately $t = 3$ s, however, the nonpolar particle in front of the cluster moves sufficiently far away from the leading SPP. This enables the frontmost SPP to lean completely against the boundary, resulting in the rearmost and frontmost SPPs exerting approximately the equal magnitude of force in opposite directions on the SPP cluster. Consequently, the SPP cluster acquires a symmetrical form and loses its persistent mobility. This state of motion is referred to as the static phase.

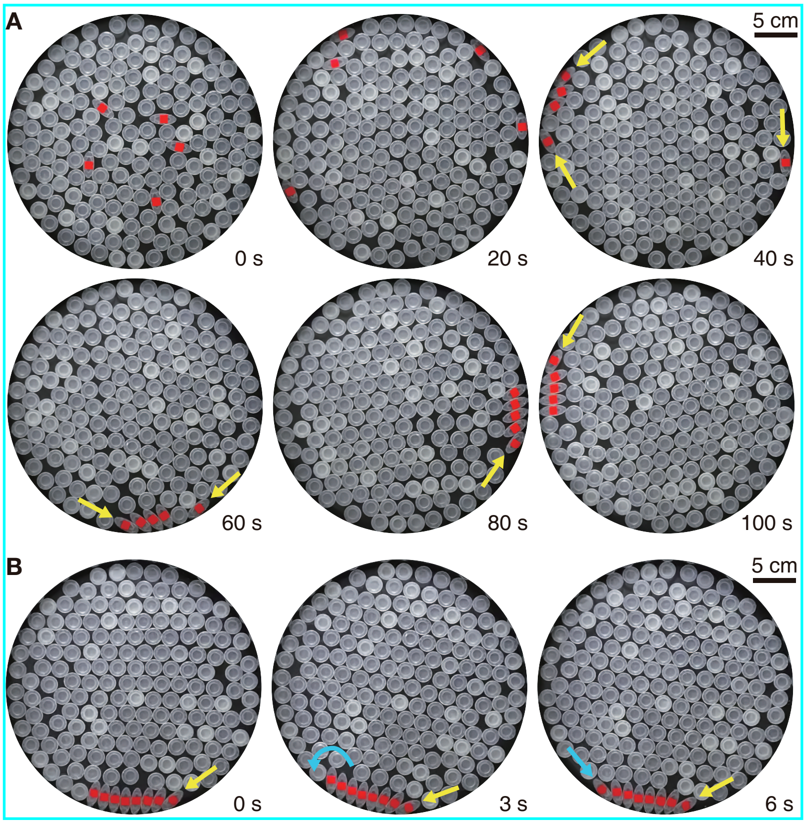

Figure 2.14: Collective motion of multiple SPPs. **A**, Five SPPs initially positioned in the bulk approach the boundary and form a cluster with permanently asymmetric configuration and unidirectional movement. **B**, A moving cluster of eight SPPs becomes immobile after the leading SPP reverses its direction and restores the symmetry. All polar particles used in **A** and **B** have AR $= 2.5$ and $\theta_{\mathrm{L}} = 10^{\circ}$.

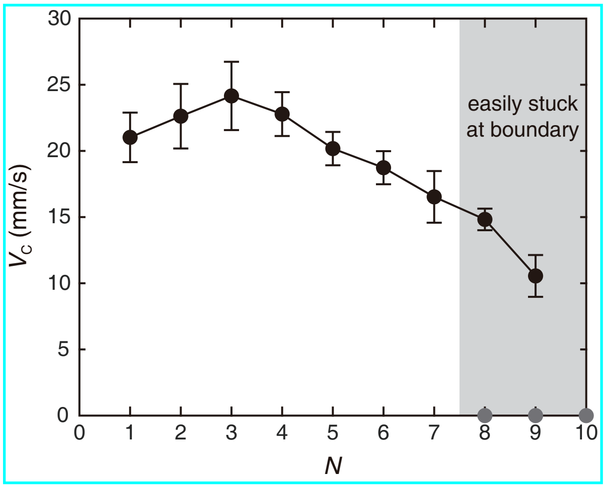

Figure 2.15: The averaged cluster velocity V_{C} with increasing number of SPP, N. The black points correspond to the velocity measured when the cluster moves persistently in one direction for more than 2 minutes. Whereas, the gray points represent that the clusters with $N > 7$ mostly get stuck at the boundary after 5 minutes of observation time. All polar particles forming the cluster have AR = 2.5 and $\theta_{\mathrm{L}} = 10^{\circ}$.

We then study how does the amount of SPP influence the phase of the SPP cluster, and what is the nature of the phase transition from moving to static. As shown in Fig. 2.15, the velocity of the SPP cluster V_{C} tends to decrease with N for more than three particles. We see numerous metastable values found for $N > 7$, where the SPP cluster may exhibit an extended period of persistent motion, which eventually becomes static as the leading particle flips over to restore the cluster's symmetry via the mechanism explained above. After that, the cluster becomes immobile, never moving again during the time of observation. These observations, in particular the coexistence of several metastable states of motion over a range of N, imply that the transition between the dynamic and static phases is discontinuous. This is further supported by the results depicted in Fig. 2.16, in which the moving phase and the static phase appear to coexist for $N \geq 7$, with the static phase becoming more probable than the moving phase as N increases from 7 to 8.

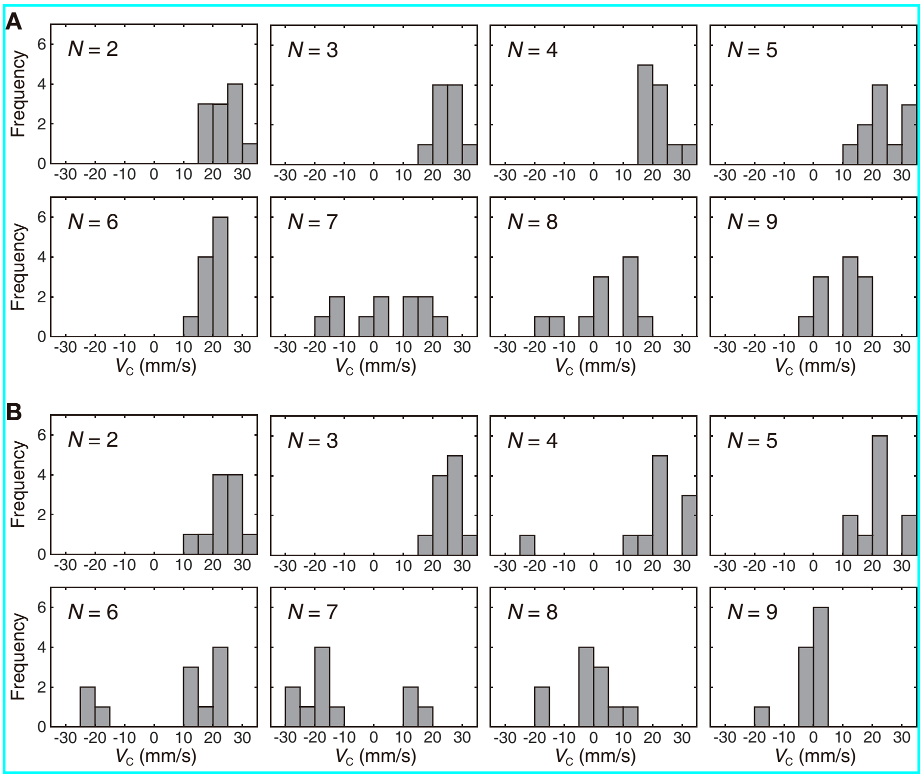

Figure 2.16: Changes in distribution of short-term cluster velocity V_C along the boundary with time. The velocity is measured (**A**) 30 seconds and (**B**) 5 minutes after the cluster starts to move in one direction. Each velocity is time-averaged for 5 seconds before and after each time stamp.

2.6 Conclusions

We have reported experimental data demonstrating how the easily modifiable characteristics of the SPPs, such as their AR and number, greatly alter their individual and collective behavior in a vibrated dense granular medium. In the absence of a granular medium, the motion of a single SPP on a vibrating plate can be accurately described as active Brownian motion with a substantially constant axial velocity and weak rotational diffusion, as previously reported (Deseigne *et al.*, 2010, 2012). As depicted in Fig. 2.1 and Fig. 2.6, the velocity and rotational diffusion coefficient of the SPP do not demonstrate a strong dependence on its AR, particularly when the self-propulsion is strong enough ($\theta_L > 5^\circ$). However, when surrounded by a dense granular medium of isotropic particles, we showed that the AR greatly influences both the axial and rotational components of the SPP's motion through cage formation and cracking. As a result, in the presence of the dense granular media, the easily tunable microscopic properties of the SPPs have a far higher impact on the self-organization process than in the absence of it.

Previous studies have shown that a large amount of SPPs create a long-range orientational order via direct mechanical interactions (Deseigne *et al.*, 2010, 2012) or indirect interactions mediated by the granular medium (Kumar *et al.*, 2014). This process, known as flocking, requires the system's confining boundary to be designed in such a way that SPPs easily adhering to the boundary are constantly steered back into the bulk. Without such boundary condition, the SPPs eventually form a static cluster that adheres to the boundary and moves infrequently as a whole, inhibiting the creation of a flock. This corresponds exactly to the static cluster at the boundary for large N mentioned in Section 2.5. Because these studies only looked at a system with a large number of SPPs, they overlooked the possibility of a small number of SPPs forming a motile cluster whose polarity and cohesion are preserved by the surrounding dense granular medium.

Our findings pave the way for a number of intriguing future studies. First, the precise relationship between the SPPs' self-organized structure and the physical properties of the surrounding granular media remains unknown. While the enhanced effects of the SPP's shape on its dynamics and the formation of the traveling cluster at the boundary appear to require the presence of caging (i.e., the granular medium must be dense enough to be glassy), we still need to investigate how these phenomena change depending on the granular medium's packing fraction and vibration protocols. It would be fascinating to see if local adjustments in the vibration protocols can allow us to regulate the form of the self-organized structure in a way similar to how swimming bacteria produce light-induced patterns. Second, we can investigate the system's self-organization behaviors for a non-rigid confinement boundary. We anticipate that such systems will exhibit a diverse spectrum of collective dynamics as a result of feedback between SPP ordering and membrane deformation. Their activities may also provide information about the dynamical features of cells and vesicles, which are crowded systems made up of diverse SPPs surrounded by flexible membranes. Finally, we must determine whether our conclusions apply to cases when the particles are even softer and hence more flexible. This could provide a physical picture of how highly motile and invasive cells spread within a confluent tissue of epithelial cells, with implications for morphogenesis and cancer metastasis (Grosser *et al.*, 2021).

Chapter 3

Dense particle structures with switchable behavior via redistribution of vibrated particle clusters

In the previous chapter, we have introduced our dense granular system where easily tunable characteristics of the self-propelled particles (SPPs), such as their polarity, aspect ratio (AR) and amount of particles, significantly change their individual and collective dynamics. Based on the results, we show that our system can be used to create dense structures exhibiting diverse behahviors. Confining active particles in a free-to-move boundary is an emerging strategy to create particle structures capable of directed motion and shape change. Many active particle ensembles with low packing density have been proposed that can move and deform through internal stress or external stimuli; nonetheless, structures with particles close to the jamming condition have been rarely studied. Such densely packed systems are structurally robust and thus advantageous to operate in high-stress environments. Here, we present rigid particle structures consisting of

a mobile boundary enclosing a few SPPs and randomly vibrated nonpolar particles. We investigate how and why changing the variables that make up a dense particle structure influences its behavior. First, tuning the shape and amount of SPPs makes the structures exhibit diverse behaviors ranging from random, rotational to directional motion. Second, changing particle packing density and mechanical properties of the boundary additionally modulate the dynamic properties – the magnitudes of polarity and chirality – of these structures. Our study paves the way for significant regulation of cluster behavior with small changes in the components of dense systems.

3.1 Introduction

Programmable active matter and swarm robotics use ensembles of simple, independent particles to perform tasks beyond the scope of individual units (Brambilla *et al.*, 2013; Culha *et al.*, 2020; Rubenstein *et al.*, 2014). From contact-mediated approaches (Li *et al.*, 2019, 2021) to collective response to external fields (Jin *et al.*, 2019; Wang *et al.*, 2022; Zhang *et al.*, 2021), a variety of interactions have been proposed for units to cooperate to reach this goal. A promising approach for creating functional structures is to enclose cluster of active agents with stiff or flexible boundaries (Abaurrea-Velasco *et al.*, 2019; Deblais *et al.*, 2018). These structures acquire translational or rotational mobility when the internal units exert an asymmetric force on the boundary. Most of these structures are composed of low number densities that allow units to be skewed to one side or mechanically interact with neighboring units, resulting in structure motion (Boudet *et al.*, 2021; Savoie *et al.*, 2019). Although the low-density and flexible boundary enables for the structure to be deformable, which allows for functions like space exploration, it also implies that these structures may undesirably be constrained in a small space or change their shape and functions when exposed to external stress.

Despite the advantages of structural stability and reliability, it remains much less explored to develop multimodal systems with densely packed particles within confinement, except for the possibility of rotational motion (Liu *et al.*, 2020; Paoluzzi *et al.*, 2016; Vincenti *et al.*, 2019). One of the fundamental difficulties in creating dense structures with various behaviors is to change the position, orientation, and alignment of the particles that can affect structure behavior. Highly confined active particles are prone to dense clogging or crystal formation that easily prevents component flow (Briand *et al.*, 2018; Patterson *et al.*, 2017). We showed in the previous chapter that particles with high polarity and aspect ratio placed in densely packed nonpolar particle move well from the center to the boundary, and that the motion along the boundary varies depending on the number of SPPs. This result shows the possibility to modulate the behavior of dense particle clusters by changing shape and polarity of some particles.

Here, we investigate how manipulating the components that make up a densely packed particle structure affects its behavior and what the underlying mechanism is. we characterize experimentally the dynamic properties of the structure made by filling the inside of a thin boundary with randomly vibrated, nonpolar particles including some self-propelled particles (SPPs). All experiments are performed with the particles and settings introduced in chapter 2. The behavioral characteristics of the structure are shown to be closely related to SPPs' ability to pass through the dense surrounding particles. We next explore how the number of SPPs, which affects their orientation with respect to the boundary wall, controls the polarity and chirality of the structure. It appears that particle packing density and boundary properties further fine-tune the behavior of the dense particle structure.

3.2 Particle structures with a single SPP

To explore the prospect of manipulating the behavior of dense structures, we begin to investigate the dynamics of densely packed, nonpolar particle cluster containing a single SPP confined in deformable and mobile boundary. If the SPP has a limited cracking ability, i.e., low aspect ratio

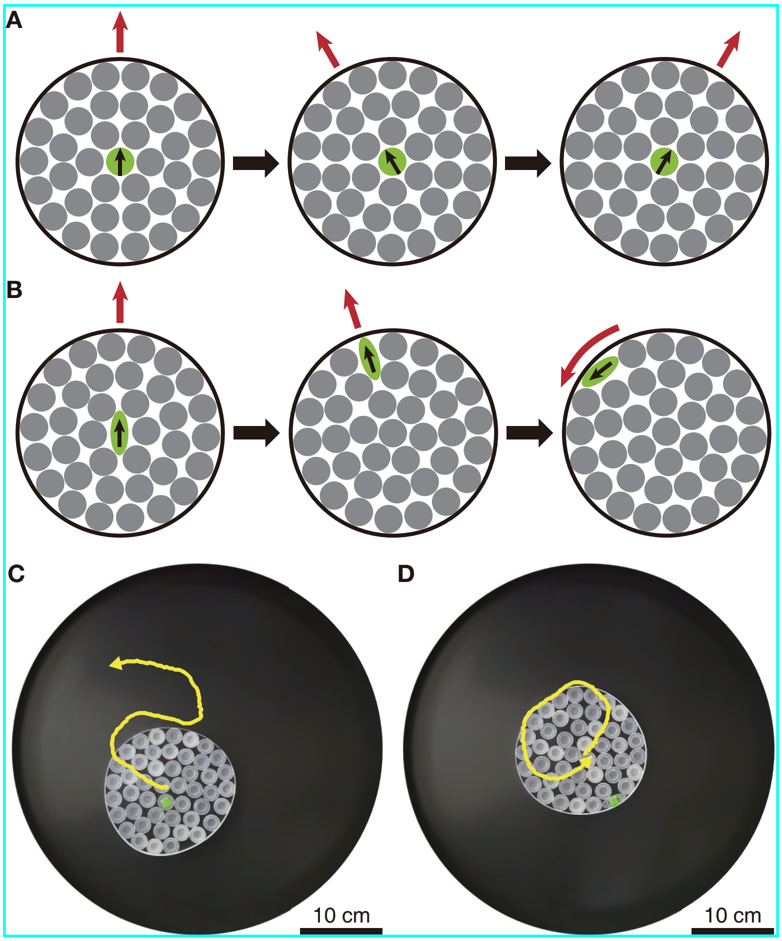

Figure 3.1: Dynamics of dense particle structures containing a single SPP. Movement direction of structures containing an initially centered, single polar particle with (**A**) low and (**B**) high cracking ability. Trajectories of structures containing a single SPP (marked in green) with an aspect ratio of (**C**) 1 and (**D**) 2.5, where the diameter of the boundary is $D = 155$ mm. The trajectory in (**D**) shows the motion after the SPP reaches the mobile boundary.

(AR) or polarity, it pushes surrounding nonpolar particles rather than penetrating them. The propulsion of the SPP causes the structure to move in the orientation of the SPP, and the SPP's rotation modifies the movement direction. Thus, the structure behaves as one large, slow SPP (Fig. 3.1A).

In contrast, if the SPP in the structure has a strong cracking ability due to its high AR and polarity, the SPP passes through the nearby nonpolar particles and reaches the boundary of the structure. This SPP moves along the boundary, making the structure's outermost particles to rotate along the boundary. As a result, the structure follows the SPP's direction until the particle reaches the boundary, and once the SPP moves along the boundary, the structure possesses chirality in the direction of the SPP's movement (Fig. 3.1B). Fig. 3.1C shows the behavior of a structure having a single SPP with an AR of 1 in its center. The structure moves while turning in both directions, demonstrating that the structure has polarity with some rotational degrees of freedom. The behavior after a single SPP with an AR of 2.5 reaches the boundary is shown in Fig. 3.1D. The structure moves in a circle in one direction, revealing its chirality.

3.3 Particle structures with multiple SPPs

If the particle structure contains two SPPs, the particles meet over time at the boundary and then move together. The movement of these SPPs causes the structure to move in a circle of a certain radius (Fig. 3.2). Here, the rotational motion can be divided into pure translational motion and pure rotational motion. The pure rotational motion involves the rotational motion of the inner particle cluster and the outer boundary. The structure with the radius of R moving along the radius of r_m at the translational speed v, the inner rotational velocity $w_\mathrm{i} = \theta_\mathrm{i}/t$, and the outer rotational velocity $w_\mathrm{o} = \theta_\mathrm{o}/t$ is schematically shown in Fig. 3.3. Yellow right triangle gives r_m:v=r_m+R:v+Rw_i or r_m=v/w_i, which indicates that r_m represents the polarity of the rotating structure.

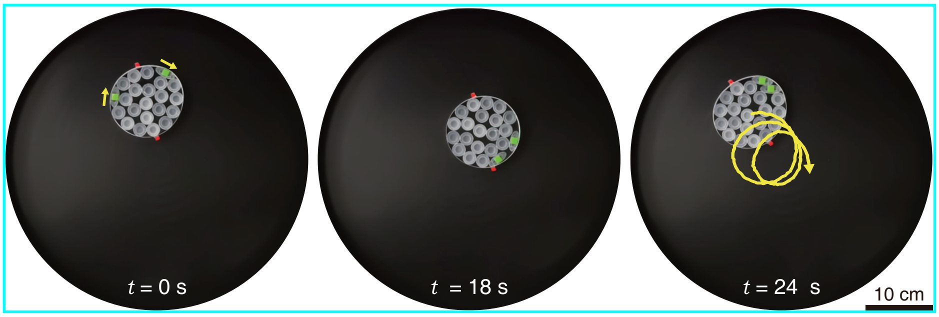

Figure 3.2: A particle structure containing two SPPs moving along the boundary. A total of 22 particles fill the circular boundary of $D = 110$ mm. After the two SPPs meet ($t > 24$ s), the structure continues to rotate in a nearly constant radius.

To quantify how the number of SPPs N_p affects the behavior of the dense particle structures, we measure the dynamic properties v, w_i, w_o, and r_m by increasing N_p while the packing fraction η is fixed. The structure's translational speed v increases roughly linearly as SPPs replace nonpolar particles (Fig. 3.4A). This result is easily expected because the momentum of the structure is increased by the addition of SPPs. In the case of rotational motion, the structure begins to rotate when a single SPP is introduced, and further addition of SPP causes the two rotational velocities w_i and w_o steadily rise (Fig. 3.4B). In contrast, the rotation slows down when a fourth SPP replaces the nonpolar particle, demonstrating that there exists an optimal N_p for maximum rotational velocity. Fig. 3.4C shows that the ratio of w_o and w_i is not constant depending on N_p; $w_\mathrm{o}/w_\mathrm{i}$ is greater when the structure has two or more SPPs than when it has one. This ratio reveals the degree to which the inner particles interact with the mobile boundary, indicating that the interaction between particles and the boundary is greater when the structure has many SPPs. The number of SPPs also change the radius of structure motion. We calculate the average radius by dividing the distance the structure has moved by the angular

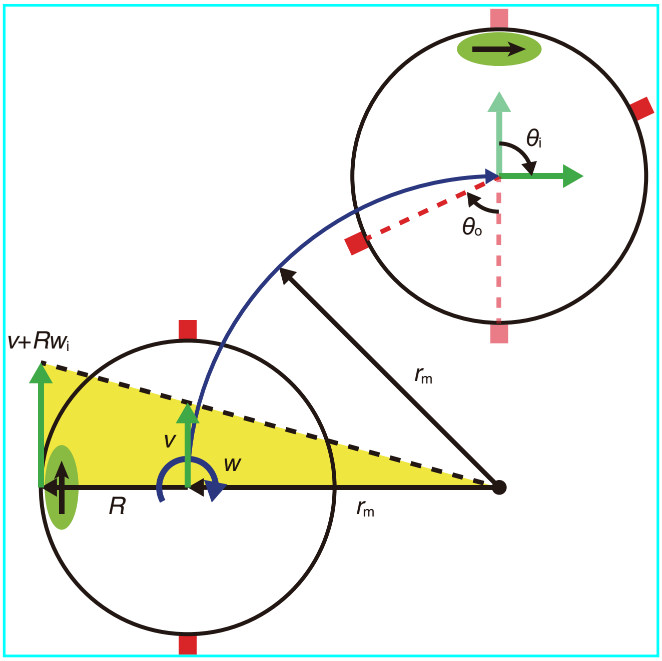

Figure 3.3: Schematic showing the motion of particle structure with constant rate of rotation and translation. During time t, the internal particles and boundary rotate by θ_i and θ_o, respectively, and the structure moves by vt around a radius of r_m.

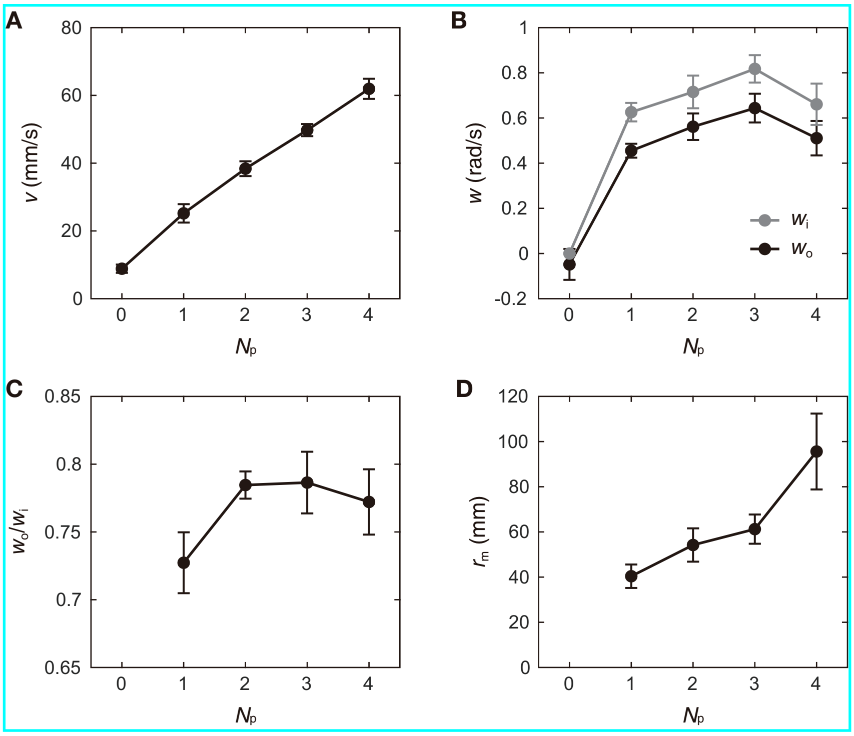

Figure 3.4: Dynamic properties of the structures versus number of SPPs N_{p} for the structure containing the total particles with $N_{\mathrm{t}} = 22$ (packing fraction $\eta = 0.73$). **A**, Translational speed v. **B**, Rotational velocity of the outer boundary w_{o} and inner particles moving along the boundary w_{i} with respect to the boundary center. **C**, The ratio of inner and outer rotational velocity $w_{\mathrm{o}}/w_{\mathrm{i}}$. **D**, Mean radius of the structure motion r_{m}.

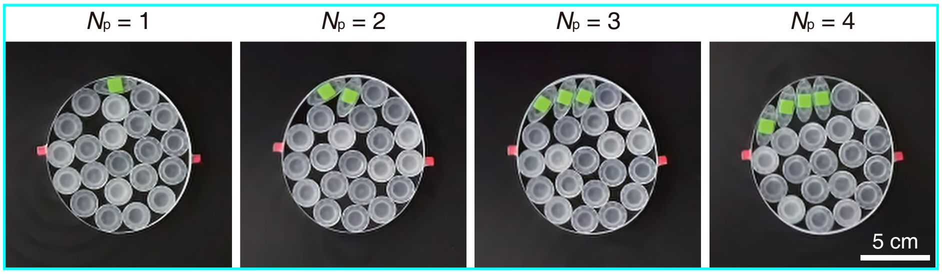

Figure 3.5: Snapshots of dense particle structures moving with different numbers of SPPs.

change in the direction of movement, $r_\mathrm{m}=\int vdt/\int d\theta$, where $d\theta$ is the angle of change of direction during dt. The radius increases with N_p, and it rises dramatically by the fourth SPP (Fig. 3.4D). The primary reason for this dramatic rise is that v increases more rapidly than w_i with N_p (Fig. 3.4A and 3.4B). Also, the decrease in w_i at $N_\mathrm{p} = 4$ (Fig. 3.4B) induces rapid rise in r_m (Fig. 3.4D), suggesting that the structure's polarity increases rapidly when N_p exceeds a critical number.

These changes in polarity and interaction are the results of the different ordering of the SPPs depending on N_p, which is shown in Fig. 3.5. When the structure contains a single SPP, the particle moves along the boundary in a tangential direction to the boundary. On the other hand, for $N_\mathrm{p} \geq 2$, physical interference between particles makes the preceding SPPs to be erected in a direction perpendicular to the boundary. The propensity for the structures to move straight increases as the SPPs align perpendicular to the boundary, implying that the polarity increases with N_p. In addition, the increased normal force on the boundary, which is the origin of interaction between the particles and the boundary, makes the two rotational velocities, w_i and w_o, to be similar. Fig. 3.6 shows the process in which the SPP at the front rotates when $N_\mathrm{p} = 5$ so that the structure undergoes pure translational motion. The increase in SPP population reduces movement speed and changes SPP arrangement along the boundary, making it easier for the front SPP to change directions. This direction change leads the

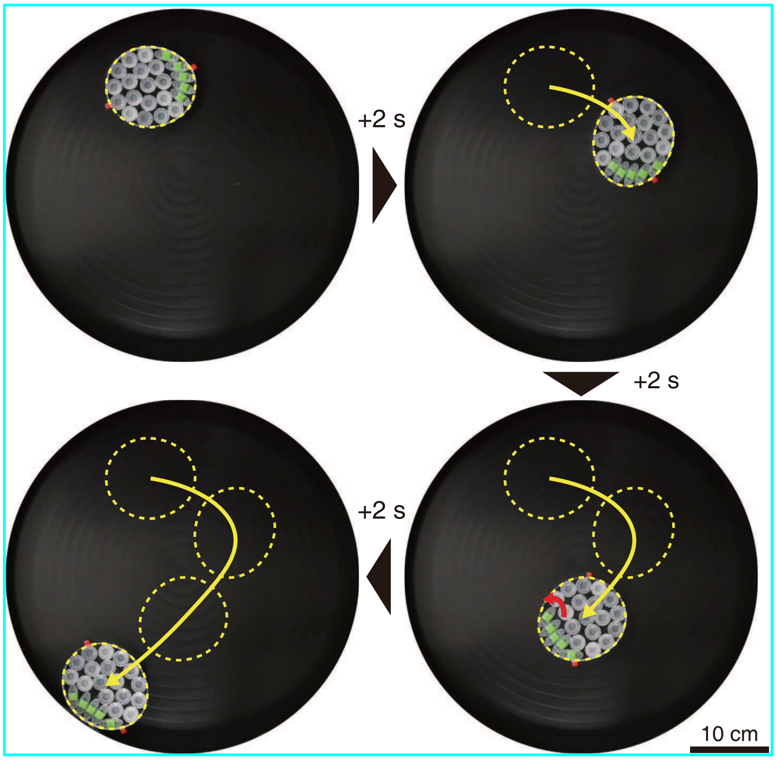

Figure 3.6: The transition of a dense particle structure containing five SPPs from circular motion to straight motion. The structure, which initially moved with chirality, moves straight to the arena boundary after the leading SPP rotates.

SPPs to become stuck at the boundary, which is similar to the SPP cluster of eight or more particles in §2.5 of chapter 2. This behavior shows that the structure increases in polarity with N_p, but losses chirality and has pure polarity without orientation change above a critical N_p.

The polarity and chirality of the particle structure allows for different behavior of the structure in a dense environment. If the structure is composed of a mobile boundary with short arms, the rotation of the structure may well exert a rotational force on the surrounding particles. We see that the densely packed particles move to some extent by a centrally

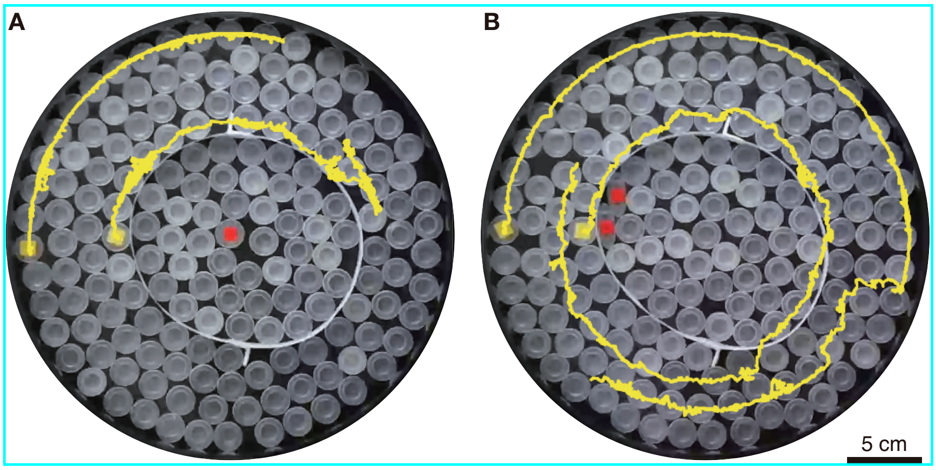

Figure 3.7: Trajectories of two nonpolar particles in a dense environment outside the dense particle structure. In order to affect the neighboring particles, we attached a thin plastic structure, 15 mm long, to both sides of outer boundary of 155 mm in diameter. The positions of the two nonpolar particle (marked in yellow) are tracked for 4 minutes. Compared to a structure (**A**) containing a signle circular SPP (marked in red), a structure (**B**) containing two SPPs with an AR of 2.5 displaces neighboring particles more.

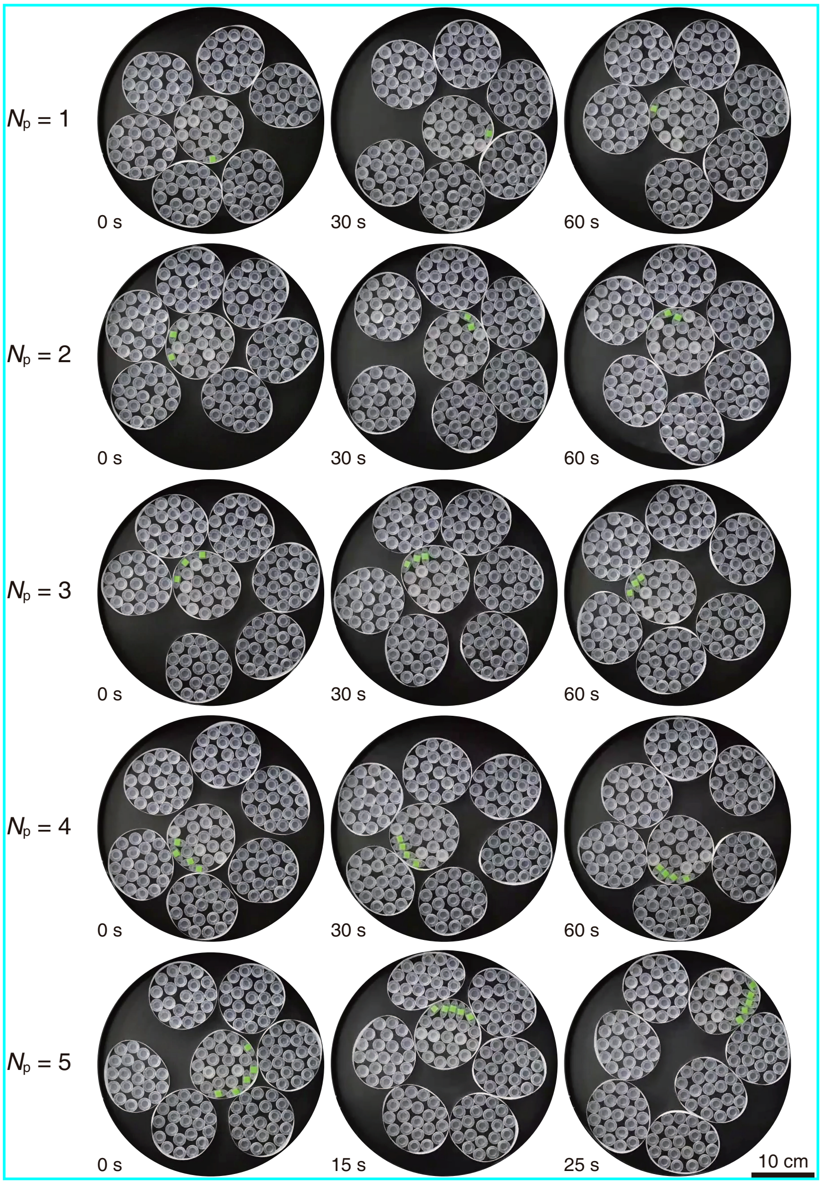

Figure 3.8: Behaviors of dense particle structures with different N_p when surrounded by randomly vibrated structures containing only nonpolar particles. For $N_\mathrm{p} \leq 4$, the structures stay inside the surrounding structures. The structure containing five SPPs moves to the arena boundary by opening the gap between the surrounding structures and pushing them away.

placed structure containing a single SPP with an AR of 1 (Fig. 3.7A). As expected, in a dense environment, it is difficult to create large movements of surrounding particles with only the vertical momentum caused by polarity. On the other hand, the surronding particles are displaced much more than in Fig. 3.8A by the structure containing two SPPs with an AR of 2.5 rotating along the structure boundary (Fig. 3.7B). The combination of high angular momentum and strong normal force by multiple SPPs moving along the boundary facilitate the rotational motion around the structure in a dense environment. Unlike chirality, which creates rotational motion, the high polarity of the structures makes it easy for them to squeeze through narrow gaps as a single SPP move in a dense environment. We consider a situation where a structure containing SPPs is surrounded by structures that are composed entirely of nonpolar particles and thus exhibit directionless motion. In contrast to structures with $N_\mathrm{p} \leq 4$ that are continuously rotating and trapped inside the surrounding structures, the structure with five SPPs lose its chirality due to the rotation of the leading SPP and eventually squeeze through the gap between the surrounding structures (Fig. 3.8). These two behaviors show the potential for the dense particle structure to perform different functions in dense environments.

3.4 Particle packing density effect

Decreasing the particle packing density in the mobile boundary can change the way the particles are arranged, which can alter the dynamic properties of the particle structures. Fig. 3.9A shows the structure in motion when the particles are densely packed. The SPPs move along the boundary with the leading particle being obstructed by the two nonpolar particles in front (blue and magenta) as observed in previous chapter. In Fig. 3.9B, the structure moves with one less nonpolar particle than in Fig. 3.9A. Here, unlike blue particle at the boundary, magenta particle hardly pushes the leading SPP due to the empty space by low packing density, allowing the SPPs to align close to the normal direction to the bound-

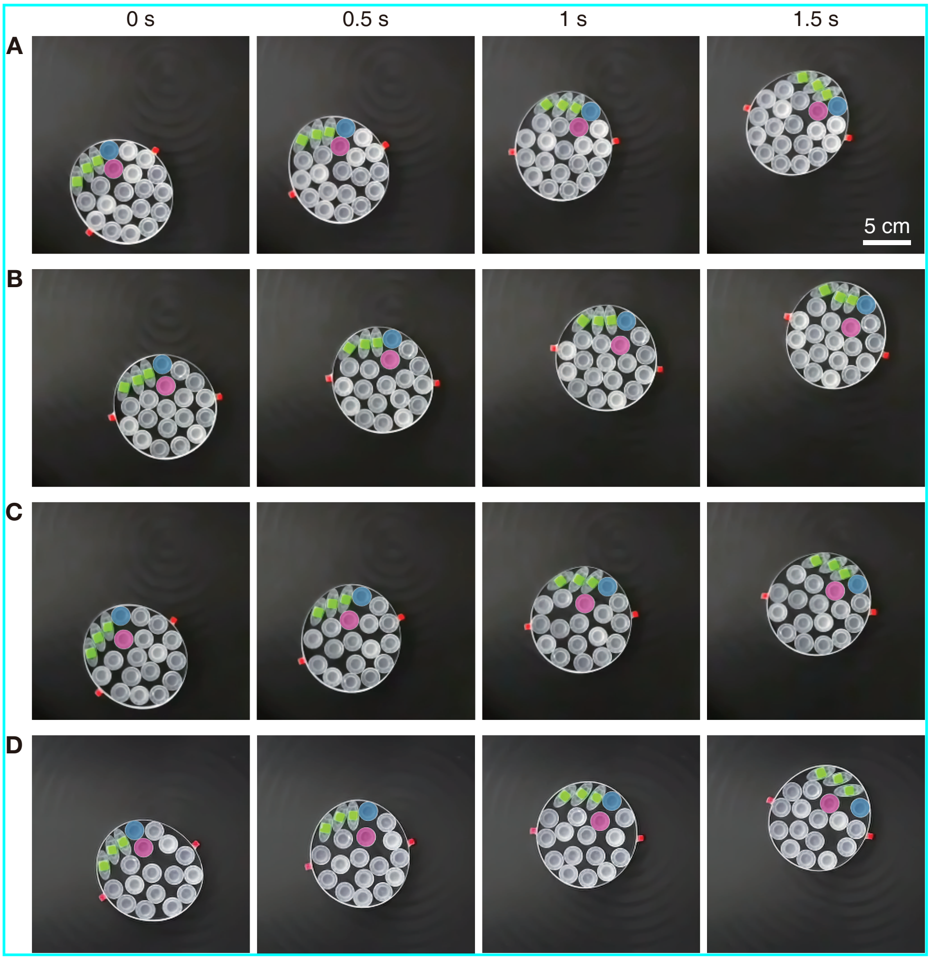

Figure 3.9: Changes in particle distribution and arrangement by reducing particle packing density. Snapshots of particle structure containing three SPPs with (**A**) 22, (**B**) 21, (**C**) 20, and (**D**) 19 total particles.

ary. This alignment causes the SPPs to poorly move along the boundary and exerts a strong force perpendicular to the wall. If the number of nonpolar particles is reduced more than in Fig. 3.9B, the density around the boundary also decreases (Fig. 3.9C and 3.9D). In these cases, neither magenta nor blue particles exert much force on the leading SPP. Therefore, unlike in Fig. 3.9C, the SPPs are again tilted in a direction tangent to the boundary, similar to the particles in Fig. 3.9A. SPPs eventually move well along the boundary at low packing density, and both the tilted alignment and reduced η itself cause the SPPs to press more weakly against the boundary.

To quantify the effects of packing density reduction, we measure the dynamic properties of the particle structure by varying η and N_p. The translational speeds are shown in Fig. 3.10A where the speeds are not significantly affected by η. This independence is because the nonpolar particles are able to follow the structure motion through their directionless mobility, so that the number of nonpolar particles does not impose much resistance to the structure motion. On the contrary, the inner rotational velocities w_i obviously vary with η (Fig. 3.10B). When $N_\mathrm{p} = 1$, the single SPP moves tangentially to the boundary regardless of the packing density. Therefore, the decrease in particle resistance as a result of a decrease in η causes the SPP to move faster, eventually leading to a rise in w_i. Unlike $N_\mathrm{p} = 1$ and 2, when $N_\mathrm{p} = 3$, w_i becomes minimum around $\eta = 0.7$ ($N_\mathrm{t} = 21$) because the SPPs are aligned most perpendicular to the boundary at $N_\mathrm{t} = 21$ as mentioned above in Fig. 3.10B. Fig. 3.10C shows that $w_\mathrm{o}/w_\mathrm{i}$ decreases as η decreases, and the effect is stronger when the structure contains fewer SPPs. This reduction is a result of the low internal pressure caused by low packing density, which leads to less interaction between the particles and the boundary. Also, as shown in Fig. 3.5, the SPPs are less likely to be oriented perpendicular to the boundary as the N_p goes down, making the interaction more dependent on the internal pressure. The change in the alignment and behavior of SPPs due to the reduced packing density eventually alters the radius of motion (Fig. 3.10D). In general, a rise in chirality

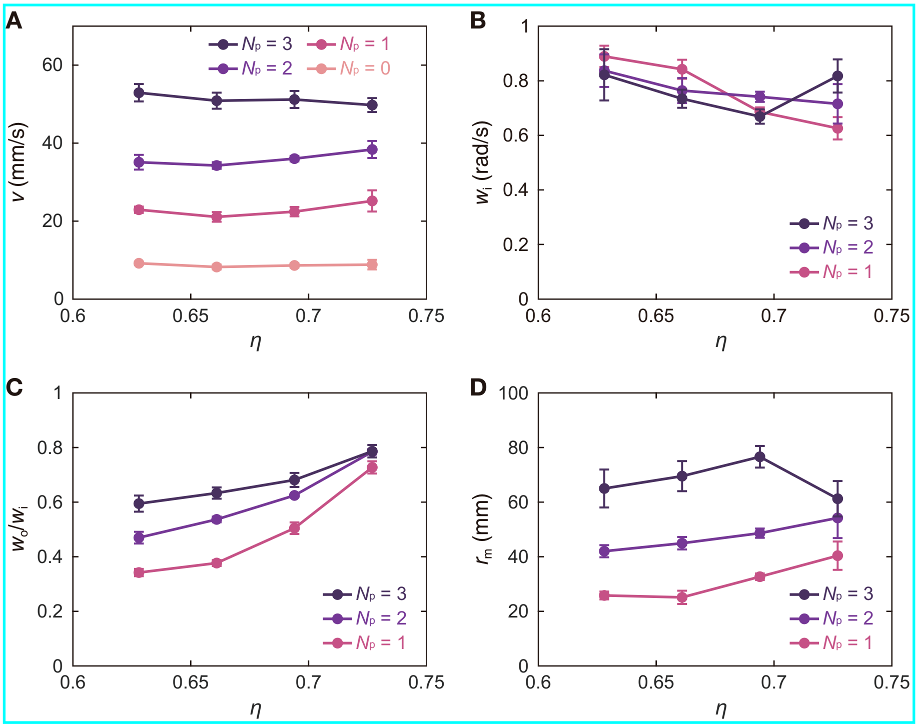

Figure 3.10: Dynamic properties of the structures versus particle packing fraction η for different N_p. **A**, Translational speed v. **B**, Rotational velocity of the inner particles moving along the boundary w_i with respect to the boundary center. **C**, The ratio of inner and outer rotational velocity $w_\mathrm{o}/w_\mathrm{i}$. **D**, Mean radius of the structure motion r_m.

due to a decrease in η (Fig. 3.10B) causes r_m to decreases, but when $N_\mathrm{p} = 3$, the radius reaches its maximum at $N_\mathrm{t} = 21$ where the chirality is at its lowest (Fig. 3.9B and 3.10B).

3.5 Boundary properties effect

In addition to the particle packing density, the mechanical properties of the boundary can also affect the behavior of dense particle structure. The mass and flexibility of the boundary affect the structure mobility and the inner particles distribution, respectively. To avoid altering the surface properties inside the boundary, we fabricate new boundaries by increasing the height from the original boundary (a, 0.64 g) to add mass while keeping the stiffness low (b, 1.54 g), and by attaching a stiff frame outside the boundary to increase both mass and stiffness (c, 1.54g), as shown in Fig. 3.11A. Then we compare the stiffness of each boundary by measuring the force when pressing the boundaries as shown in the schematic in Fig. 3.11B. At a displacement less than 15 mm, the stiffness of boundary b and boundary c is measured to be within 3 times and over 30 times that of original boundary, respectively (Fig. 3.11B and inset of Fig. 3.11B). A low stiffness makes it easier for SPPs to deform the boundary, which makes them more likely to get stuck in large curvatures and consequently reduces their mobility along the boundary.

We plot in Fig. 3.12 the dynamic properties of the particle structure measured experimentally. As expected, the translational speed v decreases with mass without stiffness effect, $v_\mathrm{a} > v_\mathrm{b} \approx v_\mathrm{c}$ (Fig. 3.12A). For rotational motion, Fig. 3.12B shows $w_{\mathrm{i,a}} > w_{\mathrm{i,b}} \approx w_{\mathrm{i,c}}$ when $N_\mathrm{p} = 1$ and 2, demonstrating the effect of high moment of inertia due to increased mass of the boundary. But we can see $w_{\mathrm{i,a}} \approx w_{\mathrm{i,b}} \approx w_{\mathrm{i,c}}$ when $N_\mathrm{p} = 3$, and the relationship is reversed to $w_{\mathrm{i,a}} < w_{\mathrm{i,b}} < w_{\mathrm{i,c}}$ when $N_\mathrm{p} = 4$. This result occurs because the boundary's degree of deformation changes with N_p. When N_p is small, the weak propulsion force cannot deform the boundary, which makes w_i only affected by mass, similar to v. When N_p is large, on the

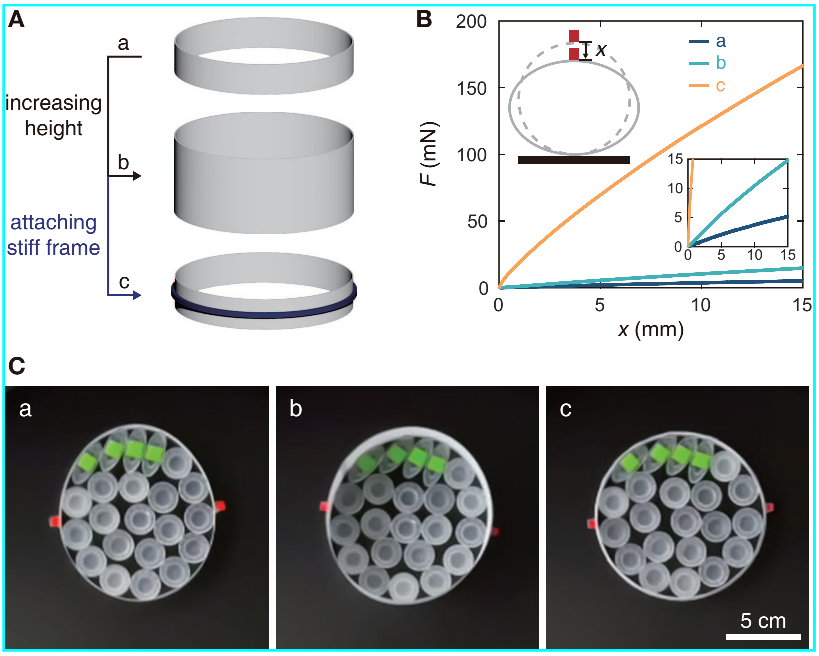

Figure 3.11: Three types of boundaries with different mass and stiffness. **A**, Thin, light (a, 0.64 g), thin, heavy (b, 1.54 g), and thick, heavy (c, 1.54 g) boundary. **B**, Force-displacement curves of each boundary. **C**, The deformation of each boundary under the condition that $N_\mathrm{t} = 22$ ($\eta = 0.73$) and $N_\mathrm{p} = 4$. The initially circular boundaries are deformed to aspect ratio of (a) 1.13, (b) 1.07, and (c) 1, respectively.

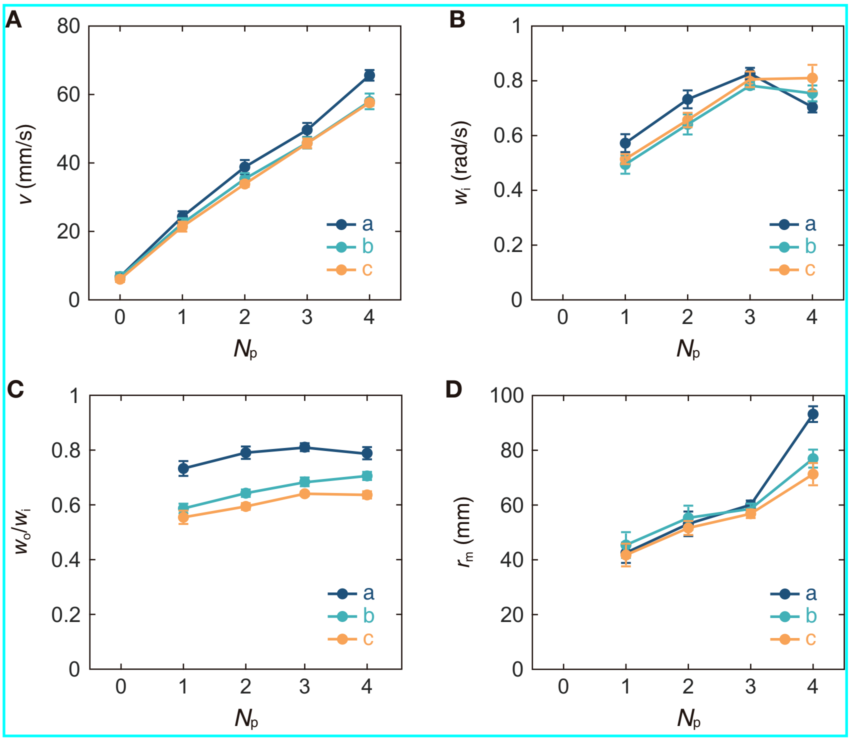

Figure 3.12: Dynamic properties of the structures versus number of SPP N_{p} for different boundaries. **A**, Translational speed v. **B**, Rotational velocity of the inner particles moving along the boundary w_{i} with respect to the boundary center. **C**, The ratio of inner and outer rotational velocity $w_{\mathrm{o}}/w_{\mathrm{i}}$. **D**, Mean radius of the structure motion r_{m}.

contrary, a significant force can deform the non-stiff boundary. This deformation makes the SPPs susceptible to being trapped in large curvature and thereby reduces their mobility along the boundary, which makes w_i decrease with the stiffness. The change in $w_\mathrm{o}/w_\mathrm{i}$, shown in Fig. 3.12C, also demonstrates the stiffness effect. Essentially, the increase in the boundary's moment of inertia inhibits its rotation, which makes $w_\mathrm{o}/w_\mathrm{i}$ smaller. At this point, the trap effect through deformation at low stiffness increases the interaction between polar particles and the boundary, thereby making $w_\mathrm{o}/w_\mathrm{i}$ slightly larger in boundary b than in boundary c. Also, the closest approach of the $w_\mathrm{o}/w_\mathrm{i}$ in boundary b to that in boundary a when $N_\mathrm{p} = 4$ reaffirms that the trap effect increases with N_p. Fig. 3.12D shows that each r_m is similar when $N_\mathrm{p} \leq 3$ because the effects of inertia and stiffness on v and w_i cancel out. However, the rapid change of w_i due to the large trap effect when $N_\mathrm{p} = 4$ eliminates the canceling effect so far, causing the r_m of original boundary is much larger than those of boundary b and c.

3.6 Conclusions

In this chapter, we have presented an analysis of alterations in structural behavior resulting from modifications in the components of a dense particle structure. Because particles are not free to move in dense environments, imparting switchable behavior to our structure is highly different from the behavioral mechanism proposed in previous studies for structures confining low nomber density particles or unconfined robotic swarm systems. We used the results on the behavior of a small number of SPPs in a dense environment introduced in chapter 2 to show the different behavior of dense structures. We proposed the redistribution of vibrated particle clusters as a mechanism for modulating the motion of the densely organized structures. By conducting experiments with a single SPP, we first found that the behavior of the structure differs when the SPP stays in the bulk of the dense granular medium and when it moves at the boundary. Then we confirmed that the mechanical properties and the amount of SPPs allow for the confined, dense structure to exhibit diverse behaviors ranging from random, rotational to directional motion. Next, by changing particle packing density or boundary properties, we showed that tuning the particle-particle and particle-boundary interaction can additionally adjust the structure behavior. The substantial changes in structure behavior highlight the importance of altering the characteristics and number of individual components, giving a straightforward but effective method for designing and optimizing self-organized structures with reconfigurable behaviors. The finding of our study can help researchers develop dense structures with emergent properties through a bottom-up approach. We also expect that our approach, along with the introduction of highly deformable particles or boundaries, will provide a simple but effective platform for evaluating the mechanical properties of cell behavior.

Chapter 4

Vibrated particle chains with reconfigurable behaviors and functions

In the previous chapter, we have introduced our dense particle structures that can exhibit diverse behavior by changing the charactersistics of self-propelled particles (SPPs) and mobile boundaries confining the particles. In this chapter, we show that particle cluster can organize more flexible and multifunctional structures without using boundaries. Soft active structures possess the ability to alter their shape and motion in order to achieve a variety of target functions. This ability enables them to navigate through narrow gaps, circumvent obstacles, and transport objects. At the microscale, where it is challenging to imbue individual units with sufficient intelligence, collectives are unable to execute such tasks without intricate regulation of an external field. In order to attain diverse behaviors utilizing uncomplicated active particles, it is imperative that the structures be manipulable through scale-free physics. In this study, we present an unbranched, open chain structure composed of SPPs that exhibit continuous translational motion through vertical vibration. The manipulation of design parameters of connecting links enables the regulation of the relative motion of neighboring particles. This alteration of flexible structures facilitates unidirectional or reciprocating motion and enables the particles to exert a propulsive force when encountering an obstacle. Our study provides evidence of the chains' superior functionality as they are capable of executing multiple tasks that may be in opposition to one another, including object passing or enclosing, load advancement or retraction, and narrow space penetration or obstruction. The possibility of reprogramming functions implies that incorporating behavioral constraints among neighboring components could facilitate the design and development of adaptable soft robot systems, at both small and large scales.

4.1 Introduction

Similar to a small organisms that responds to environmental disturbances and performs many functions, self-driving robots that operate at very small sizes could be applied in a range of applications, including medicine (Nelson *et al.*, 2010), manufacturing (Diller & Sitti, 2011), and changing shape (Goldstein *et al.*, 2005). The capacity to modify the morphology of such systems confers upon them the possibility of adapting to intricate microenvironments (Palagi & Fischer, 2018) or conforming to predetermined configurations (Boley *et al.*, 2019). The objective of these robots is to demonstrate a range of intricate and multifaceted behaviors akin to those observed in traditional swarm robots. The utilization of small active particles that convert energy from their surroundings into propulsion presents a promising avenue for actuating micro-robotics, but a significant obstacle lies in effectively directing their movements. The field of macroscale swarm robotics involves the utilization of individual units that are equipped with memory devices, self-regulatory mechanisms, and communication capabilities with one another to achieve a desired formation (Rubenstein *et al.*, 2014) or reach a predetermined destination (Li *et al.*, 2019). However, it is challenging to give colloidal particles these abilities, which makes it uncommon to observe their robust reconfiguration into finite structures for particular behaviors or functions; these particles typically make emergent patterns instead of discrete shapes (Hagan & Baskaran, 2016; Marchetti *et al.*, 2013; Palacci *et al.*, 2013).

Using particle collectives modulated by light (Lavergne *et al.*, 2019; Zhang *et al.*, 2021), acoustics (Aghakhani *et al.*, 2020), magnetic fields (Wang *et al.*, 2022), or other global inputs is one approach to achieve complicated behaviors at the microscale. These externally powered microrobot collectives can move, flock, rotate, and travel through channels (Xie *et al.*, 2019), as well as perform tasks including transporting and turning objects (Gardi *et al.*, 2022). However, each particle is limited to materials that respond to external stimuli like as a magnetic field for these collective behaviors, and each freely moving unit is at risk of being scattered by flow and disturbances in the absence of the stimuli. One new strategy to overcoming these constraints is to manage behavior through physical interactions between system components. One study illustrates directed locomotion of macroscale robot swarm by programming robots to expand and contract out of phase with each other to push and pull nearby robots (Li *et al.*, 2019). Recent work uses active cohesive robots (Li *et al.*, 2021) or confining simple active robots (Boudet *et al.*, 2021; Deblais *et al.*, 2018) in flexible and mobile boundaries for systems that can be used across scales, but neither exhibits the high functionality and adaptability of particle collectives controlled by a sophisticated external force field. Other groups have broadened the scope of active matter by utilizing chains of active particles or active polymers (Eisenstecken *et al.*, 2016; Kaiser *et al.*, 2015; Winkler *et al.*, 2017), similar to active filaments in living organisms (Deblais *et al.*, 2020; Heeremans *et al.*, 2022). Connecting particles in translational (Agrawal & Glotzer, 2020) and rotational (Scholz *et al.*, 2021; Spellings *et al.*, 2015) motion, or robots that operate on the ground (Ozkan-Aydin & Goldman, 2021) or in the air (Kulkarni *et al.*, 2020) allows the chain structures to take on diverse shapes and perform varied roles. While the dynamics of these structures are restricted, they highlight the possibility for adaptable, reconfigurable systems only by adjusting the sequence or configuration of active particles.

In this study, we present a particle chain that is reconfigurable and capable of executing a variety of behaviors and tasks with only simple SPPs. The experimental system is built by assembling a nonloop chain of SPPs driven by vertical vibration and links connecting two neighboring particles. The chain's flexible nature allows it to adapt to its environment by changing its form and the orientation of each particle when it encounters a wall, object, or impediment. The chain is initially composed of particles loosely aligned in the direction of the center particle. To control the behavior, we use morphological control that changes the length of the chain and the relative motion of neighboring particles by the design parameters of the connecting links. The chain's adaptability is evidenced by its capacity to travel along the surface in a variety of ways and perform a variety of functions, including traversing or remaining in obstacles, passing or enclosing objects, moving objects forward or backward, and infiltrating or blocking narrow spaces (Fig. 4.1). The dynamics can be represented qualitatively or quantitatively by studying the orientation of each particle in the chain as it deforms in each environment. Our concept's scalability, material independence, and programmability enable the development of reconfigurable and autonomous systems from simple components at any scale.

4.2 Chain design

To construct a particle chain, we created particles with tilted legs that exhibit directed motion by vertical vibration. As shown in Fig. 4.2, the particles have a cuboid top on a circular head with a diameter of $d = 15$ mm to allow indirect interparticle interaction through connections. We connect N particles with $N-1$ links that have ribbon-shaped slots on both sides and a length L between the centers of two slots. To produce a nonloop chain with no interparticle interference, we fixed the length L = 16 mm, which is slightly longer than the particle diameter. The chain is symmetrical,

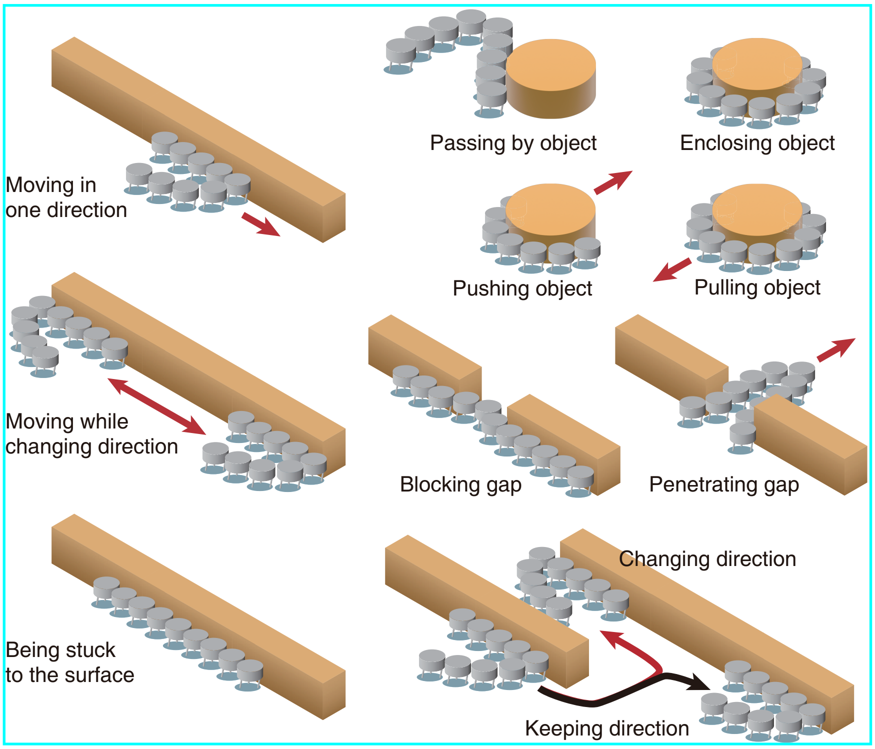

Figure 4.1: Schematic representation of the diverse functions that a particle chain can execute. On the left, the chain exhibits unidirectional or bidirectional motion along a surface, or alternatively, it adheres statically to the surface without any motion. In the upper right, the chain passes through or encloses an object, and pushes or pulls an object. In the lower right, the chain obstructs or traverses a constricted aperture, and alters its trajectory upon encountering modified topography.

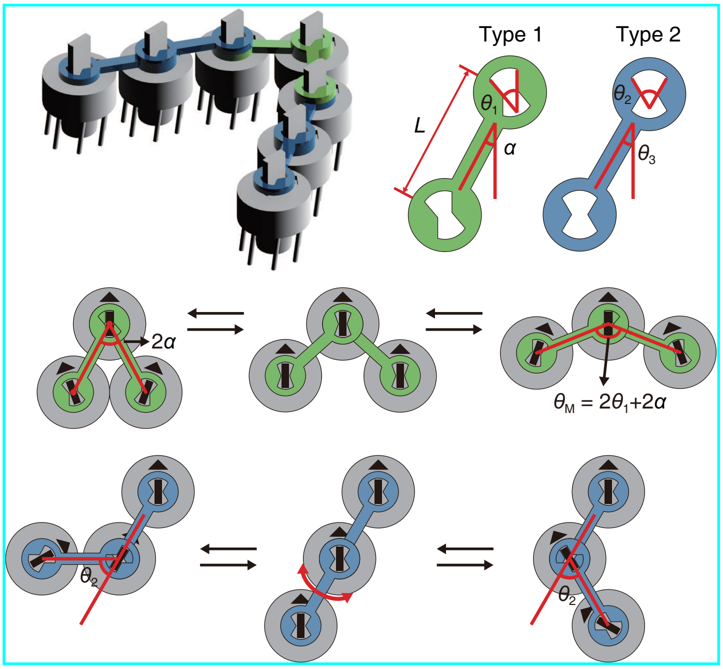

Figure 4.2: Chain design with controllable shape. A nonloop chain of seven particles symmetrically connected by two types of links which have ribbon-shaped slots on each side. These slots allow particles and linkes to rotate in a limited range.

with links on one side reversed from links on the other in regard to the center particle. This symmetry prevents undesirable, random deformations, such as crumpling and curling, that are common in many active filaments (Winkler *et al.*, 2017).

We designed two types of links to manage the chain's behavior and deformation. The center particle and two particles on each side are connected by type 1 (green) links that can be rotated within θ_1. When fully unfolded, this link permits the chain's center to be up to $2\theta_1$ degrees distant from the angle $2\alpha = 2\arcsin(d/2L)$. The remaining particles are connected together by type 2 (blue) links, which have a degree of rotational freedom θ_2 and a tilt angle θ_3 that sets the initial position of any two neighboring particles.

The angle θ_2 limits the rotation range of the particles and links, and the angle θ_3 controls how far the chain expands to either side. Here, restriction of rotation ranges by θ_1 and θ_2 assures that all particles are loosely aligned in the orientation of the center particle. These links offer the chain the behavior directionality as well as the structural flexibility it requires to fold or unfold around its center, and each angle that limits the chain's range of motion gives it programmability.

4.3 Dynamics of chains on walls

4.3.1 Behavior at the boundary

We begin with the chain contacting a wall to obtain insight into how the design of the links related to the behavior of the chain. We first orient the particles in one direction so that the chain travels to the arena boundary of diameter $30d$. The behavior of a chain of seven particles connected by links with $\theta_1 = 180^\circ$ and $\theta_2 = 180^\circ$, where each particle and link can freely rotate, is depicted in Fig. 4.3A. When the chain reaches the boundary, it moves by falling away and reattaching the boundary as its shape randomly deforms. On the other hand, a chain whose particles travel closer to the orientation of the center particle continues to move along the boundary while maintaining a constrained shape (Fig. 4.3B). The alignment effect and symmetrical structure keep the chain from deviating from the boundary.

The movement along the surface of chains with an alignment effect and a symmetrical structure exhibits three distinct behaviors, as schematically shown in Fig. 4.4A: traveling in one direction (i), changing direction while moving (ii, see 4.3B, $4.5 < t < 7$ s), becoming stuck while pushing the surface (iii). The behavior of the chain is determined by how the particles move together, which is altered by the design of the links. With $\theta_2 = 60^\circ$ fixed, we see that the chain goes unidirectionally when θ_1 is small ($\theta_1 < 30^\circ$), pushes the boundary when θ_1 and θ_3 are large together ($\theta_1 \geq 50^\circ$ and $\theta_3 \geq 30^\circ$), or θ_3 is very large ($\theta_3 \geq 45^\circ$), and moves bidirectionally in

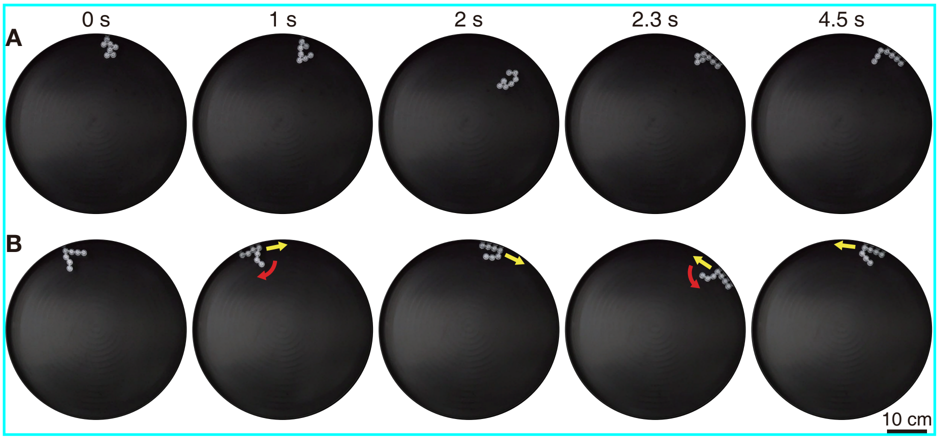

Figure 4.3: Effects of restricting rotation range by links on chain behavior at arena boundary. Seven SPPs are connected by links with (**A**) $\theta_1 = 180^\circ$, $\theta_2 = 180^\circ$, and links with (**B**) $\theta_1 = 40^\circ$, $\theta_2 = 60^\circ$, and $\theta_3 = 30^\circ$. To reach the boundary, each particle in the chain is initially aligned in the orientation of the center particle.

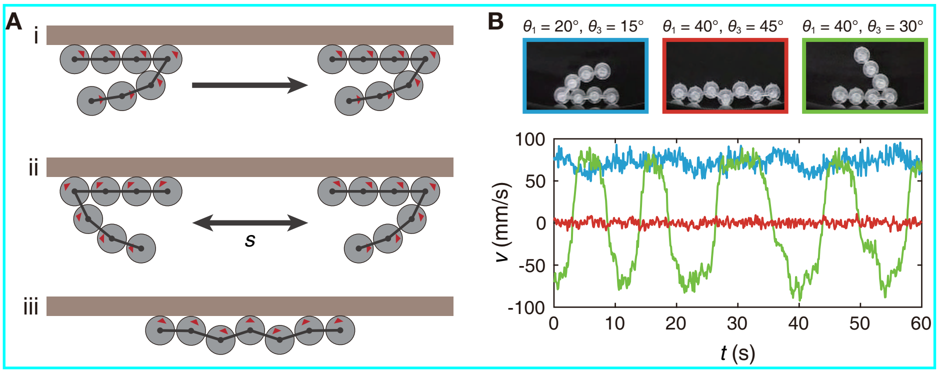

Figure 4.4: Different chain behaviors at arena boundary. **A**, Schematic showing three different behavior modes at a wall: (i) moving in one direction, (ii) moving back and forth at intervals of s, (iii) pushing a wall without moving. **B**, Velocity changes with time and chain snapshots for the three modes.

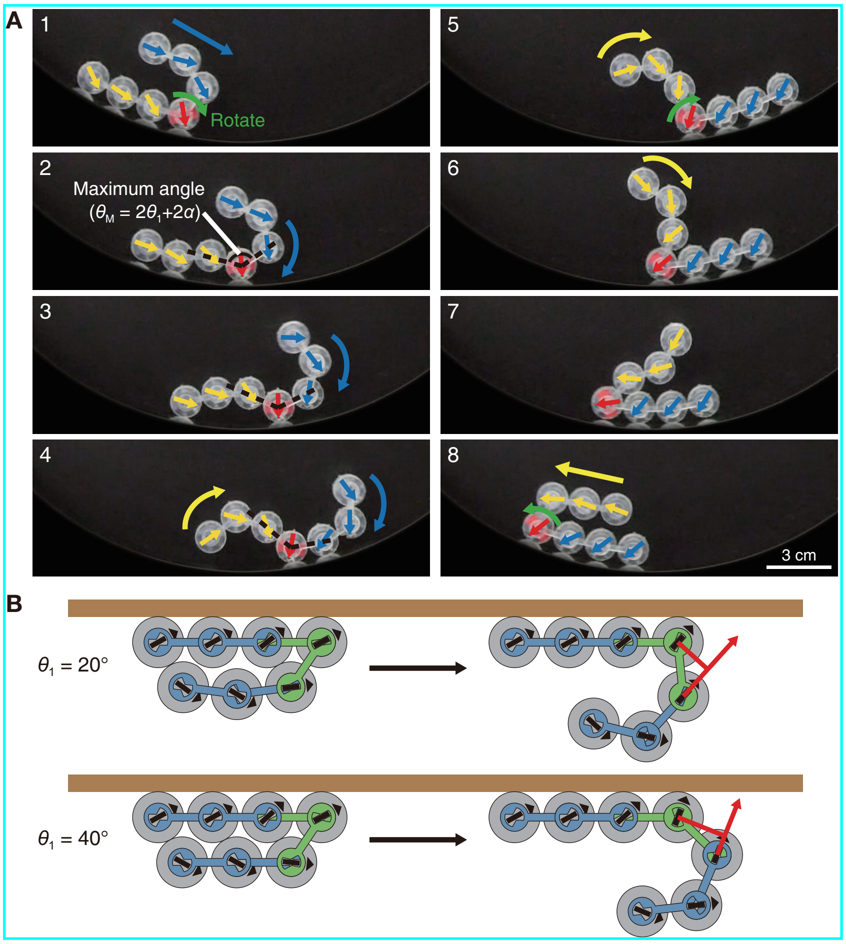

Figure 4.5: The mechanism by which a chain changes direction at arena boundary. **A**, The process by which the chain changes direction. The momentum of the particles on the other side of the boundary increases the angle between the two links at the center, which pulls the other particles away from the boundary and finally rotates the chain. The arrows marked on the particles indicate the orientation of each particle. **B**, Schematic showing the orientation of each particle when one side of the chain is attached to the wall and the other side is maximally extended outward.

all other conditions. These disparities result from the greater difficulty of reversing direction when the chain is easier to fold (low θ_1) and the greater likelihood of the chain to line up parallel to the surface when the chain is likely to extend out (high θ_1 and θ_3). Fig. 4.4B depicts an example of the time-varying velocity of the center particle for each behavior; in each condition, the chain moves with the velocity reversing at regular intervals, stays above a particular velocity with minimal variations, or has an almost zero velocity. The cyclic reorientation occurs as follows: (i) the movement of the particles on the opposite side of the boundary causes the center of the chain to unfold at a maximum angle, (ii) the torque exerted by the sustained movement rotates the center particle, and (iii) the remaining particles fall off the boundary, forcing the chain to mnove in reverse (Fig. 4.5A). We do not see this reorientation at low θ_1 because the narrow spreading exerts little torque on the center particle (Fig. 4.5B). We note that the three modes of behavior remain the same as the chain gets longer, with the exception that the chain is more likely to exit the static state when it is longer due to higher noise (Fig. 4.6).

As just mentioned, increasing θ_1 makes reorienting the chain easier, which reduces the root-mean-square velocity, v_{rms}, or makes it immobile (Fig. 4.7A). To further investigate the dynamics of bidirectional motion quantitatively, we measured v_{rms} and the distance traveled in half a cycle s with $\theta_1 = 40^\circ$. Fig. 4.7B shows that chains with a small θ_3 move by changing direction throughout a wide range of θ_2, whereas chains with a $\theta_3 = 30^\circ$ do not move when θ_2 is either too small ($\theta_2 = 30^\circ$) or too large ($\theta_2 = 120^\circ$). This means that the chain exhibits bidirectional motion when it has appropriate interparticle interactions and structure flexibility, which occurs when the particles have a moderate rotational degree of freedom. Under conditions that ensure each particle's intermediate rotation ($45^\circ \leq \theta_2 \leq 75^\circ$), the chain continues to move as θ_3 increases, and then switches to pushing the boundary when θ_3 surpasses a threshold value for each θ_2 (Fig. 4.7C). For the distance traveled in the subthreshold situation, s increases with θ_3 at a slower rate as θ_2 increases, and it appears to be capable of reaching

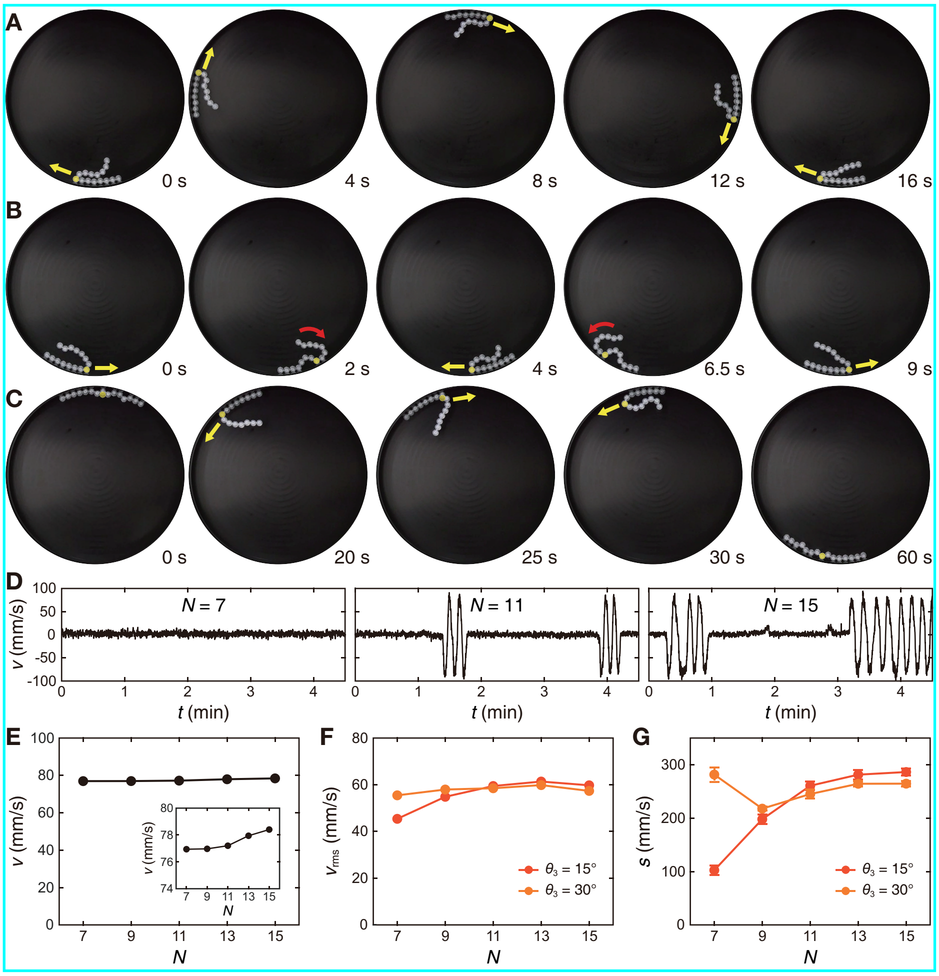

Figure 4.6: Behaviors of longer chains at arena boundary. **A**, A chain with $\theta_1 = 20^\circ$, $\theta_3 = 15^\circ$ unidirectionally moves along the boundary. **B**, A chain with $\theta_1 = 40^\circ$, $\theta_3 = 30^\circ$ moves while changing direction. **C**, A chain with $\theta_1 = 40^\circ$, $\theta_3 = 45^\circ$ switches between pushing the boundary and moving along the boundary. In **A** to **C**, N is 15 and the yellow circles in each chain indicate the center particle. **D**, Velocity over time at the boundary of three chains with different N with same links as (**C**). **E**, Average speed of chains with different N with same links as (**A**) The relation of (**F**) $v_{\rm rms}$ and (**G**) s to N with same links as (**B**). The angle θ_2 is 60° for all experiments.

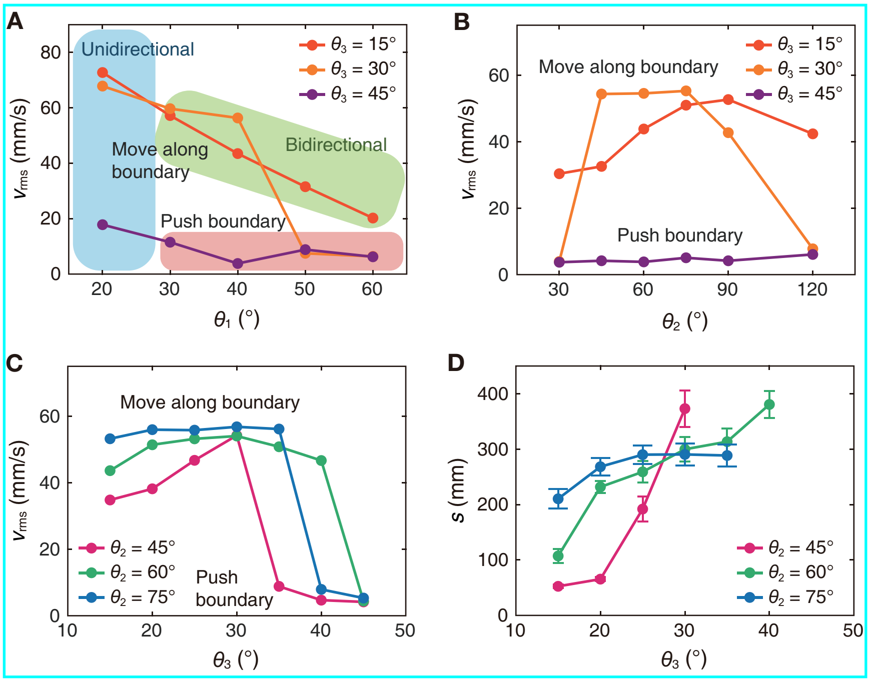

Figure 4.7: Dynamics of particle chains at arena boundary. **A**, Root-mean-square velocity, v_{rms}, of chains with different θ_1 and θ_3 when θ_2 is fixed to 60°. **B**, The relationship between v_{rms} and θ_2 when θ_1 is fixed to 40°. The relationship of (**C**) v_{rms} and (**D**) average distance traveled in half a cycle s to θ_3 when θ_1 is fixed to 40°.

a maximum of more than 25 times the particle diameter when the radius of boundary curvature is 225 mm (Fig. 4.7D). Finally, we see that v_{rms} and s change with N, whereas the effect of θ_3 decreases as the chain gets longer (Fig. 4.6F and 4.6G). With these observations and measurements, we can move on to our next investigation, which will look at how the chain travels when it comes into touch with various obstacles or objects. We now proceed further experiments by fixing $\theta_2 = 60^\circ$, which provides the chain with appropriate flexibility and interparticle interaction throughout a large range of θ_3.

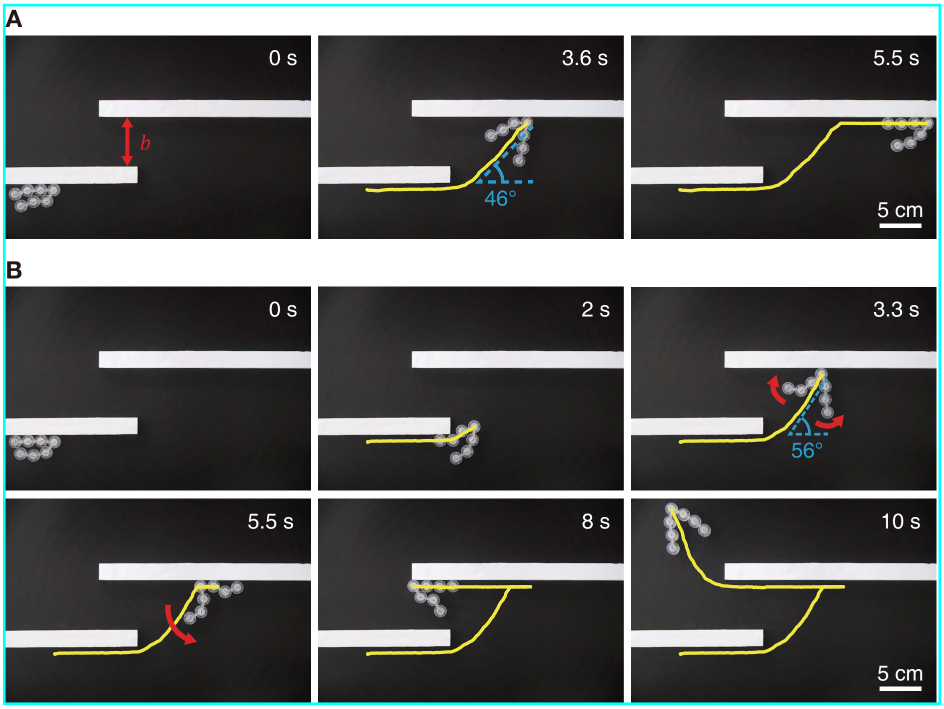

Figure 4.8: The trajectory of a chain of $N = 7$ connected by type 1 links with $\theta_1 = 20^\circ$ and type 2 links with $\theta_3 = 15^\circ$ (**A**) or 30° (**B**) when it reaches the end of a wall and encounters another parallel wall with a gap $b = 4d$ from the original wall.

4.3.2 Behavior when encountering obstacles

Given that the design of the links influences how the chain moves along the surface, the chain can exhibit a variety of significant behaviors when confronted with diverse obstacles. We first examined how the chains move when one wall ends and there is a parallel wall next to it by a certain distance. Due to their nature of applying normal force to the surface, chains travelling in a single direction along the surface ($\theta_1 = 20^\circ$) will turn toward the next wall when they reach the end of the original wall. The chain with $\theta_3 = 15^\circ$ remains in its original route after colliding with the new wall (Fig. 4.8A), but the chain with $\theta_3 = 30^\circ$ switches directions

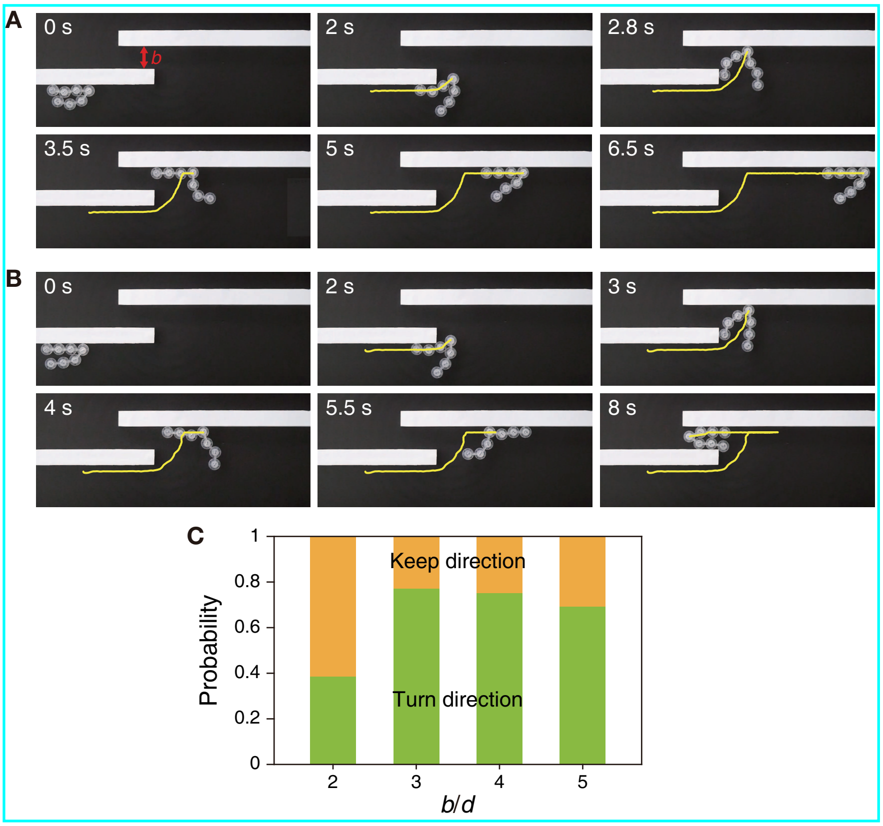

Figure 4.9: Stochastic reorientation of chains in an environment with two parallel walls. When a chain with $\theta_1 = 20^\circ$, $\theta_3 = 30^\circ$ reaches the end of a wall and encounters another parallel wall with $b = 2d$, it moves (**A**) while maintaining its direction or (**B**) reversing its direction. **C**, Probability of a chain with $\theta_1 = 20^\circ$, $\theta_3 = 30^\circ$ changing direction at each interval between two walls.

(Fig. 4.8B). Unlike the chain with low θ_3, which turns at a low angle and forms a narrow structure after leaving the original wall (Fig. 4.8A, $t = 3.6$ s), the chain with higher θ_3 moves more perpendicular to the new wall and has a wider structure (Fig. 4.8B, $t = 3.3$ s), making it easier to change direction after encountering the wall. We note that the direction change for the same chain can be probabilistic because the chain's movement and shape have some degree of freedom due to the slots with θ_1 and θ_2 (Fig. 4.9A and 4.9B). Experiments with varying the distance between the two walls b show that direction change of chains with $\theta_3 = 30^{\circ}$ occurs infrequently ($\sim 40\%$) in narrow gaps ($b/d = 2$) due to the obstruction of the original wall, whereas chains change direction with a higher probability of close to 80% in wider gaps ($b/d \geq 3$) as shown in Fig. 4.9C.

We then created a scenario with a short wall in front of a gap between two independent walls. If a chain with bidirectional motion along the surface moves toward the short wall, it can cross through the obstacle by colliding with the wall in front, going over the wall behind, changing direction at the wall, and then passing through the gap (Fig. 4.10). This passage is only conceivable if the length of the front wall is less than s, the range over which the chain travels periodically; the chain is unable to exit the wall if the length of the front wall exceeds s. The results in both cases illustrate that, depending on the chain design, it is possible for chain to move across diverse obstacles or to move away from it.

4.4 Chains encountering mobile objects

The chain then exhibits a variety of behaviors when directed towards a movable circular object with diameter D. To ensure that the chain has adequate contact with the object, we utilize type 1 links with $\theta_1 = 90^{\circ}$; chains with low θ_1 are more prone to move away from the object after contact due to their weakly unfolded center. We observed five distinct behaviors: essentially static state with the object, carrying the object forward (Fig. 4.11A) or backward (Fig. 4.11B), and moving away from the object

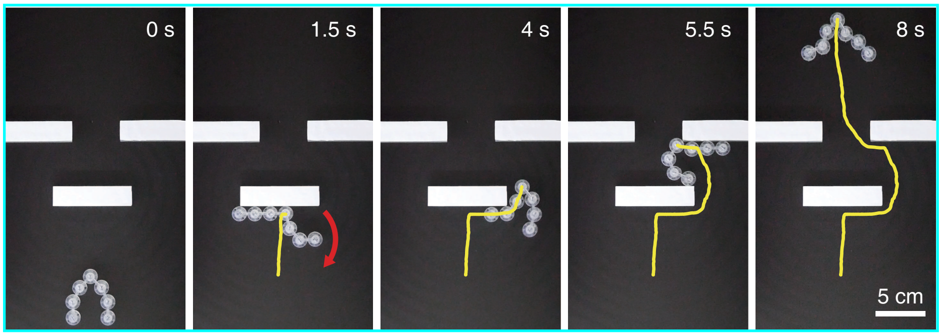

Figure 4.10: The trajectory of a chain of seven particles with with $\theta_1 = 40^\circ$ and $\theta_3 = 30^\circ$ when it encounters a short wall ahead by an interval of $3d$ than a gap between two separate walls.

forward (Fig. 4.11C) or backward (Fig. 4.11D). In this context, ‘forward’ denotes movement in the direction of the center particle’s orientation (red arrows in Fig. 4.11A to 4.11D), whereas ’backward’ denotes the opposite. Which of the five behaviors occurs is governed by the size of the object, the length of the chain, and the degree of spread of the chain that is determined by θ_3. Fig. 4.12 depicts regime maps of chain behavior for three θ_3, 75°, 60°, and 45°. In all three cases, the chains transport the object forward in the upper left area (shorter chain and larger object), and the green regime expands as θ_3 increases. However, when we move to the right area (longer chain), the chains are more likely to move away from the object, and the blue regime becomes wider as θ_3 decreases. Only chains with a large θ_3 appear to carry the object backward in the lower right area. In all panels, bicolored circles reflect the conditions under which the two behaviors can occur. Chains that collide with an object at a little angle are difficult to unfold symmetrically under these conditions, increasing the likelihood that the chain will move away from the object.

To quantitatively understand why each regime appears, we examined the orientation of each particle when the chain comes into conformal contact with the object, as illustrated in Fig. 4.13A. Through geometric analysis,

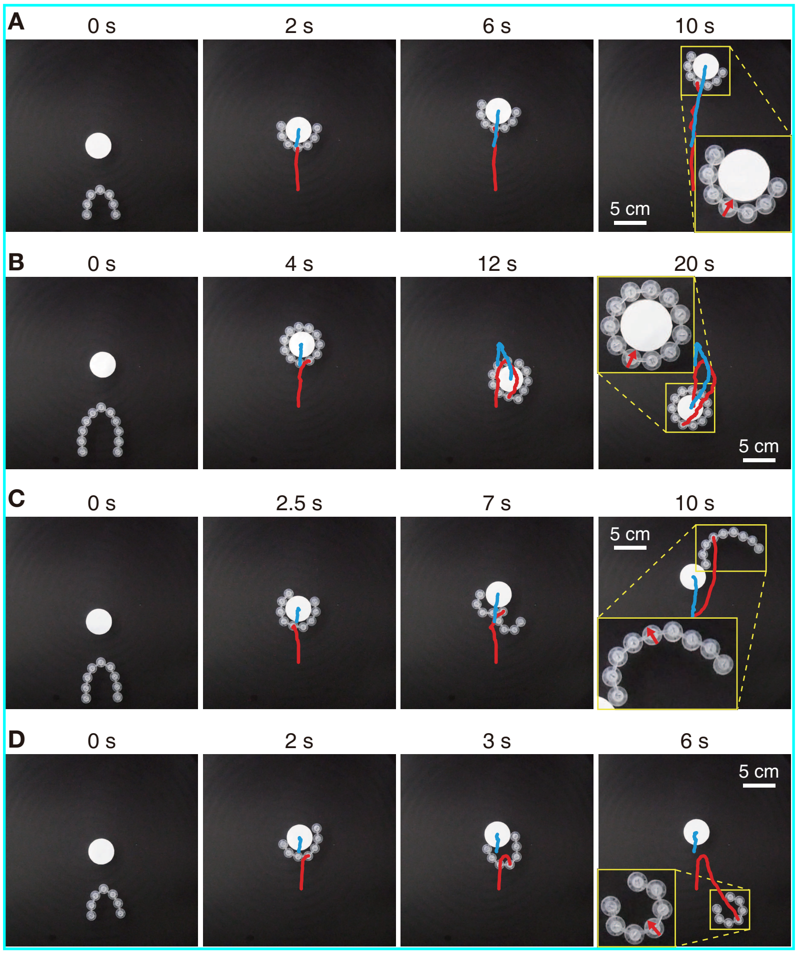

Figure 4.11: Different chain behaviors when encountering a single, mobile circular object. **A**, A chain with $N = 7$ and $\theta_3 = 75^\circ$ carries the object forward. **B**, A chain with $N = 11$ and $\theta_3 = 75^\circ$ carries the object backward. **C**, A chain with $N = 9$ and $\theta_3 = 60^\circ$ moves forward away from the object. **D**, A chain with $N = 7$ and $\theta_3 = 45^\circ$ moves backward away from the object. The blue and red lines show the trajectories traveled by the object and center particle of the chain, respectively, from their initial positions. The diameter D of the object is $D/d = 2.67$, and the angle θ_1 is 90° in all experiments.

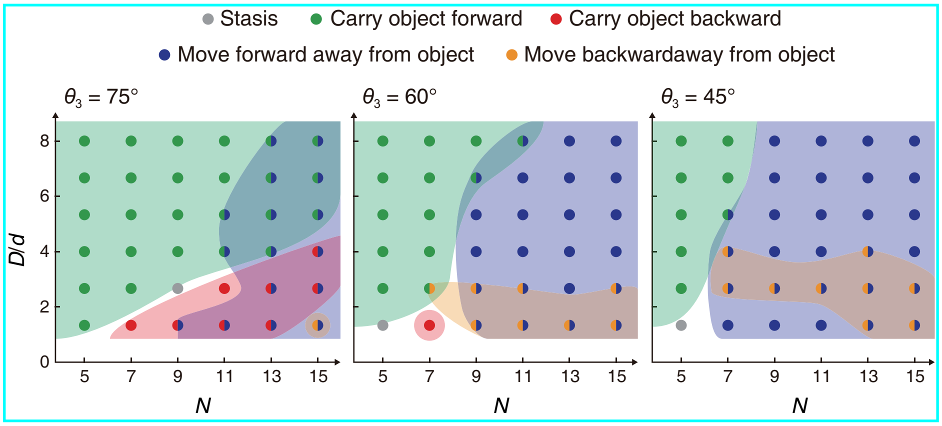

Figure 4.12: Regime map of chain behavior after colliding with an unanchored, mobile object according to the number of particles N and object diameter D at three θ_3. Bicolored circles indicate that two behaviors appears in same condition.

we calculated the magnitude of the angle θ_R by which the particle n$^{\text{th}}$ from the center has rotated with respect to the orientation of the center particle as follows:

$$\max\left(\frac{\pi + 3\beta - \theta_2 - 2\theta_3}{2}, \frac{\pi + \beta - 2\alpha - 2\theta_1}{2}\right) \le \theta_R \le \min\left(\frac{\pi + 3\beta + \theta_2 - 2\theta_3}{2}, \frac{\pi + \beta - 2\alpha}{2}\right) \quad \text{for} \quad n = 1\,, \tag{4.1}$$

$$\frac{\pi + (2n+1)\beta - \theta_2 - 2\theta_3}{2} \le \theta_R \le \frac{\pi + (2n-1)\beta + \theta_2 - 2\theta_3}{2} \quad \text{for} \quad 1 < n < \frac{N-1}{2}\,, \tag{4.2}$$

$$\frac{\pi + (N-2)\beta - \theta_2 - 2\theta_3}{2} \le \theta_R \le \frac{\pi + (N-2)\beta + \theta_2 - 2\theta_3}{2} \quad \text{for} \quad n = \frac{N-1}{2}\,, \tag{4.3}$$

where $\beta = 2\arcsin[L/(D+d)]$ is the angle formed by the two lines connecting the object's and nearby particles' centers. Assuming that orientation

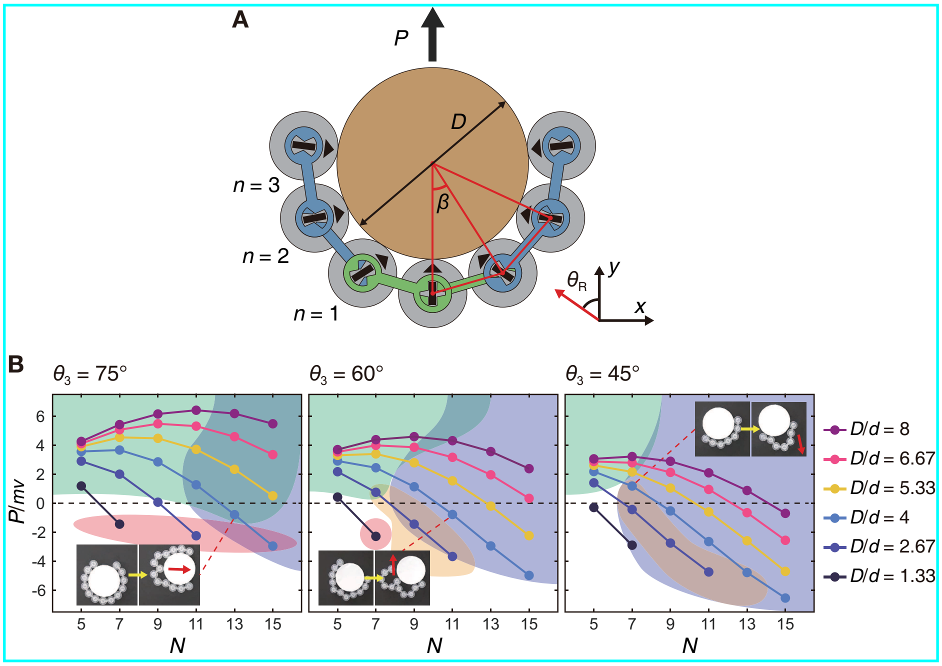

Figure 4.13: Momentum of a chain in conformal contact with an object. **A**, Schematic of a particle chain having a momentum of P in conformal contact with a circular object. **B**, Normalized momentum of the chain in conformal contact with the object in each condition. The colored areas indicate the regimes represented by the same colors in Fig. 4.12. The inset images show the chains losing conformal contact and finally moving in the opposite direction to the calculated momentum.

of each particle is aligned to the middle of each angular range $\theta_{\mathrm{R,m}}$, we displayed the normalized momentum of the chain, $P/mv = \Sigma \cos\theta_{\mathrm{R,m}}$, when the chain length is no longer than the the condition of entirely enclosing the object. The result is shown in Fig. 4.13B where the colored areas represent the regimes depicted in Fig. 4.12 with the same colors. In general, chains in conformal contact with larger objects have lower deformation curvature, which makes structure have greater momentum. The curvature effect causes the length of chain at which momentum begins to decline to be longer for larger objects.

The change in chain momentum with respect to N represents the forward momentum of the particles added to both sides. The decrease in momentum implies that the added particles are propelled backward, which makes it possible for both ends of the chain to be pushed backward. Retraction on both sides leads the chain to lose contact with and eventually move away from the object, which is consistent with the blue regime beginning where momentum begins to diminish. The mild negative momentum generated when the chain with large θ_3 entirely encloses the object allows the chain to keep enclosing and transport the object backward. Under similar conditions, chains with low θ_3 tend to lose contact separate from the object due to either increased backward propulsion at both ends or excessive negative momentum, which results in behaviors shown in Fig. 4.11C and 4.11D. Inset images in Fig. 4.13B illustrate examples of chains modifying their shape as both sides are pushed back, afterwards traveling in the opposite direction of momentum upon conformal contact. This is because the shape change caused by both sides pushing back causes the chains to have momentum in the opposite direction to that when it is assumed to make conformal contact.

Carrying an object forward enables a more detailed analysis of the carrying speed. The predicted momentum of the chain when enclosing the object gives us a decent estimate of how fast it will carry the circular object. Calculating the speed by momentum, with each particle's speed set to 33 mm/s, reveals that the estimates fit well for various object sizes at

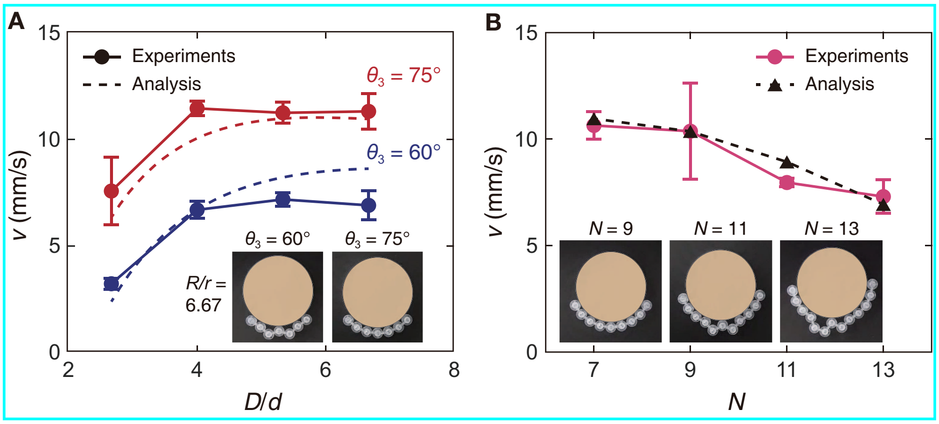

Figure 4.14: The speed at which chains carry circular object forward. **A**, The relationship between object diameter and carrying speed for chains with $N = 7$. **B**, The relationship between chain length and carrying speed for chains with $\theta_3 = 75^\circ$.

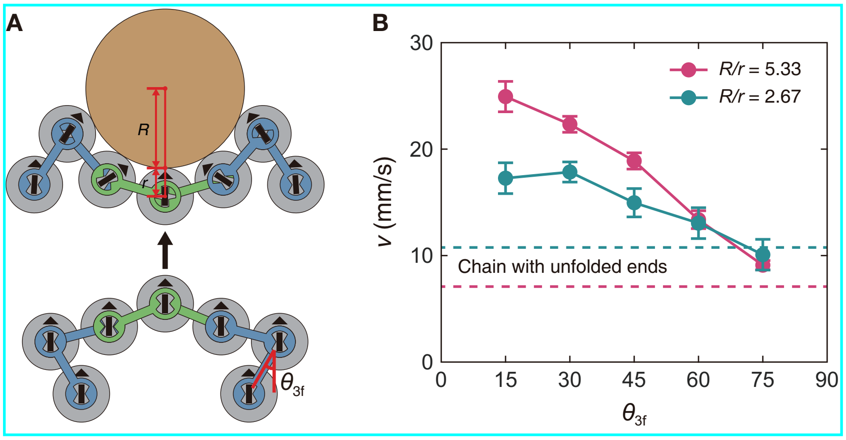

Figure 4.15: Carrying an object on a chain with folded ends. **A**, Schematic of a chain with inverted links of θ_{3f} at both ends pushing a circular object. **B**, The relationship between θ_{3f} and carrying speed for chains with folded ends under the condition of $N = 7$, $\theta_3 = 75^\circ$. The horizontal dashed lines indicate the carrying speed for chains with unfolded ends.

$\theta_3 = 75^\circ$ (Fig. 4.14). For low θ_3 and large N, the difference between anticipated and observed values is not negligible because the chain fails to make conformal contact with the object due to retraction on both sides. Furthermore, the speed can be enhanced by modifying the chain design. Flipping the links with θ_3 at each end causes the chain ends to bend inward, allowing the particles at the ends to face forward (Fig. 4.15A) and thus making the objects to be transported quicker. The θ_3 of the inverted connections is denoted here as $\theta_{3\mathrm{f}}$. Chains with folded ends carry objects faster than original, unfolded chains, except when $\theta_{3\mathrm{f}}$ is too large ($\theta_{3\mathrm{f}} = 75^\circ$), and the optimal $\theta_{3\mathrm{f}}$ for maximum speed depends on the object size (Fig. 4.15B).

We now look at scenarios in which the chain encircles a fixed object. The chain's ability to enclose an object is not restricted to a circular shape. A chain may surround objects of various shapes such as ellipses, squares, triangles, L and cross shapes without losing contact (Fig. 4.16), demonstrating its ability to enclose objects of complex shapes. The ability of the chain to maintain enclosing an object can be further enhanced by introducing folded ends. As previously stated, retraction at both ends precludes the chain from keeping conformal contact with the object. Even under the conditions that the chains without folded ends move away from the objects as depicted in Fig. 4.12, a chain folded at both ends with suitable $\theta_{3\mathrm{f}}$ can keep surrounding the objects (Fig. 4.17). Both ends of a chain with small $\theta_{3\mathrm{f}}$ are repeatedly brought together and spread apart. If $\theta_{3\mathrm{f}}$ is too large, on the other hand, the force that keeps the ends of the chain from pulling back is weak, so the chain is likely to move away from the object like a chain without folded ends.

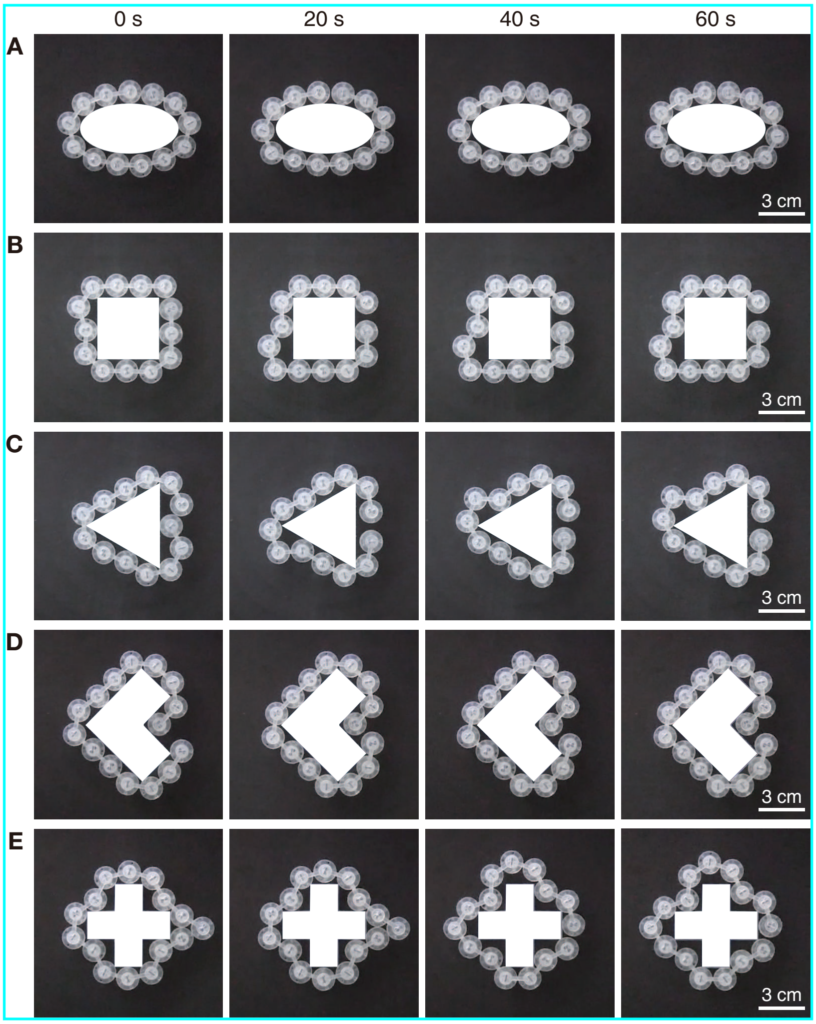

Figure 4.16: Chains enclosing objects of different shapes. **A**, Ellipse. **B**, Square. **C**, Triangle. **D**, L shape **E**, Cross shape. In all experiments, the angle θ_1 and θ_3 are 90° and 75°, respectively.

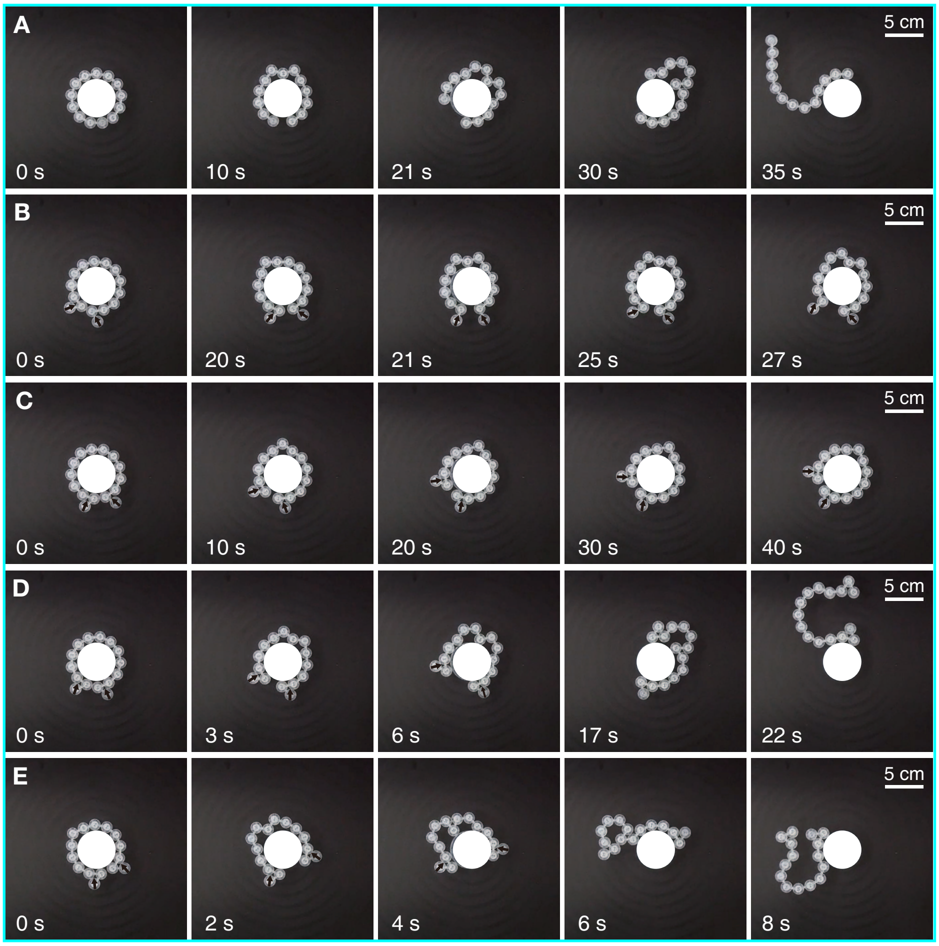

Figure 4.17: Effect of θ_{3f} on keeping a fixed object enclosed. **A**, A chain with $N = 11$ does not leave an circular object of $D/d = 2.67$. **B**, A chain with $N = 13$ move away from an object of $D/d = 3.33$. If two particles are added to both ends of the chain via an inverted link with θ_{3f} compared to the condition of (**B**), a chain with (**C**) $\theta_{3f} = 15^\circ$ remains enclosing the object with an ends that repeats widening and narrowing, while a chain with (**D**) $\theta_{3f} = 30^\circ$ maintains the surrounding with little opening. A chain with (**E**) $\theta_{3f} = 45^\circ$, (**F**) 60°, and (**G**) 75° moves away from the object by pushing back on both sides, just like a chain without folded ends. In all experiments, the angle θ_1 and θ_3 are 90° and 75°, respectively.

4.5 Chains encountering narrow space

4.5.1 Behavior when encountering a narrow gap

When the chain is directed into a narrow gap, the folding and spreading of the chain structure allow for intriguing phenomena. Even with large θ_1 and θ_3, which is likely to extend the chain structure outward, a chain with its center toward the gap can pass through the gap as it is folded around the center (Fig. 4.18A). Whereas, a chain with its center slightly to the side of the gap does not pass through but closes the gap (Fig. 4.18B). When the center deviates slightly from the center of the gap, the chain cannot be folded around the center, and the considerable resistance from the tiny gap and the two walls prevents it from moving further. If the chain is long, it can block a gap over a wide range of positions. We discovered that a long chain skewed to one side of the gap may not even cross a gap of $g = 3d$ (Fig. 4.18C); for $g > 3d$, particles on the gap side is likely to flow through the gap and surround the wall if there are no additional factors that prevent movement such as folded ends. The design of chain structure, which drives the particles toward the center particle when stretched from side to side, leads the chains center to adhere strongly to the wall and prevents passage of the chain from passing through the gap.

The gap-blocking chain allows for the selective passage of objects via the narrow gap. Due to the significant resistance from the two walls and a narrow gap in the direction of the chain, the chain can prohibit approaching objects on its side from reaching the opposite side (Fig. 4.19A). Objects on the other side of the chain, on the other hand, can pass through the gap by pushing the chain as far as they can resist the momentum of all or part of the blocking chhain. After the object goes through the gap, the chain exhibits two different behaviors depending on the position of the chain that has been closing the gap. When the center particle is originally close to the gap, the moving object is likely to pull the chain's center into the gap, causing the chain to move to the other side and eventually leaving the gap open (Fig. 4.19B). In constrast, the chain whose center was distant from

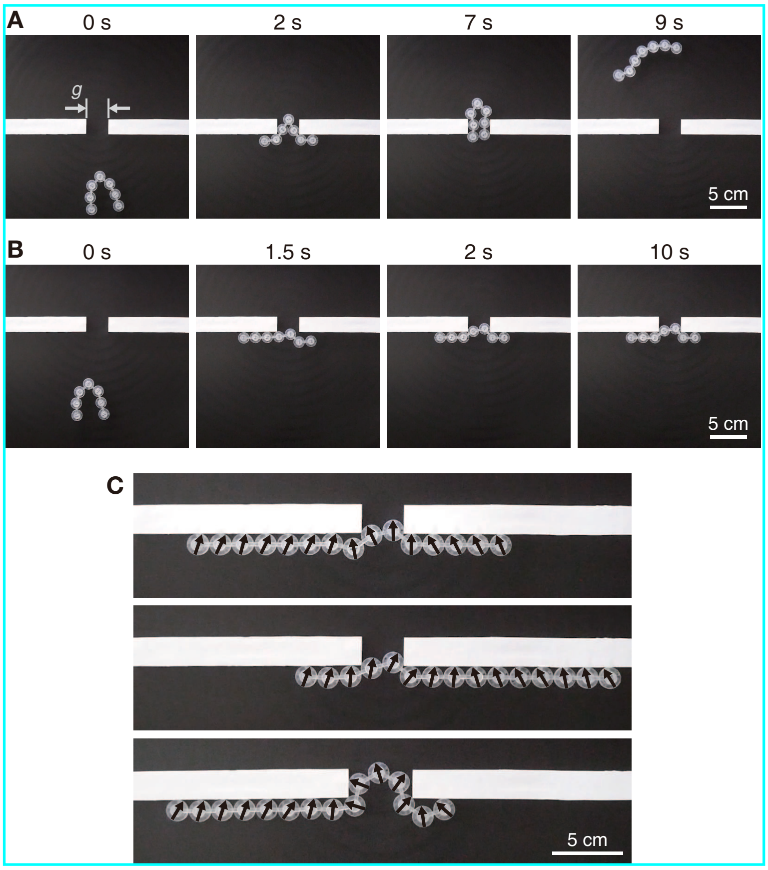

Figure 4.18: Different chain behaviors when encountering a narrow gap. A chain with $N = 7$ (**A**) passes through or (**B**) and fail to pass through the gap of spacing $g = 2d$ depending on the position reached. **C**, A chain with $N = 15$ blocking the gap of $g = 2d$ (left, middle) and the gap of $g = 3d$ (right). The black arrows show the orientation of each particle. The angle θ_1 and θ_3 are 90° and 75°, respectively, in all experiments.

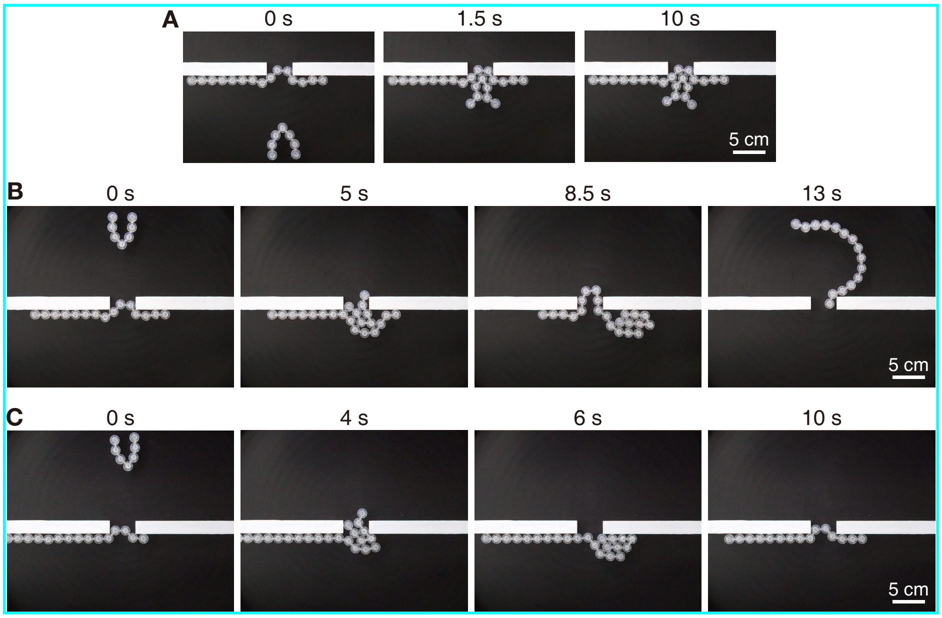

Figure 4.19: Behavior of a chain blocking a narrow gap when an object approaches to the gap. **A**, A chain with $N = 15$ that was closing a gap prevents a short chain with $\theta_1 = 20^{\circ}$ and $\theta_3 = 15^{\circ}$ moving upward from passing through a gap of $g/d = 2.67$. At the same gap spacing, the blocking chain allows the short chain moving downward to pass through, then the gap (**B**) opens or (**C**) stays closed depending on the center position of the chain that was blocking the gap.

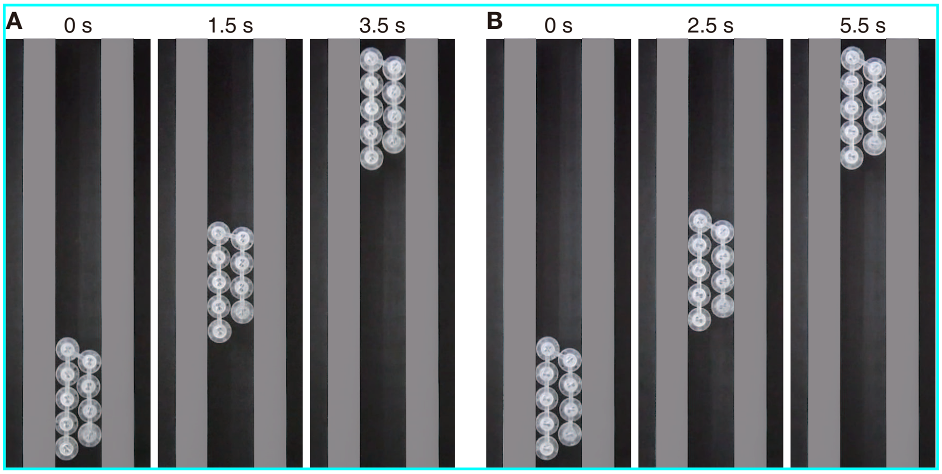

Figure 4.20: Chains moving along a narrow channel. A chain composed of nine particles with (**A**) $\theta_3 = 15^\circ$ and (**B**) $\theta_3 = 75^\circ$ moves in a channel with a spacing of $2d$.

the gap travels slightly to the side as it meets the object, and it again closes the gap (Fig. 4.19C). This result shows that even with repeated passing of objects, a very long chain with its center skewed far away from the gap will keep the gap closed for a long time.

4.5.2 Dynamics inside a narrow channel

The confinement affects the chain's travel speed when it enters a long, narrow channel rather than a short gap. Fig. 4.20A and 4.20B illustrate chains with $\theta_3 = 15^\circ$ and 75°, respectively, moving in a channel with a spacing of $2d$. We see that a chain with a smaller θ_3 moves faster. The chain's speed in the narrow channel is depicted in Fig. 4.21A, where it declines with θ_3 and seems to be nearly independent of N. This decrease in speed occurs because increasing θ_3 causes the particles to rotate towards both walls, reducing their momentum in the direction of movement. In the channel, chains with $\theta_3 = 15^\circ$ and 75° travel around 25% and 60% slower, respectively, than a single undisturbed particle ($v = 80$ mm/s). As

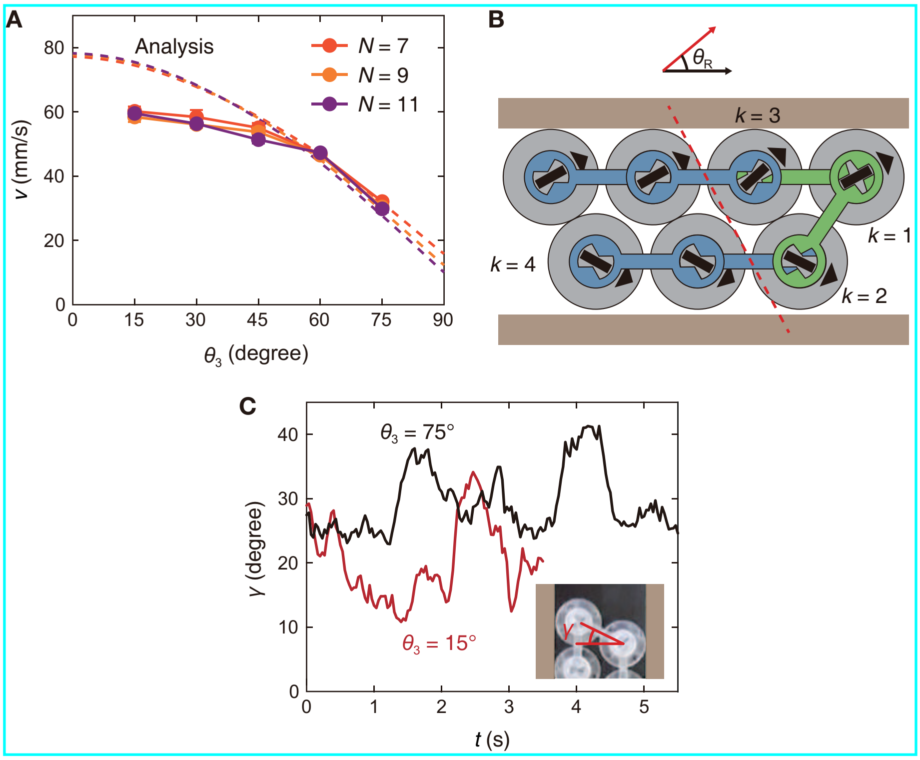

Figure 4.21: Dynamics of chains in a narrow channel. **A**, Average speed of chains with different N and θ_3 moving in a channel shown in Fig. 4.20. **B**, Schematic showing the orientation of each particle when a chain is fully folded and the particles on each side are aligned parallel to the wall. The dotted lines are prediction by assuming the geometry of chain as **A**. **C**, The angle between the vertical line of the channel wall and the line connecting the centers of the front two particles in the moving chain.

shown in Fig. 4.13, the speed can be predicted by analyzing the direction of each particle. The speed is estimated by assuming that the chain in the channel moves with particles on either side lined up parallel to the channel wall and particles touching each other, as schematically shown in Fig. 4.21B. Through geometric analysis, we calculated the magnitude angle θ_R by which each particle has rotated with respect to the direction of the chain's progression as follows:

$$\theta_\mathrm{R} = \alpha \quad \text{for} \quad k = 1\,, \tag{4.4}$$

$$\max\left(-\frac{\theta_2}{2} - \theta_3, \alpha - \theta_1\right) \leq \theta_\mathrm{R} \leq \min\left(\frac{\theta_2}{2} - \theta_3, \alpha\right) \quad \text{for} \quad k = 2\,, \tag{4.5}$$

$$\max\left(\theta_3 - \frac{\theta_2}{2}, \alpha\right) \leq \theta_\mathrm{R} \leq \min\left(\theta_3 + \frac{\theta_2}{2}, \alpha + \theta_1\right) \quad \text{for} \quad k = 3\,, \tag{4.6}$$

$$\theta_\mathrm{R} = \theta_3 \quad \text{for} \quad k = 4\,. \tag{4.7}$$

Assuming that orientation of each particle is aligned to the middle of each angular range $\theta_\mathrm{R,m}$, we displayed the estimated speed as dotted lines in Fig. 4.21A. For large θ_3, the anticipated speed agrees well with the experimental value, but the discrepancy grows as θ_3 gets smaller. The strong momentum in the direction of movement of the chain with tiny θ_3 is likely to bring adjacent particles close to horizontal (Fig. 4.21C), and the resulting high resistance by jamming between two walls makes the chain move slower than expected.

4.6 Chain design principles and possible combination of functions

The results so far shows that particle chains composed of SPPs exhibit different behavior depending on the design parameters of the links. Here, we summarize the criteria for chain design parameters for the aforementioned functions. As mentioned in §4.3.1, we fix θ_2 at 60° which gives a chain possessing suitable degrees of flexibility and interparticle interaction across a broad spectrum of θ_2, and provide a range of θ_1, θ_2, and N for each function. In the table below, adjusting the parameter within each range changes the distance the chain travels and the speed at which it moves or behaves.

Functions	θ_1	θ_3	N
Continue moving in a single direction without getting stuck	$< 30^\circ$	$< 30^\circ$	·
Patrol within a certain range along objects or walls	$30^\circ \leq \theta_1 < 50^\circ$	$< 40^\circ$	·
Change direction to get around obstacles	$< 50^\circ$	$30^\circ \leq \theta_3 < 40^\circ$	·
Maintain contact with objects	$75^\circ <$	large	
– Carrying objects forward	"	"	$\ll \pi D/l$
– Carrying objects backward	"	$60^\circ <$	$\simeq \pi D/l$
Loss contact and move away from objects	small	small	large
Block narrow gaps	$45^\circ <$	$45^\circ <$	·
Move quickly along walls or narrow channels	·	small	·

A particle chain of specific designs is not limited to a single functionality. For tasks that can be accomplished under the same link conditions, a chain can accomplish them in succession without switching links in between. For example, a chain with $N = 11$ and $\theta_3 = 75^\circ$ can completely enclose an object with a diameter of $D/d = 2.67$ and then carry it backwards, and it can also pass through a narrow gap or channel. This means that, as shown in Fig. 4.22A, the chain can fully surround or carry an object beyond the narrow passage.

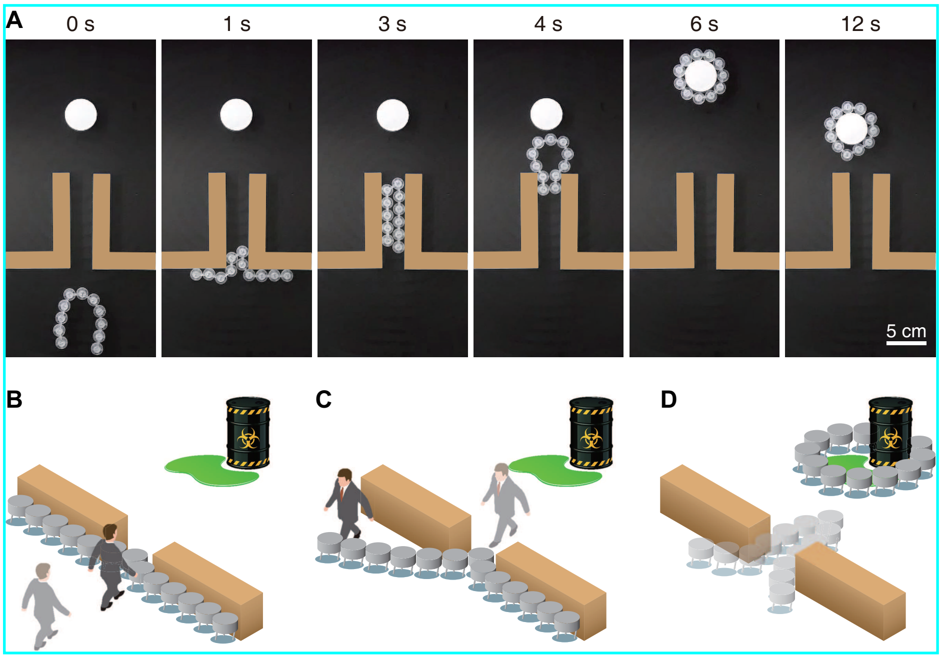

Figure 4.22: Chains performing tasks in an environment with a narrow space. **A**, A chain composed of eleven particles with $\theta_3 = 75^\circ$ traverses a narrow channel and carries an circular object backward after completely enclosing it. Schematic illustrating a particle chain that (**B**) prevents people from approaching an area where a toxic substance is leaking, (**C**) then permits people to leave the area, and (**D**) then moves to encircle the hazardous area.

A long chain structure that can perform multiple functions in succession can be used in a disaster environment or in a situation where dangerous substances are found. A chain structure outside the harmful place can block the passage of people approaching the place (Fig. 4.22B). On the other hand, it can be easily opened by someone trying to get out of the dangerous area to allow escape (Fig. 4.22C). After the escape of several people, the chain can enter the area and perform further actions, such as covering a hazardous location or moving a harmful material (Fig. 4.22C). This continuous behavior shows the an example of the physical intelligence of a particle chain that behaves according to its environment and purpose only through physical contact.

4.7 Conclusions

Despite numerous attempts to develop intelligent systems out of mindless active particles, existing particle-based robotic machines are limited to simple or narrow-range functions. We established in this chapter, through a series of experiments, that a particle chain made of SPPs is capable of executing desired locomotion and different functions in complex environments that particle swarms cannot achieve without sophisticated external control. Our approach is to connect these non-intelligent particles using rigid bars with ribbon-like slots on each side, giving the chain the chance for communication between neighboring particles as well as a high degree of deformability. The interparticle motion and location of each particle are determined by the links' three design parameters, θ_1, θ_2, θ_3, and the total number of particles forming a chain. The morphological control allows the chain to move through or around obstacles, stick to or fall from an object, transport objects forward or backward, penetrating or blocking small gaps, and allowing or obstructing the passage of objects through the gaps. Due to the degree of freedom of each particle's motion, the chain does not always exhibit the same behavior under the same conditions. However, optimizing the design parameters as well as the symmetrical structure results in a system with predictable functions.

Our research could be expanded to include non-rigid, flexible links. The curvature of the flexible link is determined by the stiffness of the link, the propulsion force on the particle, and the shape of the objects the chain will encounter. A design that takes into account the deformation of the link can allow for the implementation of a broader variety of functions than the system shown in our study. Furthermore, using connections that can be altered by external fields enables for remote programming of chain behavior. The current study is limited to an initially fixed design. By remotely reconfiguring the slots on each link, the chain can perform a range of diverse, even competing tasks instantly on demand.

With the opportunity to enhance the design, our approach to manufacturing particle chains can be utilized as a starting point for creating simple yet versatile robots at any scale. Robotic tools in medical applications are one example. Because these modular structures are very versatile and flexible, they should be able to travel easily through soft tissues or small vessels to perform functions like drug delivery, hole sealing, or target-site capture. Our method can also be applied to the development of sturdy and low-cost robots capable of infiltrating complicated terrain for object transfer, environmental monitoring, or traffic management. We hope that the findings of our research will help us create robots capable of executing complicated functions with minimal materials at any length scale.

Chapter 5

Concluding remarks

In the concluding chapter, we begin by providing a brief summary of our key findings in §5.1. Then, we suggest potential research subjects for future studies that are inspired by the experimental and analytical findings of this thesis in §5.2.

5.1 Summary of findings

Based on a comprehensive understanding of particle and robotic swarms, we have explored the dynamics of single or cluster of particles, and reconfigurable behaviors and functions of two-dimensional structures composed of nonintelligent particles without sophisticated external control. Using a vibrating baseplate and particles designed to be propelled by vertical vibration, we have conducted research in three distinct topics. First, we proposed a densely packed particle system and demonstrated the dynamics of self-propelled particles (SPPs) in dense granular media. Second, based on the particle dynamics in a dense environment, we have created dense particle structures composed of particles and mobile boundary, and shown that they can exhibit a wide range of motions. Third, we have created new structures, particle chains, by linking several SPPs and showed their high adaptability and versatility under various conditions. Our experiments and analysis shows that morphological control, utilizing the physical relationship between various elements within a system to regulate its behavior, allows us to easily reconfigure the structures for different purposes.

In chapter 1, we began by describing the motivation of the study that development of a variable and multifunctional system is in high demand at various scales. We then mentioned that clusters of units serve this purpose well, and introduced some examples of natural swarms and various artificial swarm systems that have been developed in recent years. We point out the limitations of existing systems that use intelligent units or are externally controlled, and demonstrate how simple active particles can be used to create highly functional robotic machines by adopting constraints that resemble cells and biomolecules.

In chapter 2, we presented a system in which a small number of SPPs are mixed with nonpolar particles that are randomly vibrated in a two-dimensional circular confinement. We first designed particles with thin legs to respond to vertical vibration, and confirmed random or directional movements of the particles depending on the tilt angle of their legs. Using vibrated particles, showed that a single SPP with high polarity (leg tilt angle) exhibits superdiffusion in a dense granular medium, with the diffusion exponent increasing with the aspect ratio (AR). A quantitative analysis of the forces acting on the particles reveals that a high aspect ratio SPP can penetrate between neighboring particles significantly better than a low aspect ratio SPP. At confinement boundary, a single SPP move well along the boundary without moving to the bulk only at high AR, and multiple SPPs eventually form a cluster at the boundary. We found that this cluster tends to transition from a moving state to a static state as the number of SPP increases, which provides clues to changes in the behavior of particle clusters.

In chapter 3, we used the results in Chapter 2 to show how dense particle structures can perform various behaviors. These structures are distinct from many conventional particle ensembles having low number densities and therefore low structural stability. We created rigid particle structures by confining randomly vibtated particles and a few SPPs in a free-to-move boundary. We demonstrated that the way the structure behaves is closely linked to the ability of SPPs to travel through the surrounding dense particles. The structures show polar motion or rotating motion when a single SPP stays in the bulk or moves along the boundary, respectively. In case of SPPs moving along the boundary, the number of SPPs influences their orientation with respect to the boundary, which changes the polarity and chirality of the structure. We finally showed that the behavior of the dense structure is further adjusted by the particle number density and boundary properties.

In chapter 4, we show a reconfigurable particle chain that can carry out a variety of behaviors and functions only using SPPs. We modified the design of the SPP used in chapter 2 and 3 for interparticle connection, and connected two adjacent particles using links to create a nonloop chain. To regulate the behavior, we employ morphological control that modifies the relative motion of adjacent particles based on the parameters of the connecting links. This modification of flexible structures allows for unidirectional or reciprocating motion and enables particles to generate propulsive force when they encounter obstacles. We quantitatively and qualitatively described the factors that determine the direction of motion and the mechanism of reorientation. To demonstrate high adaptability and functionality of the chains, we showed that they can carry out a range of conflicting tasks such as passing or enclosing objects, changing or maintaining movement direction, pushing or pulling loads, and blocking or infiltrating narrow space. We also constructed theoretical models to help predict the speed of transporting objects and moving through narrow channel.

Overall, we anticipate that the scalability, material independence, and programmability of our approach to modulate particle structures can be applied to the development of reconfigurable and autonomous systems comprised of only simple components at any scale.

5.2 Future works

In this thesis, we have introduced two reconfigurable particle collective systems and describes the behavioral mechanisms of each system. We have advanced previous work on enclosing several simple robots with boundaries or linking them together to create particle structures with a broader range of functions. We believe that our approach is highly scalable and can be used as a starting point to develop various existing systems. Following are some suggestions for future studies related to this research.

Studying the dynamics of dense particle structures adopting soft components

The self-organization behaviors of the system can be examined in the context of a highly flexible confinement boundary. It is expected that the interaction between SPP ordering and membrane deformation will result in a wide range of collective dynamics in such systems. The investigation of their activities may yield insights into the dynamic characteristics of cells and vesicles, which are complex systems composed of various SPPs enclosed by extremely deformable membranes. Moreover, it is necessary to determine the applicability of our findings to situations where the particles are made of a softer material and are therefore very flexible. The suggested study could show how very mobile and invasive cells spread through a densely packed epithelial tissue. This would be a big deal for the fields of morphogenesis and cancer metastasis.

Investigating the influence of non-rigid links on chain behavior

We could extend our study of particle chain to include non-rigid links. The stiffness of the link, the self-propulsion force of the particle, and the shapes of the objects the chain will encounter all affect how the flexible link will deform. Compared to the system illustrated in chapter 4, a design that considers the deformation of the link can enable the implementation of a wider range of functions. Additionally, using links that are subject to change by external stimuli makes it possible to remotely control the chain behavior. The present investigation is constrained by a design and material properites that was initially predetermined. By remotely changing the shape of slots and the mechanical properties of each link, the chain can instantly and on demand execute a variety of different, even competing tasks.

The studies presented above concerns how particle structures can be refined in the near future. From a long-term perspective, we expect our findings to have the following ripple effects.

Developing a new paradigm of mechanical systems

Our work on highly reconfigurable collective systems will pave the way for future development of mechanical systems with high degrees of freedom, where the shape and functions of the structures quickly and adaptively change shape in response to external environmental stimuli. Such properties may minimize unnecessary movement or reaction time beyond what the user intended. Therefore, the systems can be applied to novel machines or robots that interact with humans of operate with minimal information and resources in hazardous areas and disaster relief sites. It also has potential applications in the field of patient-customized medicine such as drug delivery vehicles, structural reinforcements, and surgical robots that can be injected into the body through minimally invasive procedures and deform, separate, and coalesce as needed.

Pioneering a new paradigm in basic academic fields

Continued research on highly adaptive collective systems will also open up new paradigms in many fundamental fields of study. For example, sophisticated self-assembly systems will advance the fields of soft matter physics, which deals with the behavior of unconventional materials, and biomimetics, which analyzes and simulates the collaborative processes of living organisms. The exploration of emergence will provide the theoretical and technical foundations for creating systems including artificial life and nervous systems that humans have yet to fully emulate. Furthermore, understanding the universal principles of irreversible processes, information processing, and emergent phenomena in the presence of multiple interactions is one of the most fundamental challenges in the field of complex systems and statistical physics. Thus, this research will expand and deepen the theoretical basis for exploring various problems in life sciences, control theory, and information theory from the perspective of statistical physics.

Appendix A

Detailed analysis

This chapter provides a more detailed analysis of the dynamics of a single SPP and SPP cluster covered in §2.3, §2.4, and §2.5 of chapter 2. This analysis has been done in collaboration with Professor Yongjoo Baek in the Department of Physics and Astronomy.

A.1 More detailed characterization of a single SPP motion

The superdiffusion of a single SPP in a dense environment, which is shown in Fig. A.1, suggests that the motion of a single SPP contains non-trivial long-range temporal correlations. To further describe the motion, we also examined the time-averaged mean squared angular displacement $\langle\overline{\Delta\theta_{\mathrm{o}}(t)^2}\rangle$. Here, $\langle\overline{\Delta\theta_{\mathrm{o}}(t)^2}\rangle$ is defined as

$$\langle\overline{\Delta\theta_{\mathrm{o}}(t)^2}\rangle = \left\langle \frac{1}{T-t}\int_0^{T-t} dt' \left[\theta_{\mathrm{o}}(t'+t)-\theta_{\mathrm{o}}(t')\right]^2 \right\rangle, \tag{A.1}$$

where $\theta_{\mathrm{o}}(t)$ indicates the orientation of the self-propulsion force. As shown in the inset of Fig. A.1, the angular motion already shows normal diffusion on a subsecond time frame. This means that the SPP's angular motion is essentially an unbiased Brownian motion with a randomly fluctuating

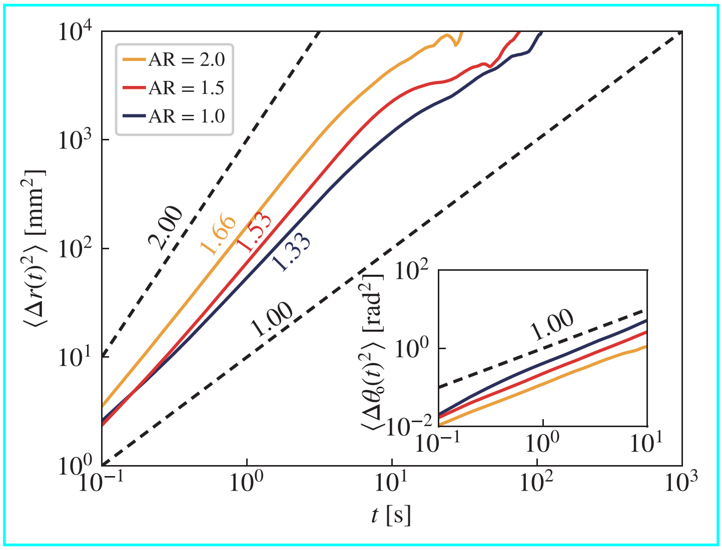

Figure A.1: The time-averaged mean squared displacement of the SPP in a dense environment. (Inset) The time-averaged mean squared angular displacement of the same SPP under same condition.

torque whose autocorrelation decays quickly over time. The orientation θ_{o} becomes completely randomized on a time scale longer than the inverse of the angular diffusion coefficient, and the position of the SPP begins to show normal diffusion. It is also noteworthy that a higher AR results in a smaller angular diffusion coefficient. This is because the torque imparted by the surrounding isotropic particles suppresses the angular motion of SPPs with a higher AR more strongly. Due to this effect, the SPP with a higher AR maintains its initial orientation for a prolonged period of time, as depicted in Fig. 2.2A.

Now we discuss the axial motion of the SPP. For this purpose, we investigate the properties of the SPP's axial velocity and axial displacement, which are respectively defined as

$$v_{\parallel}(t) \equiv \dot{\mathbf{r}}(t) \cdot \hat{\mathbf{e}}_{\theta(t)}, \quad l_{\parallel}(t) \equiv \int_0^t dt'\, v_{\parallel}(t'), \tag{A.2}$$

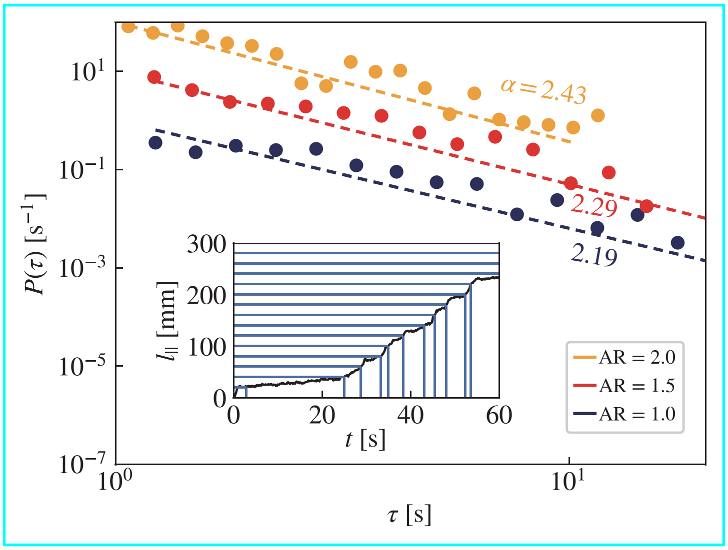

Figure A.2: The interevent time probability $P(\tau) \sim \tau^{-\alpha}$ characterizing the axial motion of the SPP with $\theta_L = 10^{\circ}$ in a dense environment. (Inset) An example of the time evolution of the axial displacement.

where $\hat{\mathbf{e}}_\theta \equiv (\cos\theta_o, \sin\theta_o)$ denotes the orientation of the self-propulsion force. By this definition, $l_{||}$ increases (decreases) if the SPP moves in the direction of (against) its self-propulsion. As shown in the inset of Fig. A.2, $l_{||}$ rarely decreases in time but rather increases through a sequence of steps interspersed with plateaus of varying lengths between adjacent pairs of steps. This indicates that the SPP is typically confined by a cage composed of the surrounding particles, but sometimes it can move forward by cracking the cage.

To quantitatively characterize such motion, we measured the trapping time τ, which is defined as the time it takes for $l_{||}$ to increase by a step of 20 mm (the diameter of each nonpolar particle). Refer to the inset of Fig. A.2 for a visual representation, where the distance between each pair of adjacent vertical blue lines corresponds to an instance of τ. As shown in the main plot of Fig. A.2, its distribution exhibits a broad power-law

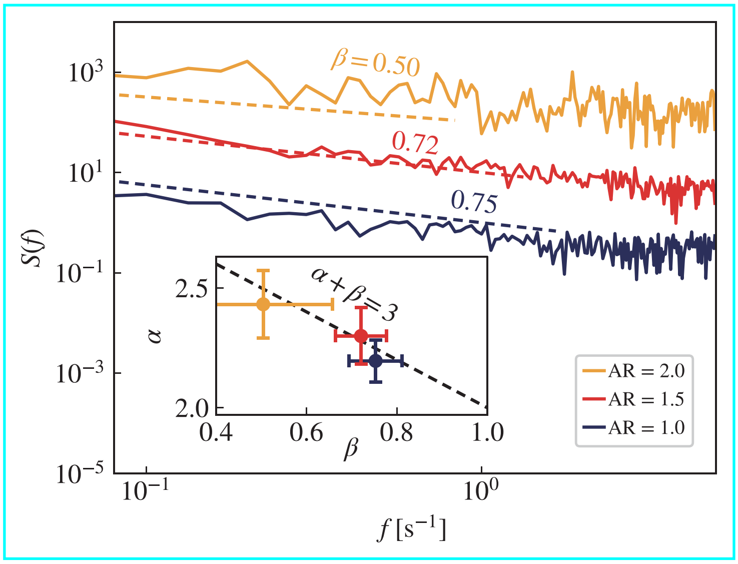

Figure A.3: The power spectrum $S(f) \sim f^{-\beta}$ of the axial velocity of the SPP in a dense environment. (Inset) The power-law exponents α and β satisfy the relation $\alpha + \beta = 3$ within the error bar.

tail $P(\tau) \sim \tau^{-\alpha}$ with $2 < \alpha < 3$. We also looked at the power spectrum $S(f) = |\hat{v}_{||}(f)|^2$ acquired from the Fourier transform

$$\hat{v}_{||}(f) \equiv \int_0^T dt\, v_{||}(t)\, \mathrm{e}^{-2\pi i f t} \tag{A.3}$$

of the axial velocity. The power spectrum, as shown in Fig. A.3, exhibits a $1/f$ noise behavior $S(f) \sim f^{-\beta}$ with $0 < \beta < 1$, where the exponent β decreases with AR. The inset of Fig. A.3 shows that the two power-law exponents α and β satisfy the relation $\alpha + \beta = 3$ within the error bars. Here we point out that a fractal renewal process, consisting of a sequence of delta-peak signals with a power-law interevent time distribution $P(\tau) \sim \tau^{-\alpha}$, is known to have a power spectrum $S(f) \sim f^{-\beta}$ with $\beta = 3 - \alpha$ provided that $2 < \alpha < 3$ (Lowen & Teich, 1993). As a result, it is possible to approximate the axial motion of the SPP as a fractal renewal process made up of static states (caging) with power-law distributed durations interrupted by sharp jumps of the same length (cracking). Because of the quasi-long-range temporal correlations found in the axial motion, the initial motion of the SPP is superdiffusive rather than diffusive or ballistic.

A.2 Calculation of cracking force by virtual work method

In chapter 2, we calculated the force P that an elliptic SPP of aspect ratio AR $= a$, moving with a self-propulsion force F pushes the neighboring nonpolar particles of radius R apart. For the calculation, we accounted for all actual forces and torques exerted in each particle which depends on the geometric and dynamical factors. Here we introduce a simpler way to calculate the cracking force without considering all of them under conditions where the friction effect can be ignored and the particles are in static mechanical equilibirum.

We use the coordinate system shown in Fig. 2.7C for the force analysis. According to the virtual work principle (Lanczos, 1986), the cracking force P and the self-propulsion force F must fulfill the relation

$$F\,\delta l + 2P\,(\delta b/2) = 0\,, \tag{A.4}$$

where δl and δb are infinitesimal virtual displacements associated with the horizontal distance between the SPP and nonpolar particls l and vertical distances between two nonpolar particles b. This relation gives the cracking force as

$$P = -F\,\frac{dl}{db} = -F\,\frac{dl/dX}{db/dX}. \tag{A.5}$$

We now express the two distance l and b as a function of X alone, where X is the x-coodinate of the point of contact $(X,\,Y)$. Using the angle θ between the x-axis and the line joining the center of the circle and the point of contact, the two distances can be express as $l = X + R\cos\theta$ and $b = 2(Y + R\sin\theta - R)$. From Eq. (2.10) and Eq. (2.11) in chapter 2, the

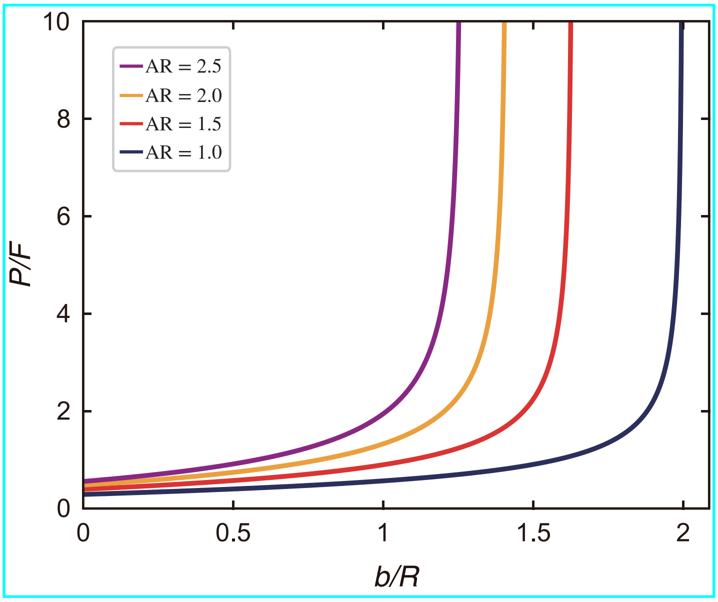

Figure A.4: The relative magnitude of the cracking force P/F applied by a single SPP with different AR as the gap b is varied. The solid lines indicate the force calculated by virtual work method, whereas the dotted lines indicate the force calculated taking into account all forces and considering the friction coefficient between particles of zero. All curves diverge when the gap reaches the thickness of the SPP.

two distances can be expresses only by X. We finally obtain the curves of the normalized cracking force P/F by substituting the two distances into Eq. (A.5), which is shown in Fig. A.4. In contrast to accounting for a finite friction coefficient, P diverges to infinity as b approaches the thickness of the SPPs at all ARs. We note that these curves are consistent with the values obtained by assuming the friction coefficient to be zero in the analysis in chapter 2, indicating that the virtual work principle is valid under conditions where energy is conserved.

A.3 A simplified model of the SPP cluster at the boundary

To further investigate the nature of the phases of the SPP cluster and the transition between them, we consider a simplified model of the cluster, shown in Fig. A.5A. We consider a two-dimensional (2D) system that is filled with particles of $N_{\text{tot}} = 25$, where a series of N SPPs (red-blue rigid dimers) propel themselves along their axis (green arrows), while the rest in front of SPPs are s series of isotropic particles without any self-propulsion(grey particles). Each isotropic particle is a (grey) particle of radius $a_1 = 6$. Each dimer consists of a smaller (red) particle of radius $a_2 = 4$ and a larger (blue) particle of radius $a_3 = 4.6$ separated by a fixed distance $l = 4$, so that the overall envelope of the dimer imitates the elliptic particle used in our experiments. The smaller (larger) particle corresponds to the front (rear) of the SPP, and the self-propulsion force $F = 100$ (green arrow) always acts on the center of the larger particle towards that of the smaller particle.

To represent the boundary accumulation of the particles, we ensure that all particles stay in contact with the boundary by constraining all isotropic (grey) particles and the smaller (red) particles of the rigid dimers to move along the 1D periodic line, which is a zero-curvature simplification of the circular confinement boundary used in our experiments. Here, the larger (blue) particles of the dimers are allowed to move in two dimensions to mimic the flipping behavior of the SPPs. The length of the 1D periodic line is set to be

$$L = 2a_1(N_{\text{tot}} - N) + 2a_2(N - 1) + (a_2 + a_3 + l), \tag{A.6}$$

which is roughly equal to the total length occupied by the particles, provided that all but one SPP stand perpendicular to the boundary and the remaining SPP completely leans against the boundary. In other words, this setting ensures that the system is densely packed with particles with the packing fraction close to one.

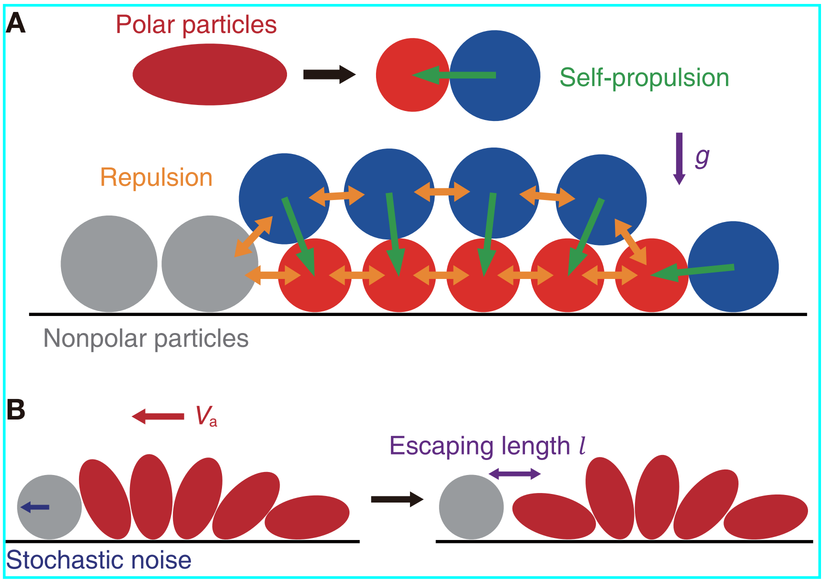

Figure A.5: Simplified one-dimensional model of the SPP cluster motion at the boundary. **A**, An illustration of our simplified model of the SPP cluster dynamics. The effective outward force applied by the bulk granular particles is indicated by g. **B**, An illustration of the effective process by which the moving SPP cluster gets stuck.

Now we describe three types of forces (other than the self-propulsion force F) acting on each of the particles. First, given the distance r_{ij} between particles i and j, their short-range repulsion is given by the gradient of the Weeks-Chandler-Andersen (WCA) potential (Weeks *et al.*, 1971)

$$U(r_{ij}) = \begin{cases} 4\varepsilon\left[\left(\frac{\sigma_{ij}}{r_{ij}}\right)^{12} - \left(\frac{\sigma_{ij}}{r_{ij}}\right)^{6}\right] + \varepsilon & \text{if } r \leq 2^{1/6}\sigma, \\ 0 & \text{if } r > 2^{1/6}\sigma, \end{cases} \tag{A.7}$$

where ε and σ_{ij} are characteristic energy and distance parameters. The latter parameter is the sum of the respective radii a_i and a_j of particles i and j. The interactions arising from this potential are indicated by orange arrows in Fig. A.5A. Second, there are random microscopic noise ultimately originating from the plate vibrations. While these forces have a characteristic driving frequency in the original experiment, here we represent them by a Gaussian white noise, simply focusing on the destabilizing effects of microscopic fluctuations. We put the diffusion coefficient associated with the noise equal to 4. Finally, we introduce a effective gravity g into the model, which corresponds to the outward pressure from bulk granular medium that tends to make the SPPs lean against the boundary. Implementing all the above elements, and assuming every particle to be overdamped with a mobility coefficient $\mu = 4$, their dynamics can be numerically integrated using the Euler method. As Fig. A.5A schematically shows, this model also exhibits persistent motion of the SPP cluster maintained by a symmetry-breaking mechanism very similar to the one observed in the experiment. Moreover, as illustrated in Fig. A.5B, the cluster mobility is eventually lost when the isotropic particle (grey) in front of the traveling cluster (red elliptic particles) moves sufficiently far away from the frontmost SPP, allowing it to lean against the boundary.

We first observe how the time-averaged velocity V_a of the SPP cluster changes depending on the number N of SPPs for different magnitudes of the gravity g. The model reproduces the existence of an optimal number of SPPs that maximizes the cluster velocity. This effect appears to be a result of the geometric shape of the SPPs. When N is small, the cluster velocity

V_a increases with N because each additional SPP adds one more pusher and one less isotropic particle to be pushed. But when N is increased further, the physical interference between elliptic shape of each SPP makes the front SPPs tend to be more and more tilted against the motion of the cluster. In this case, an additional SPP means an active obstacle that pushes the moving cluster away, instead of a passive obstacle that simply stays in front. Thus, V_a would eventually start to decrease when N goes above a certain threshold. If the boundary shown in Fig. A.5A bends upward (due to a finite radius of curvature of the boundary), the optimal N for maximum V_a would become smaller. This explains why the optimal N in the experiment (found to be 3 in chapter 2) is smaller than that found in our simplified model (found to be 5 in Fig. A.6A).

Next, we turn to the question of how a large SPP cluster transitions from a moving to a static state. As schematically illustrated in Fig. A.5B, for a moving cluster to be stuck at the boundary, the $N_\mathrm{tot} - N$ isotropic particles in front of the cluster should move far enough away from the frontmost SPP of the cluster by the length l of the SPP so that the SPP can fully lean against the boundary. This is comparable to overcoming an effective potential barrier, which is express as

$$\Delta E \sim \frac{(N_\mathrm{tot} - N) l V_\mathrm{a}}{\mu} \tag{A.8}$$

that arises from the fictitious force V_a/μ in the cluster frame. Assuming that the noise is characterized by some effective temperature T_eff, the Arrhenius' law states

$$\tau_\mathrm{cl} \sim \exp\left[\frac{\Delta E}{T_\mathrm{eff}}\right] \sim \exp\left[N \times \mathrm{constant}\right]. \tag{A.9}$$

For this reason, the lifetime of the moving cluster decays exponentially with the number of SPPs N, as shown in Fig. A.6B.

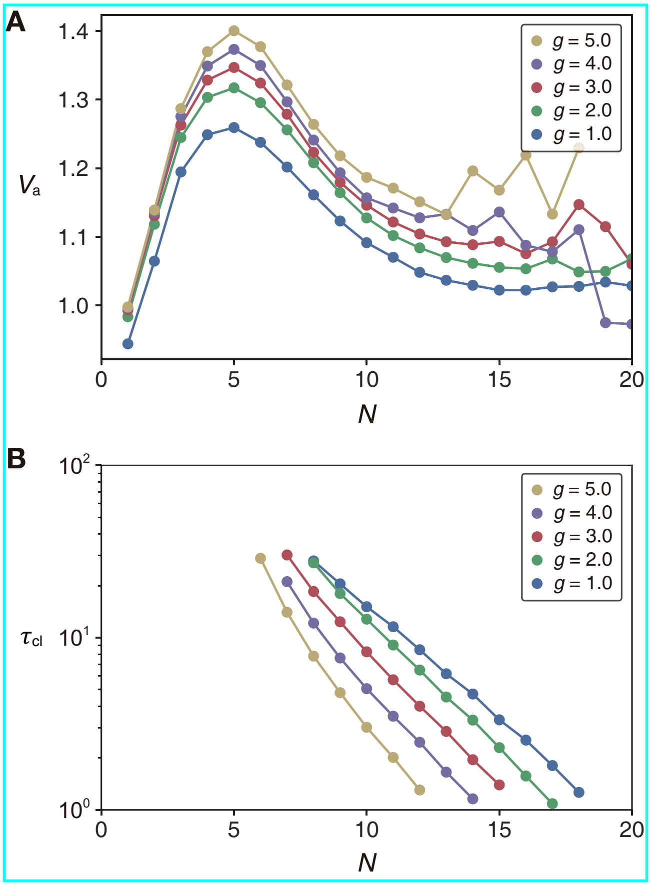

Figure A.6: The dynamic properties of SPP cluster at the boundary according to the simplified model. (**A**) The time-averaged cluster velocity V_a and (**B**) the mean lifetime τ_{cl} of the moving SPP cluster as g and N vary.

References

Abaurrea-Velasco, C., Auth, T. & Gompper, G. (2019). Vesicles with internal active filaments: self-organized propulsion controls shape, motility, and dynamical response. *New Journal of Physics*, **21**, 123024.

Aghakhani, A., Yasa, O., Wrede, P. & Sitti, M. (2020). Acoustically powered surfaceslipping mobile microrobots. *Proceedings of the National Academy of Sciences*, **117**, 3469–3477.

Agrawal, M. & Glotzer, S.C. (2020). Scale-free, programmable design of morphable chain loops of kilobots and colloidal motors. *Proceedings of the National Academy of Sciences*, **117**, 8700–8710.

Boley, W.J., van Rees, W.M., Lissandrello, C., Horenstein, M.N., Truby, R.L., Kotikian, A., Lewis, J.A. & Mahadevan, L. (2019). Shape-shifting structured lattices via multimaterial 4d printing. *Proceedings of the National Academy of Sciences*, **116**, 20856–20862.

Boudet, J.F., Lintuvuori, J., Lacouture, C., Barois, T., Deblais, A., Xie, K., Cassagnere, S., Tregon, B., Brückner, D.B., Baret, J.C. & Kellay, H. (2021). From collections of independent, mindless robots to flexible, mobile, and directional superstructures. *Science Robotics*, **6**, eabd0272.

Brambilla, M., Ferrante, E., Birattari, M. & Dorigo, M. (2013). Swarm robotics: a review from the swarm engineering perspective. *Swarm Intelligence*, **7**, 1–41.

BRIAND, G., SCHINDLER, M. & DAUCHOT, O. (2018). Spontaneously flowing crystal of self-propelled particles. *Physical Review Letters*, **120**, 208001.

CADEMARTIRI, L. & BISHOP, K.J.M. (2015). Programmable self-assembly. *Nature Materials*, **14**, 2–9.

COUZIN, I.D. & KRAUSE, J. (2003). Self-organization and collective behavior in vertebrates. *Advances in the Study of Behavior*, **32**, 1–75.

CULHA, U., DAVIDSON, Z.S., MASTRANGELI, N. & SITTI, M. (2020). Statistical reprogramming of macroscopic self-assembly with dynamic boundaries. *Proceedings of the National Academy of Sciences*, **117**, 11306–11313.

DEBLAIS, A., BAROIS, T., GUERIN, T., DELVILLE, P.H., VAUDAINE, R., LINTUVUORI, J.S., BOUDET, J.F., BARET, J.C. & KELLAY, H. (2018). Boundaries control collective dynamics of inertial self-propelled robots. *Physical Review Letters*, **120**, 188002.

DEBLAIS, A., MAGGS, A.C., BONN, D. & WOUTERSEN, S. (2020). Phase separation by entanglement of active polymerlike worms. *Physical Review Letters*, **124**, 208006.

DESEIGNE, J., DAUCHOT, O. & CHATÉ, H. (2010). Collective motion of vibrated polar disks. *Physical Review Letters*, **105**, 098001.

DESEIGNE, J., LEONARD, S., DAUCHOT, O. & CHATÉ, H. (2012). Vibrated polar disks: spontaneous motion, binary collisions, and collective dynamics. *Soft Matter*, **8**, 5629–5639.

DEVRIES, G.A., BRUNNBAUER, M., HU, Y., JACKSON, A.M., LONG, B., NELTNER, B.T., UZUN, O., WUNSCH, B.H. & STELLACCI, F. (2007). Divalent metal nanoparticles. *Science*, **315**, 358–361.

DILLER, E. & SITTI, M. (2011). Micro-scale mobile robotics. *Foundations and Trends in Robotics*, **2**, 143–259.

Divband Soorati, M., Heinrich, M.K., Ghofrani, J., Zahadat, P. & Hamann, H. (2019). Photomorphogenesis for robot self-assembly: adaptivity, collective decision-making, and self-repair. *Bioinspiration & Biomimetics*, **14**, 056006.

Eisenstecken, T., Gompper, G. & Winkler, R.G. (2016). Conformational properties of active semiflexible polymers. *Polymers*, **8**, 304.

Friedl, P. & Gilmour, D. (2009). Collective cell migration in morphogenesis, regeneration and cancer. *Nature Reviews Molecular Cell Biology*, **10**, 445–457.

Garcimartín, A., Pastor, J.M., Ferrer, L.M., Ramos, J.J., Martín-Gómez, C. & Zuriguel, I. (2015). Flow and clogging of a sheep herd passing through a bottleneck. *Physical Review E*, **91**, 022808.

Gardi, G., Ceron, S., Wang, W., Petersen, K. & Sitti, M. (2022). Microrobot collectives with reconfigurable morphologies, behaviors, and functions. *Nature Communications*, **13**, 2239.

Goldstein, S.C., Campbell, J.D. & Mowry, T.C. (2005). Programmable matter. *Computer*, **38**, 99–101.

Graham, R.L., Lubachevsky, B.D., Nurmela, K.J. & Östergård, P.R.J. (1998). Dense packings of congruent circles in a circle. *Discrete Mathematics*, **181**, 139–154.

Grosser, S., Lippoldt, J., Oswald, L., Merkel, M., Sussman, D.M., Renner, F., Gottheil, P., Morawetz, E.W., Fuhs, T., Xie, X., Pawlizak, S., Fritsch, A.W., Wolf, B., Horn, L.C., Briest, S., Aktas, B., Manning, M.L. & Käs, J.A. (2021). Cell and nucleus shape as an indicator of tissue fluidity in carcinoma. *Physical Review X*, **11**, 011033.

Guix, M., Mayorga-Martinex, C.C. & Merkoçi, A. (2014). Nano/micromotors in (bio)chemical science applications. *Chemical Reviews*, **114**, 6285–6322.

Hagan, M.F. & Baskaran, A. (2016). Emergent self-organization in active materials. *Current Opinion in Cell Biology*, **38**, 74–80.

Heeremans, T., Deblais, A., Bonn, D. & Woutersen, S. (2022). Chromatographic separation of active polymerlike worm mixtures by contour length and activity. *Science Advances*, **8**, eabj7918.

Jin, D., Yu, J., Yuan, K. & Zhang, L. (2019). Mimicking the structure and function of ant bridges in a reconfigurable microswarm for electronic applications. *ACS nano*, **13**, 5999–6007.

Kaiser, A., Bebel, S., ten Hagen, B., von Ferber, C. & Löwen, H. (2015). How does a flexible chain of active particles swell? *The Journal of Chemical Physics*, **142**, 124905.

Kudrolli, A., Lumay, G., Volfson, D. & Tsimring, L.S. (2008). Swarming and swirling in self-propelled polar granular rods. *Physical Review Letters*, **100**, 058001.

Kulkarni, M., Nguyen, H. & Alexis, K. (2020). The reconfigurable aerial robotic chain: Shape and motion planning. *IFAC-PapersOnLine*, **53**, 9295–9302.

Kumar, N., Soni, H., Ramaswamy, S. & Sood, A.K. (2014). Flocking at a distance in active granular matter. *Nature Communications*, **5**, 4688.

Lanczos, C. (1986). *The variational principles of mechanics*. Dover, Toronto.

Lavergne, F.A., Wendehenne, H., Bäuerle, T. & Bechinger, C. (2019). Group formation and cohesion of active particles with visual perception-dependent motility. *Science*, **364**, 70–74.

Li, G. & Tang, J.X. (2009). Accumulation of microswimmers near a surface mediated by collision and rotational brownian motion. *Physical Review Letters*, **103**, 078101.

Li, S., Batra, R., Brown, D., Chang, H.D., Ranganathan, N., Hoberman, C., Rus, D. & Lipson, H. (2019). Particle robotics based on statistical mechanics of loosely coupled components. *Nature*, **567**, 361–365.

Li, S., Dutta, B., Cannon, S., Daymude, J.J., Avinery, R., Richa, A.W., Goldman, D.I. & Randall, D. (2021). Programming active cohesive granular matter with mechanically induced phase changes. *Science Advances*, **7**, eabe8494.

Liu, P., Zhu, H., Zeng, Y., Du, G., Ning, L., Wang, D., Chen, K., Lu, Y., Zheng, N., Ye, F. & Yang, M. (2020). Oscillating collective motion of active rotors in confinement. *Proceedings of the National Academy of Sciences*, **117**, 11901–11907.

Lowen, S.B. & Teich, M.C. (1993). Fractal renewal processes generate 1/f noise. *Physical Review E*, **47**, 992.

Marchetti, M.C., Joanny, J.F., Ramaswamy, S., Liverpool, T.B., Prost, J., Rao, M. & Aditi Simha, R. (2013). Hydrodynamics of soft active matter. *Review of Modern Physics*, **85**, 1143–1189.

Martínez-Pedrero, F., González-Banciella, A., Camino, A., Mateos-Maroto, A., Ortega, F., Rubio, R.G., Pagonabarraga, I. & Calero, C. (2021). Static and dynamic self-assembly of pearl-likechains of magnetic colloids confined at fluid interfaces. *Small*, **17**, 2101188.

McCann, C.P., Kriebel, P.W., Parent, C.A. & Losert, W. (2010). Cell speed, persistence and information transmission during signal relay and collective migration. *Journal of Cell Science*, **123**, 1724–1731.

Mlot, N.J., Tovey, C.A. & Hu, D.L. (2011). Fire ants self-assemble into waterproof rafts to survive floods. *Proceedings of the National Academy of Sciences*, **108**, 7669–7673.

Nelson, B.J., Kaliakatsos, I.K. & Abbott, J.J. (2010). Microrobots for minimally invasive medicine. *Annual Review of Biomedical Engineering*, **12**, 55–85.

Nykypanchuk, D., Maye, M.M., van der Lelie, D. & Gang, O. (2008). DNA-guided crystallization of colloidal nanoparticles. *Nature*, **451**, 549–552.

O'Connor, C. & Adams, J.U. (2010). *Essentials Of Cell Biology*. NPG Education, Cambridge.

Ozkan-Aydin, Y. & Goldman, D.I. (2021). Self-reconfigurable multi-legged robot swarms collectively accomplish challenging terradynamic tasks. *Science Robotics*, **6**, eabf1628.

Palacci, J., Sacanna, S., Steinberg, A.P., Pine, D.J. & Chaikin, P.M. (2013). Living crystals of light-activated colloidal surfers. *Science*, **339**, 936–940.

Palagi, S. & Fischer, P. (2018). Bioinspired microrobots. *Nature Review Materials*, **3**, 113–124.

Paoluzzi, M., Di Leonardo, R., Marchetti, M.C. & Angelani, L. (2016). Shape and displacement fluctuations in soft vesicles filled by active particles. *Scientific Reports*, **6**, 34146.

Patterson, G.A., Fierens, P.I., Jimka, F.S., König, P.G., Garcimartín, A., Zuriguel, I., Pugnaloni, L.A. & Parisi, D.R. (2017). Clogging transition of vibration-driven vehicles passing through constrictions. *Physical Review Letters*, **119**, 248301.

Rappel, W.J., Nicol, A., Sarkissian, A., Levine, H. & Loomis, W.F. (1999). Self-organized vortex state in two-dimensional dictyostelium dynamics. *Physical Review lLetters*, **83**, 1247–1250.

Rubenstein, M., Cornejo, A. & Nagpal, R. (2014). Programmable self-assembly in a thousand-robot swarm. *Science*, **345**, 795–799.

Sanchez, T., Chen, D.T.N., DeCamp, S.J., Heymann, M. & Dogic, Z. (2012). Spontaneous motion in hierarchically assembled active matter. *Nature*, **491**, 431–434.

Savoie, W., Berrueta, T.A., Jackson, Z., Pervan, A., Warkentin, R., Li, S., Murphey, T.D., Wiesenfeld, K. & Goldman, D.I. (2019). A robot made of robots: Emergent transport and control of a smarticle ensemble. *Science Robotics*, **4**, eaax4316.

Scholz, C., D'Silva, S. & Pöschel, T. (2016). Ratcheting and tumbling motion of vibrots. *New Journal of Physics*, **18**, 123001.

Scholz, C., Engel, M. & Pöschel, T. (2018). Rotating robots move collectively and self-organize. *Nature Communications*, **9**, 931.

Scholz, C., Ldov, A., Pöschel, T., Engel, M. & Löwen, H. (2021). Surfactants and rotelles in active chiral fluids. *Science Advances*, **7**, eabf8998.

Sitti, M. (2017). *Mobile microrobotics*. MIT Press, Cambridge.

Slavkov, I., Carrillo-Zapata, D., Carranza, N., Diego, X., Jansson, F., Kaandorp, J., Hauert, S. & Sharpe, J. (2018). Morphogenesis in robot swarms. *Science Robotics*, **3**, eaau9178.

Spellings, M., Engel, M., Klotsa, D., Sabrina, S., Drews, A.M., Nguyen, N.H.P., Bishop, K.J.M. & Glotzer, S.C. (2015). Shape control and compartmentalization in active colloidal cells. *Proceedings of the National Academy of Sciences*, **112**, E4642–E4650.

Tinevez, J.Y., Perry, N., Schindelin, J., Hoopes, G.M., Reynolds, G.D., Laplantine, E., Bednarek, S.Y., Shorte, S.L. & Eliceiri, K.W. (2017). Trackmate: An open and extensible platform for single-particle tracking. *Methods*, **115**, 80–90.

TONER, J. & TU, Y. (1995). Long-range order in a two-dimensional dynamical xy model: how birds fly together. *Physical Review Letters*, **75**, 4326.

VICSEK, T. & ZAFEIRIS, A. (2012). Collective motion. *Physics Reports*, **517**, 71–140.

VINCENTI, B., RAMOS, G., CORDERO, M.L., DOUARCHE, C., SOTO, R. & CLEMENT, E. (2019). Magnetotactic bacteria in a droplet self-assemble into a rotary motor. *Nature Communications*, **10**, 5082.

VUTUKURI, H.R., LISICKI, M., LAUGA, E. & VERMANT, J. (2020). Light-switchable propulsion of active particles with reversible interactions. *Nature Communications*, **11**, 2628.

WANG, W., GILTINAN, J., ZAKHARCHENKO, S. & SITTI, M. (2017). Dynamic and programmable self-assembly of micro-rafts at the air-water interface. *Science Advances*, **3**, e1602522.

WANG, W., GARDI, G., MALGARETTI, P., KISHORE, V., KOENS, L., SON, D., GILBERT, H., WU, Z., HARWANI, P., LAUGA, E., HOLM, C. & SITTI, M. (2022). Order and information in the patterns of spinning magnetic micro-disks at the air-water interface. *Science Advances*, **8**, eabk0685.

WEEKS, J.D., CHANDLER, D. & ANDERSON, H.C. (1971). Role of repulsive forces in determining the equilibrium structure of simple liquids. *The Journal of Chemical Physics*, **54**, 5237–5247.

WESTLEY, P.H.A., BERDAHI, A.M., TORNEY, C.J. & BIRO, D. (2018). Collective movement in ecology: from emerging technologies to conservation and management. *Philosophical Transactions of the Royal Society B: Biological Sciences*, **373**, 20170004.

WINKLER, R.G., ELGETI, J. & GOMPPER, G. (2017). Active polymers–emergent conformational and dynamical properties: A brief review. *Journal of the Physical Society of Japan*, **86**, 101014.

Xie, H., Sun, M., Fan, X., Lin, Z., Chen, W., Wang, L., Dong, L. & He, Q. (2019). Reconfigurable magnetic microrobot swarm: Multimode transformation, locomotion, and manipulation. *Science Robotics*, **4**, eaav8006.

Yan, L., Han, M., Zhang, J., Xu, C., Luijten, E. & Granick, S. (2016). Reconfiguring active particles by electrostatic imbalance. *Nature Materials*, **15**, 1095–1099.

Yigit, B., Alapan, Y. & Sitti, M. (2019). Programmable collective behavior in dynamically self-assembled mobile microrobotic swarms. *Advanced Science*, **6**, 1801837.

Zhang, C., Macfarlane, R.J., Young, K.L., Choi, C.H., Hao, L., Auyeung, E., Liu, G., Zhou, X. & Mirkin, C.A. (2013). A general approach to DNA-programmable atom equivalents. *Nature Materials*, **12**, 741–746.

Zhang, H.P., Be'er, A., Florin, E.L. & Swinney, H.L. (2010). Collective motion and density fluctuations in bacterial colonies. *Proceedings of the National Academy of Sciences*, **107**, 13626–13630.

Zhang, J., Mou, F., Wu, Z., Song, J., Kauffman, J.E., Sen, A. & Guan, J. (2021). Cooperative transport by flocking phototactic micromotors. *Nanoscale Advances*, **3**, 6157–6163.

Zheng, W., Buhlmann, P. & Jacobs, H.O. (2004). Sequential shape-and-solder-directed self-assembly of functional microsystems. *Proceedings of the National Academy of Sciences*, **101**, 12814–12817.

Appendix B

Abstract in Korean

국문초록

형태학적 제어를 통한 진동 입자 군집의 가변적 거동

서울대학교 대학원
기계공학부
손경민

요약

한정된 자원을 사용해 여러 환경에서 다양한 기능을 수행할 수 있는 로봇 기계에 대한 필요성이 최근 증대됨에 따라, 다양한 목적으로 활용 가능한 새로운 기계 시스템에 관한 연구가 주목받고 있다. 또한, 이러한 기능성은 작은 스케일의 여러 분야에도 적용될 수 있으며, 이를 위해서는 여러 스케일로 확장 가능한 시스템 설계가 필요하다. 이때, 형태를 변화시키며 다양한 임무를 수행하는 자연계의 군집들은 입자 및 로봇 군집을 활용한 새로운 시스템 개발의 토대가 된다. 본 연구에서는 최근의 인공 군집 시스템에서 더 나아가 정교한 외부 제어 없이 형태학적 제어를 통한 구성 요소 간 기계적 상호작용만을 조절하여 입자 구조체의 다양한 거동과 기능을 구현하였다.

먼저, 밀집된 2차원의 원형 공간을 수직 진동에 의해 자체 추진하는 소수의 능동 입자들과 임의로 움직이는 입자들로 가득 채워, 능동 입자의 운동성 및 모양이 밀집된 환경에서의 거동에 어떤 영향

을 주는지를 실험적으로 규명하였다. 높은 이동성을 갖는 능동 입자는 밀집된 환경에서 초확산 거동을 보이며, 확산 지수는 종횡비에 따라 증가하는 특징을 보인다. 이후 능동 입자가 경계에 도달하면 클러스터를 형성하고, 능동 입자의 수에 따라 클러스터의 속도 및 경계에 대한 정렬이 달라짐을 보였다. 또한, 내부 및 경계에서의 능동 입자의 거동을 정량적 및 정성적으로 분석하였다. 본 연구 결과는 복잡한 외부 자극 없이 모양 및 개수 변화를 통한 입자 간 기계적 상호작용의 조절만으로 자기 조직화를 제어할 가능성을 제시하였다는 점에서 의의가 있다.

다음으로, 입자들을 원형의 움직일 수 있는 테두리에 가둬, 구조적으로 견고하면서도 움직일 수 있는 입자 구조체를 제작하였다. 능동 입자의 모양과 수를 조절하여 임의로 움직이거나 회전 및 한 방향 운동 등 구조체의 다양한 거동을 구현하였다. 이후 구조체를 이루는 입자 개수와 입자를 감싸는 원형 틀의 기계적 물성을 조절하여 구조체의 직진성, 회전성 등의 동적 특성을 세밀하게 제어할 수 있음을 보였다. 본 연구 결과는 밀집된 시스템을 이루는 구성 요소의 작은 변경을 통해 전체 거동을 조절할 수 있음을 밝혀냈다는 점에서 의의가 있다.

마지막으로, 입자를 가두는 접근에서 벗어나 높은 변형성 및 다기능성을 갖는 입자 구조를 개발하는 연구를 수행하였다. 능동 입자들을 링크로 연결해 매우 유연한 체인 구조를 만들었으며, 각 구성 요소의 설계 변수를 조절하여 입자들의 상대적인 움직임을 제어하고 체인의 다양한 거동을 보였다. 이후 체인 구조가 물체 둘러싸거나 지나가고, 물체를 앞 또는 뒤로 운반하며, 좁은 공간을 통과하거나 막는 등 여러 상충하는 작업을 수행할 수 있음을 보였다. 마지막으로 기하학적 분석을 통해 다양한 체인 동작의 메커니즘과 이동 속

도 및 방향에 대한 심층적 분석을 제시하였다. 본 연구 결과는 물체 운반, 환경 모니터링, 통행 제어 등의 기능이 가능한 견고하면서도 단순한 로봇 개발에 적용될 수 있다.

군집 시스템이 보여주는 다양한 거동 및 기능은 형상 제어를 통한 구성 요소 간 기계적 상호작용을 조절하는 방법이 단순한 입자만을 이용해 가변적으로 다양한 기능을 구현하는데 활용될 수 있음을 보여준다. 본 연구는 다양한 스케일에서 최소한의 구성 요소로 재구성이 가능한 소프트 로봇 시스템을 개발하는 데 큰 도움을 제공할 수 있을 것이다.

주요어 : 능동 물질, 진동 입자, 군집 거동, 프로그래밍 가능 로봇, 형태학적 제어
학 번 : 2018 - 31738